

# Radiative properties and multiwavelength variability of turbulent two-temperature MADs

*A thesis submitted in partial fulfilment of the requirements for the degree Master of Science in*

*Physics and Astronomy*

*Supervisor:*

Dr. Monika Mościbrodzka

*Author:*

Maarten Wijdeveld  
(s1045554)

*Second reader:*  
Prof. Dr. Andrew Levan

## Abstract

We present radiative transfer models based on two-temperature Magnetically Arrested Disc (MAD) general relativistic magnetohydrodynamics simulations of Sagittarius A\* (Sgr A\*). We compare a physically motivated electron heating model based on Alfvénic turbulence with a commonly applied ion-to-electron temperature parametrisation equation (the  $R(\beta)$  prescription). We model the dominant compact emission through synchrotron self-Compton and produce spectral energy distributions for both a non-spinning ( $a_* = 0$ ) and high-spin ( $a_* = 0.94$ ) black hole (BH). We extract near-infrared (NIR) and X-ray light curves throughout  $\sim 28$  hours of the disc's evolution and analyse their variable properties. Our results show that, regardless of BH spin, the more physically sophisticated turbulent heating model is reasonably well approximated by parametrised models, both in terms of its averaged long-term spectral properties and short-term temporal variability. Our  $a_* = 0.94$  spin model light curves are significantly more variable, especially toward cooler  $R(\beta)$  prescriptions, which we link to a long-term ( $\sim 8$  hour) periodic component and an increased sensitivity to fluctuations in the accretion flow. For both BH spin models, strong heating takes place in the layers surrounding highly magnetised plasma originating from magnetic flux eruptions in the disc. However, both turbulent heating and hot parametrisation models consistently overproduce both quiescent NIR and X-ray constraints and fail to reproduce the large flare-to-quiescent luminosity ratios observed for Sgr A\*. None of our models are capable of reproducing the strongest observed X-ray flare luminosities. Cooler parametrisation models do stay in line with quiescent constraints, but underpredict flare luminosities. These findings suggest that a combination of (potentially alternative) temperature models may be required to match observations assuming a MAD state, including a possible nonthermal component to match luminous X-ray flares.

# Contents

<b>1</b>	<b>Introduction</b>	<b>3</b>
1.1	Preliminaries of black holes . . . . .	3
1.2	Accretion flows . . . . .	6
1.2.1	Cold accretion flows . . . . .	7
1.2.2	Hot accretion flows . . . . .	8
1.2.3	Specifics of ADAFs . . . . .	9
1.3	Sagittarius A* . . . . .	11
1.4	This work . . . . .	12
<b>2</b>	<b>Numerical Model and Analysis Methodology</b>	<b>14</b>
2.1	MAD GRMHD models . . . . .	14
2.2	Electron temperature prescriptions . . . . .	15
2.3	Radiative transfer . . . . .	18
2.4	Analysis specifics . . . . .	19
<b>3</b>	<b>Results</b>	<b>21</b>
3.1	Radiative properties of MADs . . . . .	21
3.2	Multiwavelength light curve time variability . . . . .	31
3.3	Comparison to observations . . . . .	38
<b>4</b>	<b>Discussion and Conclusion</b>	<b>40</b>
4.1	Turbulent heating and $R(\beta)$ prescriptions in MADs . . . . .	40
4.2	Emission zones characteristics and light curve variability . . . . .	40
4.3	The role of magnetic reconnection heating . . . . .	41
4.4	Effect of magnetisation cut-off . . . . .	42
<b>5</b>	<b>Bibliography</b>	<b>44</b>
<b>A</b>	<b>Appendix - Bias modification</b>	<b>51</b>
<b>B</b>	<b>Appendix - Emission maps and plasma parameters</b>	<b>52</b>
<b>C</b>	<b>Appendix - Prospects for a <math>R(\beta, \sigma)</math> prescription</b>	<b>54</b>

### 1.1 Preliminaries of black holes

Historically, objects in spacetime from which even massless photons are unable to escape have been termed ‘dark stars’, ‘frozen stars’ or, rather technically, ‘gravitationally collapsed objects’. Nowadays, however, we typically refer to such an object as a ‘black hole’ (BH). Such an object is unique, as past a certain radius known as the ‘event horizon’ ( $r_h$ ), the only allowed timelike trajectories are those doomed to end up in a singularity at the centre. BHs can be fully characterised by just three independent properties: mass, spin and electric charge, often referred to as the ‘no-hair’ theorem. All other information about material inside the event horizon, such as details about its structure or composition, remains irretrievably lost. As most astrophysical BHs are thought to be electrically neutral - any charged BH will quickly accumulate enough opposite charge to become neutral - we are left with two major observables to be narrowed down: the mass and spin vector.

The first (unique) exact solution to Einstein’s field tensor equations for such a non-rotating (and non-charged) BH was found by [Schwarzschild \(1916\)](#). The Schwarzschild solution describes the curvature of spherically symmetric vacuum spacetime around a massive object. Setting  $G = c = 1$ , as is customary in general relativity (GR), the metric takes the form of

$$ds^2 = - \left(1 - \frac{2M}{r}\right) dt^2 + \left(1 - \frac{2M}{r}\right)^{-1} dr^2 + r^2 d\Omega^2 \quad (1)$$

in spherical coordinates, where  $d\Omega^2 = d\theta^2 + \sin^2 \theta d\phi^2$  describes the standard angular part of the metric. Here,  $r$  is the radial coordinate,  $t$  the time coordinate and  $M$  the central object’s conventional Newtonian mass. For brevity, we omit a derivation but refer to works such as [Eddington \(1923\)](#) (page 82-85) or more modern versions such as found in [Carroll \(2004\)](#) (Chapters 5.1 and 5.2), which also demonstrate the use of Birkhoff’s theorem to show that this solution is in fact unique. We immediately make two important observations. First, at  $r = 2M$  (the Schwarzschild radius:  $r_s$ ), the metric lacks a valid solution and seemingly reveals some sort of singularity at the event horizon. In fact, this is merely an artefact of the underlying coordinate system, a coordinate singularity intrinsic to the Schwarzschild metric expressed in spherical coordinates. The solution lies in switching to a different coordinate system. Although Kruskal-Szekeres coordinates fully describe the global structure of the Schwarzschild spacetime, Eddington-Finkelstein coordinates are often used to show there is no actual divergence at  $r = 2M$  for timelike and null particles. For an in-depth discussion, we refer to [Carroll \(2004\)](#) and [Misner et al. \(1973\)](#). Second is the divergence at  $r = 0$ , which does correspond to an actual physical singularity. Furthermore, although commonly applied in the context of BHs, it is important to note that the Schwarzschild solution is perfectly adequate for most spherically symmetric mass distributions (e.g. a solar-mass star), provided we restrict our analysis to the vacuum region *outside* the object.

Starting with the launch of the first dedicated X-ray satellite in 1970 (the Uhuru mission, [Giacconi et al. 1972](#)), the 70s, 80s and 90s pioneered an abundance of continually improving X-ray observations (see e.g. [Santangelo and Madonia 2014](#) and references therein), first providing significant insight into the nature of accreting BHs. While the Schwarzschild metric offers a model to compare to non-rotating black holes, it may be an oversimplification when interpreting observational data. Indeed, if a rotating star collapses to form a BH, one might expect at least a fraction of its angular momentum to be conserved. Then, building upon the Schwarzschild solution, the next natural step in describing the spacetime around such an object would be to include a rotation parameter into the metric. This was first realised by [Kerr \(1963\)](#), who found an exact solution for an uncharged, rotating BH, now referred to as the Kerr metric. In fact, this is the most general regular axisymmetric stationary<sup>1</sup> spacetime ([Compère and Fiorucci,](#)

---

<sup>1</sup>although certainly not necessarily static

2018). The Kerr metric incorporates the spin parameter  $a = J/M$  ( $J$  being the angular momentum), so that  $-M \leq a \leq M$ . It is often convenient to make use of a dimensionless spin parameter defined as  $a_* \equiv J/M^2$  (with then  $-1 \leq a_* \leq 1$ ). As the BH mass typically sets the length and timescales, numerical studies often fix the mass through  $G = c = M = 1$  (so that  $a = a_*$ ). Both time and spatial components of e.g. a particles trajectory are then given in units of BH mass, making it straightforward to scale them back to physical units by the choice of BH mass (§2.1, Eq. 21 and 22).

The Kerr metric is perhaps most familiar when written in Boyer-Lindquist (BL) coordinates

$$ds^2 = -\frac{\Delta}{\Sigma} (dt - a \sin^2 \theta d\phi)^2 + \Sigma \left( \frac{dr^2}{\Delta} + d\theta^2 \right) + \frac{\sin^2 \theta}{\Sigma} ((r^2 + a^2) d\phi - a dt)^2, \quad (2)$$

where  $\Delta \equiv r^2 - 2r + a^2$ ,  $\Sigma \equiv r^2 + a^2 \cos^2 \theta$ . The transformation from BL to Cartesian coordinates differs only slightly from the spherical-to-Cartesian transformation as  $x = \sqrt{r^2 + a^2} \sin \theta \cos \phi$ ,  $y = \sqrt{r^2 + a^2} \sin \theta \sin \phi$  and  $z = r \cos \theta$ . It is then straightforward to show that Eq. 2 indeed transforms back to the regular Schwarzschild metric in spherical coordinates by setting  $a = 0$  (and  $M = 1$ ).

In the Schwarzschild metric, the event horizon remains constant (assuming fixed BH mass) at  $r = 2r_g = 2M$ . Perhaps as one would expect, this is merely a special case retrieved by setting  $a_* = 0$  in the Kerr metric. If  $a_* \neq 0$ , the Kerr geometry's one-way membrane (i.e. the event horizon's analogue) is the positive root of  $\Delta = 0$

$$\frac{r_+}{M} = 1 + \sqrt{1 - a_*^2}, \quad (3)$$

often referred to as the outer event horizon. However, setting  $\Delta = 0$  in Eq. 2 hints at a similar instability as encountered for the Schwarzschild metric in spherical coordinates. Likewise, the BL-form of the Kerr metric is singular at the event horizon. To resolve this, studies that require the inclusion of horizon-scale effects often make use of Kerr-Schild (KS) coordinates. These leave  $r$  and  $\theta$  unchanged, but transform  $t$  and  $\phi$  according to (e.g. McKinney and Gammie, 2004)

$$\partial t_{KS} = \partial r_{BL} \frac{2r}{\Delta} \quad \text{and} \quad \partial \phi_{KS} = \partial r_{BL} \frac{a}{\Delta}. \quad (4)$$

Dropping the subscript, the metric in Kerr-Schild coordinates then becomes

$$\begin{aligned} ds^2 = & - \left( 1 - \frac{2r}{\Sigma} \right) dt^2 + \left( \frac{4r}{\Sigma} \right) dr dt + \left( 1 + \frac{2r}{\Sigma} \right) dr^2 + \Sigma d\theta^2 \\ & + \sin^2 \theta \left( \Sigma + a^2 \sin^2 \theta \left( 1 + \frac{2r}{\Sigma} \right) \right) d\phi^2 \\ & - \left( \frac{4ar \sin^2 \theta}{\Sigma} \right) d\phi dt - 2a \left( 1 + \frac{2r}{\Sigma} \right) \sin^2 \theta d\phi dr, \end{aligned} \quad (5)$$

which no longer blows up as  $r \rightarrow r_+$ .

Outside the event horizon, we find another peculiar radial coordinate where the notion of a stable circular orbit in GR breaks down, known as the innermost stable circular orbit (ISCO;  $r_{ISCO}$ ). This occurs as GR introduces an additional term in a *massive* test particle's potential, making it impossible for stable orbits to exist for  $r < r_{ISCO}$ . An isolated test particle orbiting between  $r_{EH} < r < r_{ISCO}$  will only be able to do so while decreasing its radial coordinate, unavoidably inspiraling toward the event horizon. For a non-rotating BH in the Schwarzschild metric, the ISCO is located at  $r_{ISCO} = 6M$ . In the Kerr metric, the ISCO for a prograde moving test particle ( $a_* > 0$ ) decreases with increasing BH spin, just like the event horizon. A generalisation of the ISCO to rotating systems is not straightforward and follows

(Bardeen et al., 1972)

$$\frac{r_{ISCO}}{M} = 3 + Z_2 \mp [(3 - Z_1)(3 + Z_1 + 2Z_2)]^{1/2},$$

$$Z_1 \equiv 1 + (1 - a_*^2)^{1/3} \left[ (1 + a_*)^{1/3} + (1 - a_*)^{1/3} \right],$$

$$Z_2 \equiv (3a_*^2 + Z_1^2)^{1/2}, \quad (6)$$

where for prograde orbits, we take a negative sign, and for retrograde orbits, a positive sign. Both the ISCO and rotating BH outer event horizon depend on BH spin, decreasing with increasing  $a_*$  for prograde orbits. At  $a_* = 1$ ,  $r_{ISCO} = r_+ = 1$  and at  $a_* = 0.9375$ ,  $r_{ISCO} = 2.044$ , while  $r_+ = 1.348$  (this latter case will return later in this work). Both Eqs. 3 and 6 are nicely approximated by a combination of a decaying square root and a linear component as

$$\frac{r_{+, ISCO}}{M} = c_1 + c_2 \sqrt{1 - a_*} + c_3 a_*, \quad (7)$$

with  $c_1$ ,  $c_2$  and  $c_3$  constants differing between cases. In Fig. 1, this approximation is fitted to Eqs. 3 and 6, which helps identify the strong negative linear dependence of Eq. 6 for spin below  $a_* \lesssim 0.8$ . If we define the intra-ISCO area in the equatorial plane as

$$A_{ISCO} = \pi (r_{ISCO}^2 - r_+^2), \quad (8)$$

Fig. 1 shows that this rapidly shrinks with increasing BH spin as  $\frac{dr_{ISCO}}{da_*} \ll \frac{dr_+}{da_*}$ . In an accreting system with a low to non-spinning BH, this has important consequences for the inner part of the disc, as inside the ISCO, the nature of the fluid changes drastically due to its velocity quickly becoming radially dominated. Toward higher spin, however, this region shrinks significantly, not affecting the disc nearly as much.

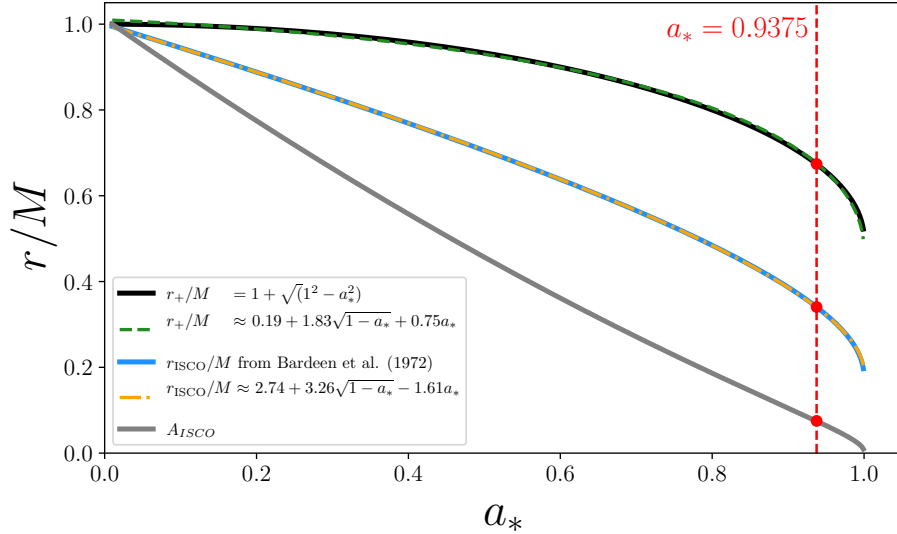


**Figure 1:** Prograde BH spin dependence of the outer event horizon (solid black line, in units of  $M = 1$ ), ISCO (solid blue line) and the intra-ISCO area in the equatorial plane (solid grey line). All lines are normalised to their  $a_* = 0$  value. The green dashed and orange dash-dotted lines represent fitted approximations according to Eq. 7, which help highlight the distinctly different decreasing behaviour of the ISCO (Eq. 6) compared to the event horizon (Eq. 3). The vertical red dashed line intersects all curves at  $a_* = 0.9375$ .

Clearly, the inclusion of GR near compact objects differs significantly from the Newtonian approach. To

further refine this framework, we need to generalise the notion of a straight line in curved spacetime. To this extent, we redefine the idea of a straight line to that of a geodesic - the path that extremizes distances (or rather the spacetime interval) between events. Such geodesics effectively replace the Newtonian notion of gravitational force with the underlying curved geometry. In other words, free-falling timelike (massive) and lightlike (photons) particles, undergoing only gravitational acceleration, must move along geodesics. Mathematically, geodesics are described by the geodesic equation, governing how the 4d vector components of a particle  $x^\mu(\lambda)$  evolve along the path parametrised by an affine parameter  $\lambda$

$$\frac{d^2x^\mu}{d\lambda^2} + \Gamma_{\alpha\beta}^\mu \frac{dx^\alpha}{d\lambda} \frac{dx^\beta}{d\lambda} = 0, \quad (9)$$

where repeated indices are summed over according to Einstein's summation convention. Here  $\Gamma_{\alpha\beta}^\mu$  are the Christoffel symbols, defined as

$$\Gamma_{\alpha\beta}^\mu = \frac{1}{2} g^{\mu\nu} (\partial_\alpha g_{\nu\beta} + \partial_\beta g_{\nu\alpha} - \partial_\nu g_{\alpha\beta}), \quad (10)$$

with  $g_{\mu\nu}$  the metric components such that  $ds^2 = g_{\mu\nu} dx^\mu dx^\nu$ . Characteristic of a geodesic is the condition that its tangent vector ( $u^\mu = \frac{dx^\mu}{d\lambda}$ ) is parallel transported along the curve, i.e.  $u^\mu \nabla_\mu u^\nu = u^\mu \partial_\mu v^\nu + u^\mu \Gamma_{\mu\rho}^\nu v^\rho = 0$ , where  $\nabla_\mu$  is the covariant derivative. A proof of Eq. 9 is typically motivated through the principle of least action, but will be omitted here (see e.g. [Misner, Thorne, and Wheeler 1973](#)).

We are still free to choose the parametrisation parameter  $\lambda$  to smoothly parametrize the particles worldline. For timelike (massive) particles, we typically choose  $\lambda$  to be the proper time  $\tau$ , so that  $d\tau^2$  is proportional to  $\pm ds^2$ , depending on signature convention. However, for lightlike particles (photons)  $d\tau = 0$ , so that it is more convenient to choose  $\lambda$  such that

$$k^\mu = \frac{dx^\mu}{d\lambda}, \quad (11)$$

where  $k^\mu$  is the photons four-wavevector, defined as

$$k^\mu = \left( \frac{\omega}{c}, \vec{k} \right), \quad (12)$$

with  $\omega$  the angular frequency and  $\vec{k}$  the 3-dimensional wavevector. In other words,  $k^\mu$  must be tangent to the photon's worldline. As  $d\tau = 0$  for photons, these must satisfy the null-condition

$$g_{\mu\nu} k^\mu k^\nu = 0. \quad (13)$$

Eq. 11 combined with Eq. 13, allows us to find the path a photon follows in curved spacetime, accounting for effects such as gravitational redshift and lensing in the vicinity of compact objects, such as (spinning) BHs.

## 1.2 Accretion flows

Matter falling toward a BH typically possesses non-zero angular momentum, which it must first get rid of before being able to accrete. The process mediating this outward angular momentum transport causes inspiraling material to spread into a rotating, flattened structure known as an accretion disc. As collisional atomic viscosity on its own is not enough to provide sufficient outward momentum transport, other mechanisms are typically invoked. These were originally proposed to be the result of some sort of shear-driven hydrodynamical turbulence, ultimately resulting in an effective viscosity  $\nu = \alpha H c_s$  ([Shakura and Sunyaev, 1973](#)), with  $\alpha$  a dimensionless parameter,  $H$  the disc height and  $c_s$  the isothermal speed of sound ( $c_s = \sqrt{\gamma P_g / \rho}$ , with  $\gamma, P_g, \rho$  the adiabatic gas index, gas pressure and gas density, respectively). Although an oversimplification, this framework has proven remarkably successful in de-

scribing the macroscopic behaviour of a wide range of astrophysical systems, such as protoplanetary discs, X-ray binaries (XRBs) and active galactic nuclei (AGN). In particular, assuming such an effective viscosity model and conservation of mass, radial momentum, angular momentum and energy, allows us to set up general height-integrated differential equations in flat spacetime, governing dynamics in the disc (Narayan and Yi 1994; Yuan and Narayan 2014)

$$\frac{d}{dr}(\rho r H v_r) = 0, \quad (14)$$

$$v_r \frac{dv_r}{dr} - \Omega^2 r = -\Omega_K^2 r - \frac{1}{\rho} \frac{d}{dr}(\rho c_s^2), \quad (15)$$

$$v_r \frac{d(\Omega r^2)}{dr} = \frac{1}{\rho r H} \frac{d}{dr} \left( \nu \rho r^3 H \frac{d\Omega}{dr} \right), \quad (16)$$

$$\rho v_r \left( \frac{de}{dr} - \frac{P_g}{\rho^2} \frac{dp}{dr} \right) = \rho \nu r^2 \left( \frac{d\Omega}{dr} \right)^2 - q^-, \quad (17)$$

with  $r$  the spherical radial coordinate,  $\rho$  the mid-plane gas density,  $\Omega$  the angular velocity,  $\Omega_K$  the Keplerian angular velocity,  $e$  the specific internal energy,  $v_r$  the radial velocity,  $q^-$  the radiative cooling rate and  $P_g$  the gas pressure. While these conservation equations are formally general, the resulting self-similar solutions remain height-integrated and scale-free. Although providing a good approximation for the thin disc ( $H/r \ll 1$ ), they fail to provide global thick disc ( $H/r \sim 1$ ) solutions, where disc turbulence plays a significant dynamical role (§1.2.2, 1.2.3). Even so, they still offer useful scaling relations for quantities like temperature, density and radial velocity, ignoring complications such as outflows, jets, or the evolution of the large-scale magnetic field.

While the precise microphysics that determines  $\alpha$  remains uncertain, the magnetorotational instability (MRI) (Balbus and Hawley, 1991) is widely seen as the leading instability that gives rise to turbulence, mediating the outward transport of angular momentum. The MRI occurs when a weak magnetic field and a conducting disc with radially decreasing angular velocity interact. The ionised, highly conductive plasma stays connected through magnetic field lines, transferring momentum outwards due to the differential difference in the disc's rotational velocity. A similar instability was first identified in the context of fluid dynamics by Velikhov (1959), but its astrophysical significance was later recognised by Balbus and Hawley (1991, 1998). Numerical studies have shown that the MRI is guaranteed as long as the gas and magnetic fields are strongly coupled (see Yuan and Narayan, 2014, §3.2.1, and references therein). Although inherently a linear instability, the MRI rapidly evolves into nonlinear turbulence in accretion discs, growing on dynamical timescales. This has important consequences for the global evolution of the disc, leading to different behaviour across various types of accretion flows. In the following, we give a (short) overview of the main accretion regimes before providing a more in-depth discussion of the model most relevant for this work.

### 1.2.1 Cold accretion flows

A widely celebrated model, often applied to luminous active galactic nuclei (AGN) or to X-ray binaries (XRBs), is the ‘standard’ thin disc (Shakura and Sunyaev, 1973). This model describes a geometrically thin ( $H/r \ll 1$ ) and optically thick ( $\tau \gg 1$ ) disc, radiating with a black body spectrum, typically peaking in the ultraviolet for AGN, while in soft X-rays for XRBs. That same year, Novikov and Thorne (1973) extended the Shakura and Sunyaev disc (SSD) model to include properties of the Kerr metric, which drastically impacts the structure of the disc through e.g. the existence of an inner dynamical disc boundary (described in the above as the ISCO, §1.1). Page and Thorne (1974) further refined the SSD model by extending the relativistic mathematical framework and providing an expression for the radius-dependent energy flux emitted from the disc's surface, helping link the model to observations. As

thin discs are sufficiently dense and ionised, the gas is strongly magnetically coupled, enabling turbulent angular momentum transport, well approximated by tweaking  $\alpha$  to fit observations. Consequently, such models are also often referred to as  $\alpha$ -discs.

Thin-disc systems must accrete just under their Eddington mass accretion rate ( $\dot{M}_{Edd} = 10L_{Edd}/c^2$ <sup>2</sup>, where  $L_{Edd} \equiv 4\pi MGcm_p/\sigma_e$  with  $m_p$  the proton mass and  $\sigma_e$  the Thompson cross-section) with typical luminosities of  $L \lesssim L_{Edd} = 0.1\dot{M}_{Edd}c^2$ , so that densities are high enough for the gas to be optically thick (see ‘high state’ in Fig. 2). However, as  $\dot{M} > \dot{M}_{Edd}$ , the disc becomes too optically thick to radiate internally dissipated energy in time, retaining the energy to eventually be advected toward the event horizon. This significantly lowers its radiative efficiency to  $L \ll 0.1\dot{M}_{Edd}c^2$ . Such discs are commonly known as slim discs, forming a class of radiatively inefficient and optically thick accretion flows (Katz 1977; Begelman 1979; Abramowicz et al. 1988). As dissipated energy is retained, radiation pressure strongly increases toward the inner parts of the disc, causing the disc scale height to increase (see ‘very high state’ in Fig. 2). Both the thin and slim disc belong to a class of cold accretion flows, with temperatures typically between  $10^4 - 10^7$  K.

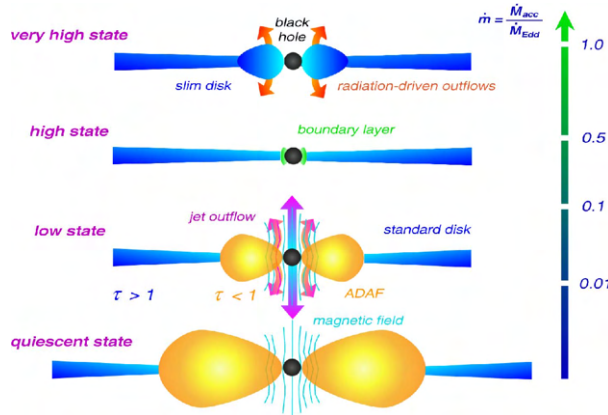


**Figure 2:** Unified scheme for BH accretion. The mass accretion rate on the right is scaled by  $\dot{M}_{Edd}$ . Independent of BH mass, the mass accretion rate dictates the state of the disc. Figure retrieved from Müller (2004).

### 1.2.2 Hot accretion flows

As the  $\alpha$ -disc is incapable of producing the observed X-rays energy range from Cygnus X-1, Shapiro, Lightman, and Eardley (1976) developed hot accretion solutions, now referred to as the SLE model, to successfully model its hard X-rays emission. In their model, the inner disc region is considerably hotter, gas-pressure dominated, optically thin and geometrically thick ( $H/r \approx 1$ ). Most notable perhaps is their inclusion of a two-temperature plasma, where the ions have a much higher temperature compared to the electrons. However, Pringle (1976) showed this model to be thermally unstable. Ichimaru (1977) first pointed out the possibility that only a portion of the viscously dissipated energy is lost through emission, while the rest goes into the heating of the gas. This helps keep the model stable, as now excess energy can be advected toward the event horizon.

In this work, we will focus on a subclass of hot accretion flows which builds upon these ideas, consisting of optically thin plasma accreting at a low mass accretion rate ( $\dot{M}/\dot{M}_{Edd} \ll 0.1$ ). As a result, the plasma density becomes low so that Coulomb couplings between ions and electrons are inefficient. However, electrons can efficiently exchange energy through synchrotron self-absorption, so that their distribution is approximately thermal. We do note that for the most energetic electrons, power-law distributions remain likely. As there is no thermal equilibrium between ions and electrons, the electrons radiate efficiently

<sup>2</sup>Assuming a radiative efficiency of  $\eta = 0.1$ . Sometimes  $\eta = 1$  or other definitions are used in literature.

(through synchrotron, inverse-Compton and Bremsstrahlung emission), whereas the ions remain hot and retain the bulk of the thermal energy of the flow. The result is a two-temperature plasma where the electrons radiate and cool, whereas the protons do not and remain hot. To keep such solutions stable, viscously dissipated energy, which is now retained in the disc, needs to be advected toward the event horizon, hence the term advection-dominated accretion flow (ADAF, ‘low state’ in Fig. 2), which is the regime that we study in the rest of this thesis. Although advection is important in both ADAFs and slim discs, we typically exclusively associate the term ‘ADAF’ with hot accretion flows. Moreover, the term ADAF is often used synonymously with radiatively inefficient accretion flows (RIAFs). Here, we will stick to the prior while explicitly referring to the thin or slim disc when discussing colder regimes. An overview of the main accretion regimes is given in Fig. 3, highlighting the differences in mass accretion rate and disc surface density between hot solutions (left of the blue vertical dashed line) and cold solutions (right of the blue vertical dashed line).

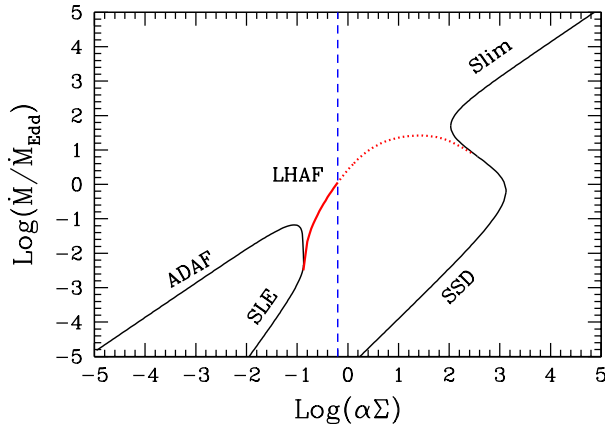


**Figure 3:** The accretion rate normalized to  $\dot{M}_{Edd}$  against the surface density ( $\Sigma \equiv 2\rho H$ ) in units of  $\text{g/cm}^2$ . Curves then describe thermal equilibrium solutions for various accretion regimes (assuming  $M = 10 M_\odot$ ,  $r = 5$  and viscosity parameter  $\alpha = 0.1$ ). The blue vertical dashed line denotes the separation between hot and optically thin solutions (left) versus the cold and optically thick (right) solutions. SSD (Shakura Sunyaev disc) refers to the thin  $\alpha$ -disc. We here omit a discussion of the luminous hot accretion flow (LHAF). Figure retrieved from [Yuan and Narayan \(2014\)](#).

### 1.2.3 Specifics of ADAFs

As discussed above, ADAFs represent a class of radiatively inefficient hot accretion solutions. These are particularly relevant in low-luminosity AGN (LLAGN) and thought to be applicable to Sagittarius A\* (Sgr A\*) in the centre of our Galaxy (§1.3), where the mass accretion rates is of order  $\dot{M} \lesssim 10^{-5} - 10^{-6} M_\odot/\text{yr}$  far away from the central BH ([Baganoff et al., 2003](#)), while outflows decrease this to  $\dot{M} \lesssim 10^{-7} - 10^{-9} M_\odot/\text{yr}$  close to the horizon ([Marrone et al., 2007](#)). As ADAFs retain most of their internally dissipated energy, the ion temperature becomes almost virial  $T \approx GMm_p / 6k_B r \sim 10^{12} r_s/r$  K, with  $k_B$  Boltzmann’s constant, resulting in a ‘puffed-up’ disc structure, or rather, they become geometrically thick. As the pressure now increases with decreasing radius ( $P_g \propto r^{s-5/2}$ , where  $s$  is a dimensionless parameter between  $0 \leq s \leq 1$ ), the pressure gradient partly balances the gravitational pull of the BH, so that the flow becomes sub-Keplerian. Moreover, from Eqs. 14–17 we can find that  $v_r \propto \sqrt{P_g/\rho} H/r$ . Thus, in comparison to the thin disc,  $v_r$  becomes much larger, which, combined with the already low mass accretion rate, results in an optically thin disc ( $\tau \ll 1$ ). This has important observational consequences, as the optically thin nature of ADAFs allows radiative processes such as synchrotron, inverse-Compton and Bremsstrahlung emission to dominate the spectrum, rather than behave like a thermal black body.

Unlike thin discs, which rely heavily on the balance between radiation pressure and gravitational pull, ADAFs are characterised by more complex interactions between magnetic fields and gas dynamics in the

disc. While the MRI can explain how turbulent angular momentum transport is mediated through small and large-scale unstable feedback loops, it does not yet explain the large-scale magnetic field evolution and its effect on the disc. The self-similar solutions resulting from Eqs. 14–17 are only applicable to flat spacetime and do not describe the inner and outer boundaries of the flow. They also omit the dynamical evolution of the magnetic fields, which is essential in describing the dynamical nature of ADAFs. To accurately capture the effects of convection and outflows in the disc and find global solutions, we require large-scale numerical simulations capable of resolving all these dynamical, turbulent effects in curved spacetime. Global 2D and 3D general relativistic magnetohydrodynamical (GRMHD) simulations like HARM (Gammie et al., 2003), COSMOS++ (Anninos et al., 2005) or BHAC (Porth et al., 2017) have demonstrated that ADAFs exhibit complex, time-dependent behaviour including large-scale turbulence, jets, disc-winds and magnetically dominated areas (e.g. Gammie et al. 2004; McKinney 2006; Penna et al. 2010; Tchekhovskoy et al. 2011; Narayan et al. 2012).

The importance of magnetic field evolution is further emphasised by observational evidence, such as strong polarised synchrotron emission from the submm to NIR (e.g. Aitken et al. 2000; Marrone et al. 2006; Eckart et al. 2006), hinting at the importance of incorporating varying magnetic conditions into models. Moreover, many (LL)AGN launch collimated relativistic jets (Bridle and Perley, 1984), such as long-since observed in M87 (Curtis 1918; Baade and Minkowski 1954). These are thought to potentially be powered by magnetic field lines threading the event horizon and extracting energy from the black hole spin (Blandford and Znajek, 1977) or the accretion disc (Blandford and Payne, 1982). The inclusion of magnetic fields into numerical models has led to the distinction between the standard-and-normal-evolution (SANE) regime, where magnetic fields are assumed to be subdominant, and the magnetically arrested disc (MAD, Bisnovatyi-Kogan and Ruzmaikin 1976; Narayan et al. 2003), where the build-up of strong, dynamically changing magnetic fields is able to strongly affect or even inhibit the accretion of gas within some magnetospheric radius ( $R_m$ ), well outside the event horizon. For  $r > R_m$ , the flow is essentially axisymmetric, while for  $r < R_m$ , it breaks up into blobs and streams as the gas has to overcome the magnetic pressure of the magnetosphere, significantly lowering its radial velocity and increasing the radiative efficiency. MAD models are also capable of launching powerful jets (Tchekhovskoy et al., 2011) while intermittently halting accretion. This latter property may help explain the highly variable emission seen from Sgr A\*. Furthermore, highly polarised synchrotron emission (EHT Collaboration 2024a, 2024b) provides evidence for the presence of strong magnetic fields, making the MAD model a primary contender for Sgr A\*.

To link observational signatures to any of these aforementioned accretion regimes, we need to accurately model their emission properties. Since emission is largely determined by hot electrons in the disc, understanding their thermodynamics remains a major challenge in ADAF accretion modelling. More specifically, identifying the dominant heating mechanisms and understanding how dissipated energy is distributed between ions and electrons is still uncertain. Although early (unstable) models introducing two-temperature flows date back to the 70s (Shapiro et al., 1976), there remains a lack of consensus on their effective electron-ion heating mechanisms, especially under varying magnetic conditions such as encountered in MADs. Early models assumed a set fraction  $\delta_e$  of the internally dissipated energy to directly heat the electrons, where originally  $\delta_e$  was assumed to be  $\delta_e < 10^{-2}$ . However, more recent works estimate  $0.1 \lesssim \delta_e \lesssim 0.5$ , with Yuan et al. (2003) putting  $\delta_e \sim 0.5$  specifically for Sgr A\*, hinting that ADAFs may be less radiatively inefficient than previously thought, in line with expectations for MADs. To appropriately capture the electron heating rate and temperatures in the disc, one can then self-consistently evolve a separate electron fluid alongside a GRMHD simulation (Ryan et al., 2015). Rather than assuming a fixed heating rate, this is often derived from physical motivations such as turbulent MHD cascades (Howes, 2010; Kawazura et al., 2019) or magnetic reconnection heating (Rowan et al., 2017; Werner et al., 2018). Alternatively, one can ‘paint on’ the electron temperatures in post-processing by assuming some plasma-dependent ‘disc-jet’ parametrisation (Mościbrodzka et al., 2016), often referred to as the  $R(\beta)$  prescription. We provide a more detailed discussion of these temperature models in §2.2.

### 1.3 Sagittarius A\*

Sgr A\*, first discovered as a compact radio source by [Balick and Brown \(1974\)](#), is a supermassive BH in the Galactic Centre, believed likely to be a LLAGN. In quiescence its bolumetric luminosity is  $L_{bol} \sim 10^{35}$  erg/s, which translates to an extremely small Eddington ratio of  $L_{bol}/L_{Edd} = 1.9 \times 10^{-10}$  ([EHT Collaboration, 2022d](#)). Located at  $8.178 \pm 0.43\%$  kpc from Earth ([GRAVITY Collaboration, 2019](#)), it has the largest angular size on the sky compared to any other BH. This makes it a unique testbed for tests of GR and accretion disc models, prompting a long history of multi-wavelength observations. Recent large-scale collaborations such as [GRAVITY Collaboration \(2017\)](#) (optical and near-infrared [NIR]) and [EHT Collaboration \(2022a\)](#) (mm) have provided groundbreaking new insight into the fundamental nature of Sgr A\*. Through precise NIR astrometric measurements [GRAVITY Collaboration \(2019\)](#) were able to constrain its mass to  $4.152 \times 10^6 \pm 0.34\% M_\odot$ , consistent with mm-wavelength interferometric imaging ([EHT Collaboration, 2022a](#)) of the BH shadow ([Falcke et al., 2000](#)).

However, constraining the spin of Sgr A\* remains a major challenge due to the absence of strong spin-dependent observables resolvable with current instruments. The EHTs very-long baseline interferometry (VLBI) spatial resolution is unmatched, enabling mapping of the innermost regions of the accretion flow of  $r \lesssim 10 r_g$ . Although major progress has been made, numerical studies still rely on strong model assumptions. Continued improvements in observations, together with more sophisticated accretion models, could both improve our understanding of accretion physics and narrow down constraints on BH spin.

Strong lightcurve variability has long since been observed in Sgr A\*, with drastic changes across wavelengths (see e.g. [Genzel et al. 2010](#) for a review). Prominent X-ray flares were first observed by Chandra ([Baganoff et al., 2001](#)), lasting about 3 hours with an increased count rate of  $\sim 45$  compared to quiescence ([Baganoff et al., 2003](#)). Short-term variability has been linked to fluctuating events in the inner parts of the disc, which can help put constraints on the accretion and radiation mechanisms. Following this, XMM-Newton found even stronger X-ray flares of  $\sim 160$  times the quiescent flux ([Porquet et al., 2003](#)). Subsequently, flares were also detected in the NIR ([Genzel et al., 2003](#)), reaching flux increases of the order of  $\sim 10$  and exhibiting quasiperiodic substructures with periods of around  $\sim 30$  min, interpreted as a possible hot spot orbiting close to or at the ISCO of a spinning BH. However, other observations ([Meyer et al. 2008; Do et al. 2009](#)) have found the NIR emission to be consistent with a red noise power spectrum (of slope  $\sim 2$ ), in accordance with a stochastic disc model, where flares are explained as a superposition of statistical fluctuations. Furthermore, X-ray flares are often accompanied by a NIR counterpart, without the opposite necessarily holding true (e.g. [Do et al. 2009; Dodds-Eden et al. 2011; Witzel et al. 2018](#)). The absence of a clear sub-mm counterpart implies that flares are likely the result of highly energetic accelerated electrons where  $\gamma \sim 10^3$  ([Markoff et al., 2001](#)).

Recent observations from NIRCam on JWST find both continual short- and long-timescale variability, ranging from seconds to days and even potentially months ([Yusef-Zadeh et al., 2025](#)). This variability is consistent with synchrotron emission from hot electrons in magnetic fields of 40 to 90 Gauss, further hinting at the importance of magnetic fields in explaining the flaring behaviour of Sgr A\*. MAD models of Sgr A\* and M87 have become a topic of significant interest (e.g. [Gold et al. 2017; Chael et al. 2019, 2025; Salas et al. 2025](#)), owing to their success in explaining highly polarised emission from Sgr A\* and jets in M87, which is thought to be in a similar state as Sgr A\*, although varying on much longer timescales due to it being a factor of  $\sim 10^3$  more massive. In the context of Sgr A\*, MADs offer a promising framework to explain both the strong magnetic fields inferred from polarised emission and the rapid, variable infrared flares. They inherently produce highly ordered magnetic structures and concentrate much of their emission near the event horizon, making them attractive candidates for modelling NIR and X-ray variability.

## 1.4 This work

Due to its short timescales, large angular size and subsequent wealth of multi-wavelength observations available, Sgr A\* is our best target to study highly variable LLAGN. Despite decades of research, significant uncertainties remain regarding both Sgr A\*'s spin and the underlying accretion mechanisms driving the observed variability in the accretion flow.

Flaring activity in both X-rays and NIR bands is still poorly understood. Many previous numerical variability studies focus on the (sub-)mm or NIR emission, omitting Comptonization into X-rays, where observed flares are most profound. MAD models are frequently invoked in an attempt to explain the flaring variability observed in Sgr A\* (Chael et al., 2018; Dexter et al., 2020a; Mizuno et al., 2021). They represent an extreme regime of accretion, where magnetic fields become dynamically dominant. Unlike in SANEs, the accumulation of magnetic flux near the event horizon leads to episodic flux eruptions, which have increasingly been proposed to result in strong (non)thermal electron acceleration through magnetic reconnection (Rowan et al., 2017; Werner et al., 2018). Heating fractions are then derived from two-dimensional kinetic particle-in-cell calculations for trans-relativistic (Rowan et al., 2017) or relativistic (Werner et al., 2018) electrons. Such heating models can possibly better explain rapid flaring events through rapid, transient heating (Werner et al., 2019). Plasmoid formation in current sheets growing to macroscopic scales might then explain flares as hot spots orbiting close to the black hole (Ripperda et al. 2020, 2022), which would also require the disc to be in a MAD state.

However, the microphysics that determines magnetic reconnection prescriptions remains an approximate extrapolation from two-dimensional particle-in-cell (PIC) simulations. Such an approach relies on strong model assumptions like highly idealised anti-parallel reconnection. Realistic reconnection layers and current sheets in global accretion flows are likely three-dimensional, so that extrapolations from two-dimensional PIC simulations are perhaps not applicable to the global turbulent structure of GRMHD solutions. Some GRMHD-based approaches, such as Dexter et al. (2020b), apply nonthermal reconnection-inspired heating models, but within a thermal Maxwellian electron framework. While pragmatic in its approach, this disconnects the macroscopic thermal GRMHD assumptions from the microphysical, typically nonthermal nature of magnetic reconnection. Dexter et al. (2020a) study a wider range of MADs and SANEs with both turbulent and magnetic reconnection heating models. They find that SANEs with turbulent heating (resulting in a disc-jet structure, dominated by the jet wall) or MADs with reconnection heating (where emission is more spread out), can correctly reproduce Sgr A\*'s sub-mm spectral shape and variable NIR emission. Due to depolarisation of the turbulent SANE models, they favour their MAD magnetic reconnection heating models. However, their analysis remains limited to sub-mm and NIR.

EHT Collaboration (2022d) make use of the ad-hoc parametrised  $R(\beta)$  prescription to study both SANEs and MADs. They study a wide range of disc-jet coupling parameters. Although  $R(\beta)$  prescriptions were originally developed for SANEs, they find that MADs where temperatures are reasonably suppressed in the disc ( $R_{high} \geq 40$ ) are generally best at representing the quiescent emission. Their  $R_{high} \leq 10$  models consistently overpredict both NIR and X-ray emission. However, as their main focus is on the quiescent emission, their results lack detailed time-dependent variability modelling in NIR and X-rays.

As the literature is not converged on one physically motivated electron heating model and turbulent electron heating is likely to be present to some extent in the disc, we compare the turbulent electron heating model from Kawazura et al. (2019) with a wide range of  $R(\beta)$  prescriptions, each coupling to different regions in the accretion flow. Our primary goal is to investigate the extent to which  $R(\beta)$  prescriptions can recover the more complex thermodynamics of turbulent heating. As MAD flux eruptions have a strong dynamical effect on the disc, such as the formation of spiral structures (Dexter et al., 2020b) which may be important for the emission properties, we directly map each models dominant emission

regions assuming two widely varying spin cases ( $a_* = 0$  and  $a_* = 0.94$ ), applied to Sgr A\*. We compute spectral energy distributions (SEDs) and construct NIR and X-ray lightcurves to link our models back to observational signatures. Moreover, we asses the model-dependent spectral luminosity and variability and directly link these back to the underlying fluid properties in the emission regions, providing new insight into how MADs produce variable emission.

## 2 Numerical Model and Analysis Methodology

### 2.1 MAD GRMHD models

We post-process 3D MAD GRMHD simulations run using the code `ebhlight`<sup>3</sup> (an extension of `bhlight` from [Ryan et al. 2015](#)), which evolves the general relativistic radiation magnetohydrodynamics (GR-RMHD) equations using frequency-dependent radiative transfer, including synchrotron and inverse-Compton scattering. `ebhlight` is designed to take into account modest but non-negligible radiative effects in the accretion flow, such as potentially important for Sgr A\*. `ebhlight` combines the radiative transfer code `grmonty` ([Dolence et al., 2009](#)) with the GRMHD routine from `harm` ([Gammie et al., 2003](#)). For a detailed discussion on the numerical setup used in this work, we refer to §2 of [Mościbrodzka \(2025\)](#).

We omit a detailed overview of the GR(R)MHD equations, but shortly link them to Eqs. 14-17 (see also [Misner, Thorne, and Wheeler 1973](#); [Gammie et al. 2003](#); [Ryan et al. 2015](#)). Assuming a co-moving frame rest mass density  $\rho_0$  and metric determinant  $g$ , the GRMHD analogue to mass conservations Eq. 14 becomes

$$\nabla_\mu (\rho_0 u^\mu) = 0 \quad \xrightarrow{\text{in a coordinate basis}} \quad \frac{1}{\sqrt{-g}} \partial_\mu (\sqrt{-g} \rho_0 u^\mu) = 0, \quad (18)$$

with  $u^\mu$  the fluid four-velocity. This is also often referred to as the continuity or particle number conservation equation. The relativistic version of the energy and momentum conservation equations (Eqs. 15-17) is then compacted into

$$\nabla_\mu (T_\nu^\mu + R_\nu^\mu) = 0 \quad \xrightarrow{\text{in a coordinate basis}} \quad \partial_\mu (\sqrt{-g} T_\nu^\mu) = \sqrt{-g} T_\lambda^\kappa \Gamma_{\nu\kappa}^\lambda + \sqrt{-g} G_\nu, \quad (19)$$

where  $T_\nu^\mu$  and  $R_\nu^\mu$  are the magnetohydrodynamic (MHD) and radiation stress-energy tensors, respectively, and  $G_\nu = -\nabla_\mu R_\nu^\mu$  is the radiation four-force density.  $R_\nu^\mu$  then describes the radiation field and  $T_\nu^\mu$  the magnetised fluid, which are coupled through emission, absorption and scattering of photons. The MHD stress-energy tensor further expands upon Eqs. 15-17 by combining both the fluid and electromagnetic stress-energy tensor ( $T_\nu^\mu = T_{\nu, \text{fluid}}^\mu + T_{\nu, \text{EM}}^\mu$ ) to also include the dynamical effects of the magnetic field. In the ideal MHD limit (i.e. assuming the plasma is highly conductive such that the electric field is negligible), the MHD stress-energy tensor becomes

$$T_\nu^\mu = (\rho_0 + u + P_g + b^2) u^\mu u_\nu + \left( P_g + \frac{1}{2} b^2 \right) g_\nu^\mu - b^\mu b_\nu, \quad (20)$$

where  $u$  is the internal energy and  $b^2 = b^\mu b_\mu$ , with  $b^\mu$  the magnetic field four-vector. The gas pressure ( $P_g$ ) is subject to the equation of state  $P_g = (\gamma - 1)u$ . Expressions for  $R_\nu^\mu$  and  $G_\nu$  are not straightforward and are given in §2.3 of [Ryan et al. \(2015\)](#). As this work revolves around low-density optically thin ( $\tau \ll 1$ ) gas, radiative pressure is assumed to have minimal effect on the physical evolution of the disc. Moreover, [Mościbrodzka \(2025\)](#) found radiative cooling to be negligible for turbulent two-temperature MAD models of Sgr A\*. We thus omit both in this work (i.e. assuming  $R_\nu^\mu = 0$ ), simplifying the output to solutions for the standard GRMHD equation.

We make use of geometrized units ( $c = G = 1$ ), such that the simulation length- and timescale are set by the BH mass  $M$ . These then relate back to e.g. cgs length and time units following

$$\mathcal{L} \equiv \frac{GM}{c^2} = M, \quad (21)$$

and

$$\mathcal{T} \equiv \frac{GM}{c^3} = M, \quad (22)$$

---

<sup>3</sup><https://github.com/AFD-Illinois/ebhlight>

respectively. Simulations are carried out in funky modified Kerr-Schild (FMKS) logarithmic coordinates  $x^\mu = (x^0, x^1, x^2, x^3)$ , which are an extension of the already modified Kerr-Schild (MKS) coordinates (Gammie et al., 2003). The justification behind these additional modifications is that they increase the effective resolution close to the horizon and in the disc midplane, where we want to accurately capture physical effects. FMKS coordinates simultaneously reduce resolution near the poles by expanding cells in the  $\theta$  direction at small radii through ‘cylindrification’ (see Tchekhovskoy et al. 2011). This is particularly useful as otherwise, near the jet funnel, the signal-crossing timescale for individual cells is rather small (as the fluid becomes highly relativistic), significantly lowering the numerical time step of the simulation. A more in-depth discussion on FMKS coordinates is somewhat detailed and can be found in the Appendix of Wong et al. (2021). Our simulation grid extends from the event horizon to  $r = 1000 M$ . The disc is initialised from a Fishbone-Moncrief torus (Fishbone and Moncrief, 1976) in hydrostatic equilibrium, with the torus’ inner radius at  $r_{in} = 20 M$  and the maximum-pressure-radius at  $r_{max} = 41 M$ . A weak poloidal magnetic field threads the torus, defined only by the azimuthal magnetic vector potential as

$$A_\phi = \frac{\rho}{\rho_{max}} \left( \frac{r}{r_{in}} \right)^3 \exp \left( \frac{r}{400} \right) \sin^3 \theta - 0.2, \quad (23)$$

where  $\rho_{max}$  is the plasma density at pressure maximum in the centre of the torus. To ensure a MAD state, the initial magnetic field is rescaled so that  $\beta_{max} = 100$ . Here we assume the plasma to have a constant overall adiabatic index of  $\gamma = 13/9$ , consisting only of non-relativistic protons ( $\gamma_p = 5/3$ ) and relativistic electrons ( $\gamma_e = 4/3$ ). We study two BH spins, namely  $a_* = 0.94$  ( $r_+ \approx 1.35 M$ ) in the Kerr spacetime and a non-spinning  $a_* = 0$  ( $r_h = 2.0 M$ ) Schwarzschild BH. A resolution study shows physical effects are converged around grid resolutions of  $(N_r, N_\theta, N_\phi) = (266, 120, 128)$  for  $a_* = 0.94$  and  $(240, 120, 128)$  for  $a_* = 0$  (see §2.4 of Mościbrodzka 2025 for details). The disc is evolved until  $30000 M$ , reaching steady-state within  $20 M$ . Outputs are recorded every  $10 M$ . Disc and face-on slices of our GRMHD models at  $t = 20000 M$  are presented in Fig. 4.

## 2.2 Electron temperature prescriptions

As the thermodynamics of electrons governs the radiative properties of the plasma, understanding the mechanism behind their heating is essential for characterising the disc. Rather than assuming a fixed electron-to-ion temperature ratio, we make use of a physically motivated electron heating method from Ressler et al. (2015). This approach self-consistently evolves an electron entropy equation modelled alongside the GRMHD simulation of the plasma. The electrons are then modelled as a separate fluid with independent internal energy from the ions in the flow. Such an implementation can incorporate the effects of the local magnetic field and thermal conduction between electrons, and in doing so can significantly alter the electron temperature in the inner regions of the flow.

This does, however, require an additional underlying electron heating model that determines what fraction of the energy recaptured from grid-scale dissipation goes into the electrons’ internal energy. A common assumption is that heating in astrophysical plasmas is caused by the kinetic dissipation of Alfvénic turbulence. Gyrokinetic modelling of anisotropic cascades can then be used to retrieve the ratio of ion-to-electron heating ( $Q_i/Q_e$ ). Howes et al. (2008) applied this to model solar winds, which was later extended to include a wider range of (non-relativistic) astrophysical plasmas by Howes (2010). Heating then strongly depends on the ratio of the gas-to-magnetic pressure

$$\beta \equiv P_{gas}/P_B \quad (24)$$

and mildly on the ion-to-electron temperature ratio  $T_i/T_e$ .

We here make use of a more recent model from Kawazura et al. (2019) (hereinafter K-model), which

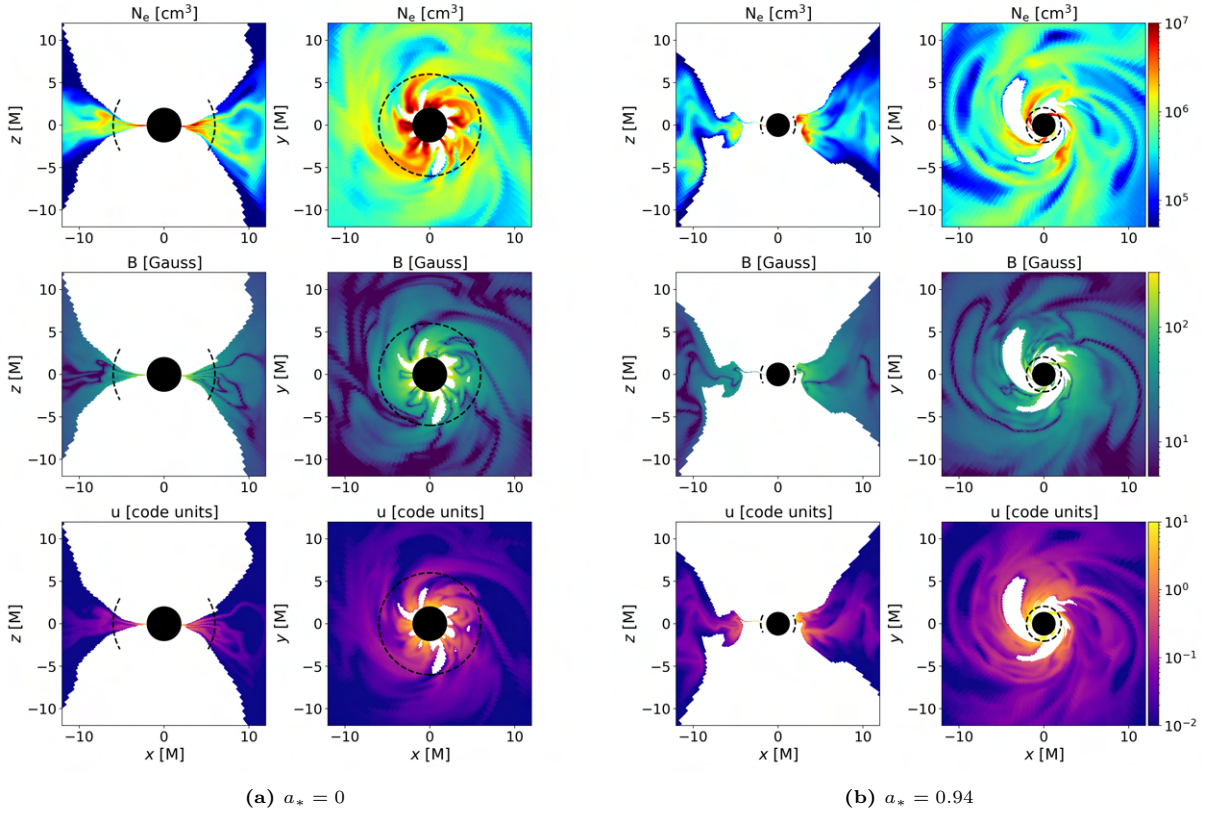


**Figure 4:** disc and face-on meridional and equatorial slices of the electron density in number density ( $N_e$ ), magnetic field strength (B) and internal energy (u) for both BH spin cases at  $t = 20000 M$ . The model density ( $\mathcal{M}$ ) used to rescale back to physical units is set to that of the K-model (Table 1 in §2.4). Dashed black lines represent the ISCO. White zones are masked as  $\sigma > 1$  and excluded from our analysis (see §2.3 for details).

further refines this heating framework for turbulent magnetised plasma using nonlinear gyrokinetic simulations, more in line with the radiatively inefficient ADAF. The heating fraction then also heavily depends on  $\beta$ , such that electrons are preferentially heated in highly magnetised ( $\beta \lesssim 1$ ) regions, whereas protons gain the bulk of the thermal energy in gas-pressure dominated ( $\beta \gtrsim 1$ ) regions (see also Fig. 1 from Chael et al. 2018, who demonstrate this for the similar heating model from Howes 2010). The ion-to-electron heating fraction is calculated through

$$\frac{Q_i}{Q_e} = \frac{35}{1 + \left(\frac{\beta}{15}\right)^{-1.4} e^{-0.1 \frac{T_e}{T_i}}}, \quad (25)$$

which also weakly depends on  $T_i/T_e$ . Due to its turbulent nature, the plasma develops thermal, but spatially varying temperature distributions, shaped by the local fluid and magnetic environment. Ressler et al. (2017) showed how turbulent electron heating models can naturally lead to coupled disc-jet structures in highly magnetised (but not quite MAD) models of Sgr A\*. Low-frequency radio emission then comes from along the jet-sheath, whereas frequencies above 100 GHz typically originate from the inner regions in the accretion disc (although frequencies below  $\lesssim 230$  GHz are optically thick). In contrast, rather than relying on turbulent cascades, one can adopt a model where electrons get accelerated through magnetic reconnection events. Such heating models can possibly better explain rapid flaring events through rapid, transient heating (Werner et al., 2019)<sup>4</sup>.

<sup>4</sup>For relativistic electrons, this typically leads to a power law distribution  $N(\Gamma) \propto \Gamma^{-\alpha}$ , with  $\Gamma$  the Lorentz factor and  $\alpha \sim 1.2$  (Werner et al., 2016). Particles can then be accelerated in plasmoids, which are in turn formed in highly localised current sheets (e.g. Ripperda et al. 2020, 2022). The fraction of the total dissipated energy that goes into the electrons is dependent on the plasma's dimensionless magnetisation parameter  $\sigma \equiv b^2/\rho$ , with  $b = \sqrt{b^\mu b_\mu}$  the magnetic field strength and  $\rho$  the density. Two-dimensional kinetic particle-in-cell calculations show that for nonthermal relativistic electrons

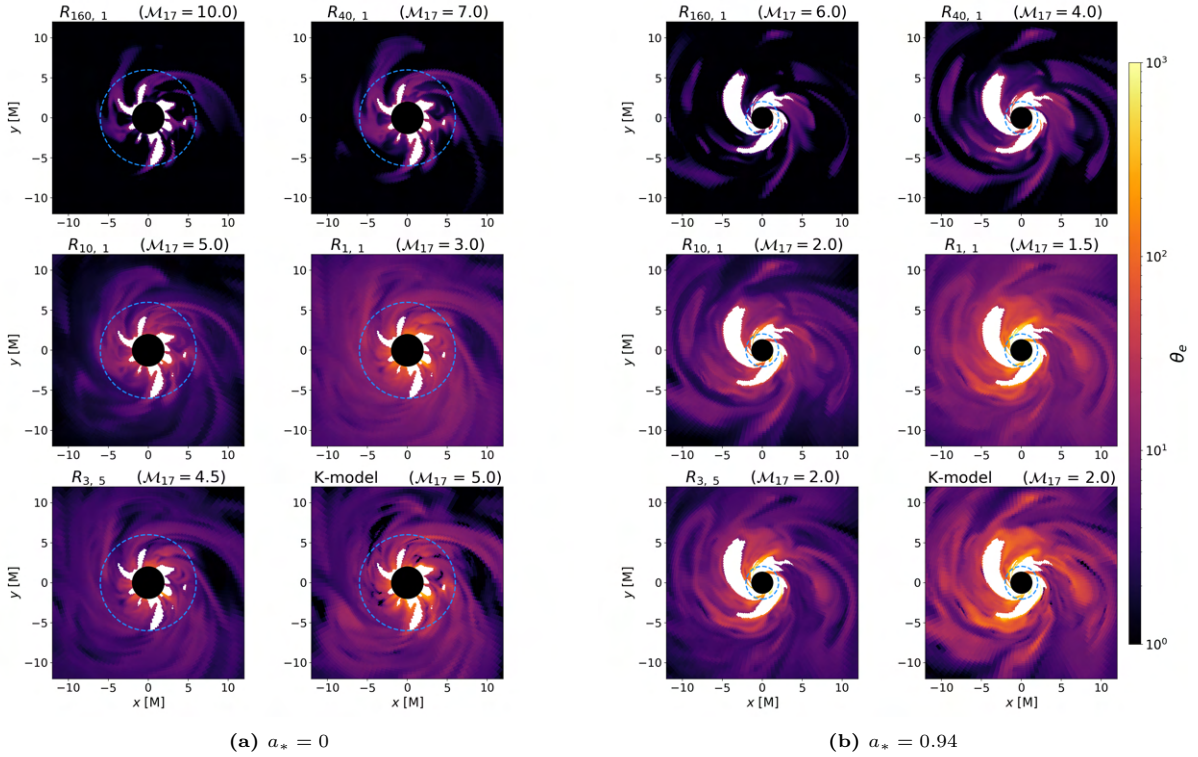


**Figure 5:** Face-on equatorial slices of different electron temperature models in units of rest mass ( $\Theta_e = k_B T / m_e c^2$ ) for both BH spin cases at  $t = 20000 M$ . The simulation's specific model density unit is denoted by  $M_{17} \equiv M/10^{17}$  (Table 1 in §2.4). In both panels (a) and (b) from top left to bottom right are the  $R_{160,1}$ ,  $R_{40,1}$ ,  $R_{10,1}$ ,  $R_{1,1}$ ,  $R_{3,5}$  and K-model. Dashed blue lines represent the ISCO. White zones are masked as  $\sigma > 1$  and excluded from our models (see §2.3 for details).

We compare this turbulent heating model to another popular, physically ad-hoc motivated approach, where electron temperatures are directly parametrised from the underlying ion(/proton) temperature, assuming a dependence only on  $\beta$  (Mościbrodzka et al., 2016). The parametrisation relies on three free parameters:  $\beta_{crit}$ ,  $R_{high}$  and  $R_{low}$ , which respectively determine the critical transition  $\beta$ , the coupling strength in gass-pressure dominated ( $\beta \gg \beta_{crit}$ ; high  $\beta$ ) and magnetic-pressure dominated ( $\beta \ll \beta_{crit}$ ; low  $\beta$ ) plasma. Setting  $b \equiv \beta/\beta_{crit}$ , the temperature ratio becomes

$$R(b) = \frac{T_i}{T_e} = R_{high} \frac{b^2}{1+b^2} + R_{low} \frac{1}{1+b^2}. \quad (26)$$

This allows one to artificially subdue electron temperatures in the inner dense (disc) regions ( $\beta \gg \beta_{crit}$ ) of the flow by setting  $R_{high} \gg 1$ , reducing the coupling strength. Temperatures then couple more strongly in the highly magnetised (jet) regions of the flow where  $\beta \lesssim \beta_{crit}$ . Moreover, this approach does not require the need for additional modelling of electron temperatures alongside the GRMHD simulation and allows for a variety of regions in the disc to be highlighted, depending on the choice of parameters. We will often refer to such parametrised models as  $R(\beta)$ -prescriptions, which are here denoted as e.g.  $R_{3,5}$  for  $R_{high} = 3$  and  $R_{low} = 5$ . We limit our selection to five  $R(\beta)$ -prescriptions:  $R_{1,1}$ ,  $R_{10,1}$ ,  $R_{40,1}$  and  $R_{160,1}$  and set  $\beta_{crit} = 1$  to compare to previous literature (e.g. Mizuno et al. 2021; EHT Collaboration 2022d) and an additional  $R_{3,5}$  model which we find to closely resemble radiative properties of the K-model (although arguably closer fits may be achieved by further tweaking  $R_{high}$  and  $R_{low}$ ). In Fig. 5 we present the varying temperature distributions produced by our  $R(\beta)$ -prescriptions and the K-model.

$\delta_e = 1/4 \left( 1 + \sqrt{0.2\sigma/(2+0.2\sigma)} \right)$  (Werner et al., 2018).

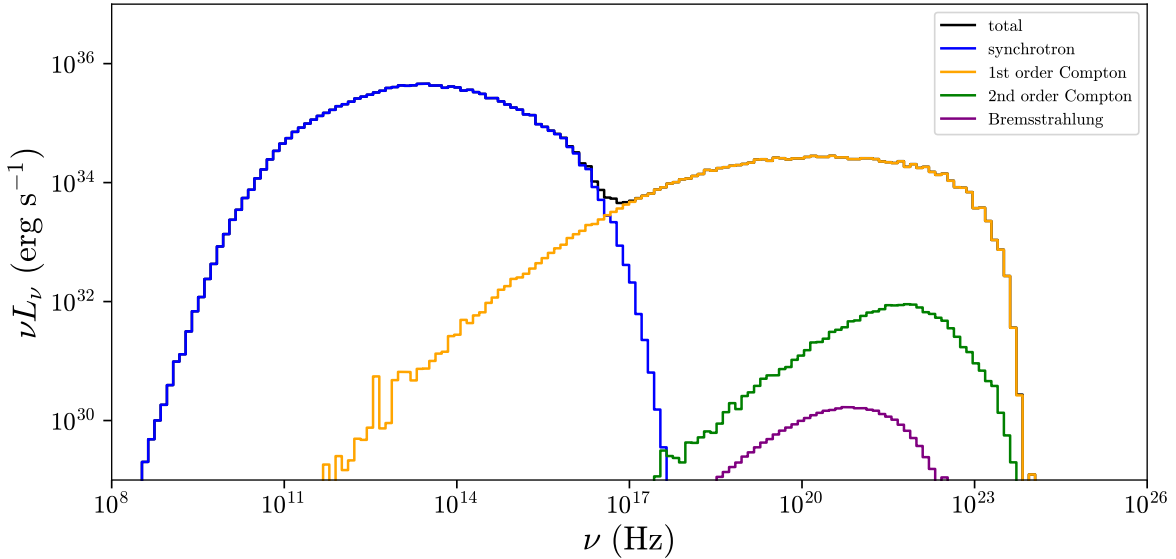


**Figure 6:** Example SED constructed from a single  $a_* = 0.94$  GRMHD time slice using the K-model. The blue, yellow, green and purple lines show the synchrotron, 1st order Compton, 2nd order Compton and Bremsstrahlung contributions to the spectrum. The black line represents the summed total across all emission types. Across our simulations, dominant emission is consistently smooth around sub-mm, NIR and X-ray frequency domains.

### 2.3 Radiative transfer

We make use of the Monte Carlo code `grmonty`<sup>5</sup> (Dolence et al., 2009), which is specifically suited to solve radiative transport problems for optically thin systems in the Kerr- and Schwarzschild spacetimes. Rather than treating individual photons, so-called superphotons are sampled to keep the code computationally viable. Intuitively, these can be thought of as photon-packets, each assigned a weight  $w$  ( $w \gg 1$ ), coordinate  $x^\mu$  and wave vector  $k^\mu$  upon creation, where weights are the scaling ratios  $w \equiv dN/dN_s$  between photons ( $N$ ) and superphotons ( $N_s$ ). `grmonty` then assumes azimuthal and equatorial symmetry by recording photons through artificial ring-like detectors within polar-angle bins  $\Delta\theta = 90^\circ/N_{\theta-\text{bins}}$ , where  $N_{\theta-\text{bins}}$  is set by the user. The program incorporates continuum emission from strictly thermal synchrotron, inverse-Compton scattering and Bremsstrahlung. Only synchrotron and free-free emission are sources of superphotons. Compton scattering is incorporated through individual interactions with sourced superphotons. When, e.g. a synchrotron superphoton is upscattered, its weight is reduced and a more energetic upscattered photon is launched while the original continues on its trajectory. We can thus have a one-to-one synchrotron to Compton scattering ratio, without losing sampling efficiency in the synchrotron-dominated parts of the spectrum. The contribution of each detected superphoton to the SED is scaled by the photon weight. The code’s output contains 200 logarithmically scaled frequency bins, allowing for substantial spectral resolution. Additionally, emission types are binned, so that it is straightforward to separate their contributions to the SED (e.g. distinguish synchrotron from Compton). An example SED is shown in Fig. 6.

We scale the BH mass to that of Sgr A\* ( $\sim 4.1 \times 10^6 M_\odot$ , GRAVITY Collaboration 2020; EHT Collaboration 2022a). For each electron temperature prescription, we fit the simulation to the observed 1.3 mm flux (Wielgus et al., 2022) by adjusting the simulation density unit  $\mathcal{M}$  accordingly. These can be scaled back from code to physical units through

$$\rho_{\text{physical}} = \frac{\mathcal{M}}{\mathcal{L}^3} \rho_{\text{code}}. \quad (27)$$

<sup>5</sup><https://github.com/AFD-Illinois/igrmonty>

As EHT Collaboration (2022b) finds the mm emission to be compact, we omit extended emission from our models and only assume a thermal electron distribution. As such, we do not expect Bremsstrahlung to play a significant role, but do include it in our models.

Superphotons are propagated and tracked throughout the disc until they are either absorbed, advected ( $r \leq r_{h,+}$ ), scattered or escape the system at  $r > 1000 M$ . Sampling of synchrotron superphotons is dependent on the local emissivity  $j_\nu$  from Leung et al. (2011). Absorption is treated deterministically, so that throughout the simulation, weights decay as

$$w_{n+1} = w_n e^{-\tau_a}, \quad (28)$$

with  $\tau_a ((\nu\alpha_{\nu,a})_n)$  the absorption optical depth depending on the invariant opacity  $(\nu\alpha_{\nu,a})_n$  and subsequently on the absorption coefficient  $\alpha_{\nu,a}$  evaluated in the fluid frame. The code's treatment of Compton scattering differs significantly, in that it uses a biased probability distribution so that

$$p_s = 1 - e^{-b\tau_s}, \quad (29)$$

with  $\tau_s$  the scattering optical depth and  $b$  the bias parameter further discussed in Appendix A. We arbitrarily impose a limit on the magnetisation in the flow by excluding all emission from regions where  $\sigma > 1$ . This is done to keep the code conservative, as small errors in the total (magnetically dominated) energy can lead to strong diverging errors in the internal energy and in turn the proton and electron temperatures. In other words, our turbulent thermodynamical models break down in these highly magnetised, low-density regions, such as inside the jet.

## 2.4 Analysis specifics

We analyse radiative properties of MADs in both a Schwarzschild ( $a_* = 0$ ) and Kerr ( $a_* = 0.94$ ) BH. Table 1 gives an overview of the analysed temperature models and their respective model density unit  $\mathcal{M}$ . The post-processed sample from the GRMHD simulation is limited to 500 snapshots between 20000 and 24990  $M$ , each separated by  $\Delta M = 10$  ( $\sim 200$  seconds when scaled to Sgr A\*). There, the flow has long since reached steady state and is relaxed from initial conditions. Moreover, we expect all photon trajectories to be fully evolved by that time, such that we can make use of the fast-light approximation (i.e. we do not evolve the underlying fluid from the GRMHD simulations during the `grmonty` run).

Runs in `grmonty` are conducted with  $\sim 3 \times 10^7$  sourced superphotons. We adjust the scattering bias (Appendix A) to ensure that the ratio of Compton upscattered to sourced superphotons remains approximately between 1:1 and 3:1, which consistently results in smooth, converged spectra.

Although the inclination angle of Sgr A\* with respect to our line of sight remains partly unconstrained, recent findings favour inclination angles where  $i > 150^\circ$  (EHT Collaboration 2022c; EHT Collaboration 2022d) with Yfantis et al. (2024) finding a best-fitting hot-spot viewing angle of  $i \in [155, 160]^\circ$ . To balance angular resolution with computational efficiency, we set  $N_{\theta-\text{bins}} = 6$ , limiting the  $\Delta\theta$ -resolution to  $\theta \in [150, 165]^\circ$ . We assume azimuthal symmetry, so that  $\phi \in [0, 360]^\circ$ , without additional constraints. The validity of this latter assumption is further examined in Appendix C.

In our analysis, we compute the time-averaged SED contribution and mean emission radius for each emission type across all snapshots (coloured lines Figs. 7 and 8). We also use the total averaged SEDs and minimum to maximum ranges reached to compare temperature prescriptions in Fig. 14 (thick lines).

In addition to the standard output from `grmonty`, we extend the code to track each recorded superphoton's origin in KS coordinates, allowing for a precise mapping of the emission zones. Moreover,

**Table 1:** Analysed electron temperature models and specific simulation densities ( $\mathcal{M}$ ) for both BH spin cases.

Model	$R_{high}$	$R_{low}$	$\mathcal{M}_{a_*=0} / 10^{17}$	$\mathcal{M}_{a_*=0.94} / 10^{17}$
K	-	-	5	2
$R_{3,5}$	3	5	4.5	2
$R_{1,1}$	1	1	3	1.5
$R_{10,1}$	10	1	5	2
$R_{40,1}$	40	1	7	4
$R_{160,1}$	160	1	10	6

this enables the tracking of local fluid parameters at the emission locations such as the plasma electron number density, magnetic field strength and proton temperature (Figs. 9 and 10). We do note that the output generated by this extension demands significantly more computational storage. Rather than incorporate this routine in our primary set of runs, we rerun an equivalent but low-resolution version of our primary models. Enforcing an upscattering ratio of 1:1 (by tweaking the bias function accordingly, Appendix A) and setting the code to source  $\sim 3 \times 10^6$  synchrotron superphotons, the code records about  $\sim 4 \times 10^6$  superphotons. Each individual time slice then takes up  $\sim 60$  MB, about  $\sim 100$  times `grmonty`'s normal output. We integrate the SEDs ( $L = \int \nu L_\nu d\nu / \nu$ ) to retrieve near-infrared (NIR, 30-3  $\mu\text{m}$ ) and X-ray (2-8 keV) lightcurves. From these, we compute the total fractional root-mean-square variability through  $\text{var}_{\text{rms}}(L) = \sigma / \langle L \rangle$  (§3.2), where  $\sigma$  is the standard deviation and  $\langle L \rangle$  the mean luminosity. We compute spectral power densities (PSD) through the periodogram function from the SciPy signal library<sup>6</sup> (Virtanen et al., 2020), with a sampling frequency of  $f_s = 0.1$  and FFT length of  $n_{fft} = 2^{12}$  to smoothly analyse even the lowest frequencies. Autocorrelations are found by mirroring the PSD, concatenating the arrays and taking the Fourier transform, which is then normalised. Cross-correlation functions (CCFs) are computed by first subtracting the data's mean, dividing by its standard deviation and applying SciPy's correlate function. If  $x$  and  $y$  represent our data arrays, this computes the correlation according to<sup>7</sup>

$$\text{CCF}[k] = \sum_{l=0}^{\|x\|-1} x_l y_{l-k+N-1}^*, \quad (30)$$

for  $k = 0, 1, \dots, \|x\| + \|y\| - 2$ . For our models,  $\|N\| = \|x\| = \|y\|$  is the length of the input arrays.  $y^*$  denotes the complex conjugate of  $y$ , which is zero outside the range of the array. We normalise the CCF by dividing by the square root of the product of the zero-lag autocorrelations of  $x$  and  $y$ , denoted by  $R_x(0)$  and  $R_y(0)$ , such that

$$\text{CCF}_{norm}[k] = \frac{\text{CCF}[k]}{\sqrt{R_x(0) R_y(0)}}, \quad (31)$$

which retains the relative strength of the correlation.

We include an additional constraint, as in our  $a_* = 0.94$  GRMHD simulations, strong disc outbursts result in occasional dense ‘blobs’ propagating along the jet. These result in intra-jet regions where  $\beta \gg 1$ , such that inside these structures  $\sigma < 1$ . Consequently, the spectrum past  $\sim 10$  keV becomes dominated by an additional population of extremely hot electrons at radii past  $r \gg 100 M$ , where the grid resolution is low. To ensure our SEDs and lightcurves are not significantly affected by these regions, we artificially set the electron temperature to  $\Theta_e \approx 0$  past  $100 M$ , only for  $a_* = 0.94$  models.

<sup>6</sup><https://docs.scipy.org/doc/scipy/reference/signal.html>

<sup>7</sup>See also <https://docs.scipy.org/doc/scipy/reference/generated/scipy.signal.correlate.html>

### 3.1 Radiative properties of MADs

We present an overview of all computed SEDs in the left two columns of Figs. 7 ( $a_* = 0$ ) and 8 ( $a_* = 0.94$ ), with the associated average emission radius depicted in the respective right two columns. Nearly all dominant NIR and X-ray emission originates from within  $10 M$ . Toward increasing  $R_{high}$ , we find a clear decrease in total emission past the normalisation frequency of 230 GHz. All models exhibit a general two-bump spectrum, except for  $R_{\geq 40, 1}$  where 1st-order Compton cuts off at  $10^{19}$  Hz, past which 2nd-order Compton and Bremsstrahlung take over, resulting in a small third spectral bump. This occurs as bremsstrahlung emissivity is proportional to  $j_{\nu, b} \propto N_e^2 \Theta_e^{1/2}$  for  $\Theta_e > 1$ , whereas the Comptonization fractional energy gain per scattering scales with  $\Theta_e^2 \tau_s$ , with  $\tau_s$  the electron scattering optical depth. As  $R_{high}$  increases, the disc temperature decreases. This, together with the increase in model density (to keep consistent with the normalisation flux at 1.3mm), then shifts the Bremsstrahlung peak to the right while the cool electrons become incapable of Comptonization past  $10^{19}$  Hz. However, within our studied frequency ranges, only synchrotron and 1st-order Compton emission are relevant. For simplicity, we will thus refer to 1st-order Compton scattering simply as Compton emission and drop further classification. In our models, Compton upscattering is only the result of synchrotron self-Compton (SSC). As  $R_{high}$  increases, both synchrotron and Compton components cut off at lower frequencies, such that the transition towards Compton occurs in the ultraviolet for  $R_{1,1}$ , while in the near-infrared for  $R_{160,1}$ . We note that the frequency and luminosity where these transitions occur are mostly independent of BH spin and only depend on the assumed temperature model. Compton spectra for  $R_{40,1}$  and  $R_{160,1}$  models peak in soft X-rays ( $< 2$  keV), whereas all other models peak toward harder X-rays ( $> 2$  keV), gradually increasing in hardness with decreasing  $R_{high}$  and increasing  $\Theta_e$ . As a result, the integrated part of the spectrum used to calculate X-ray light curves (2-8 keV, §3.2) exhibit different  $\nu L_\nu$  spectral slopes [ $\equiv d \log(\nu L_\nu) / d \log(\nu)$ ], which is typically positive for  $R_{\leq 10, \leq 5}$  while negative for  $R_{\geq 40, 1}$  (see also Fig. 14, where this frequency range is denoted by vertical dash-dotted blue lines).

We find that both MAD simulations produce significant NIR and X-ray variability, as expected for Sgr A\* (see §3.2 for a quantitative analysis), with some temperature models spanning over two orders of magnitude. In general, variability decreases with increasing  $R_{high}$  for  $a_* = 0$  models, while this is not at all evident for  $a_* = 0.94$  models. The emission regions in both non-spinning and high spin models are differentiable by their averaged radial coordinate (right two columns of Figs. 7 and 8). For  $a_* = 0$ , relevant synchrotron emission past  $\sim 10^{12}$  Hz originates primarily from inside the ISCO. The transition frequency from the averaged synchrotron to Compton component in the SED almost exactly matches the frequency where the Compton average emission radius coincides with the ISCO radius. All dominant Compton emission past this frequency has its origin, on average, inside the ISCO. This is reversed for high-spin models, where the average emission radius of the relevant emission always exceeds the ISCO radius.

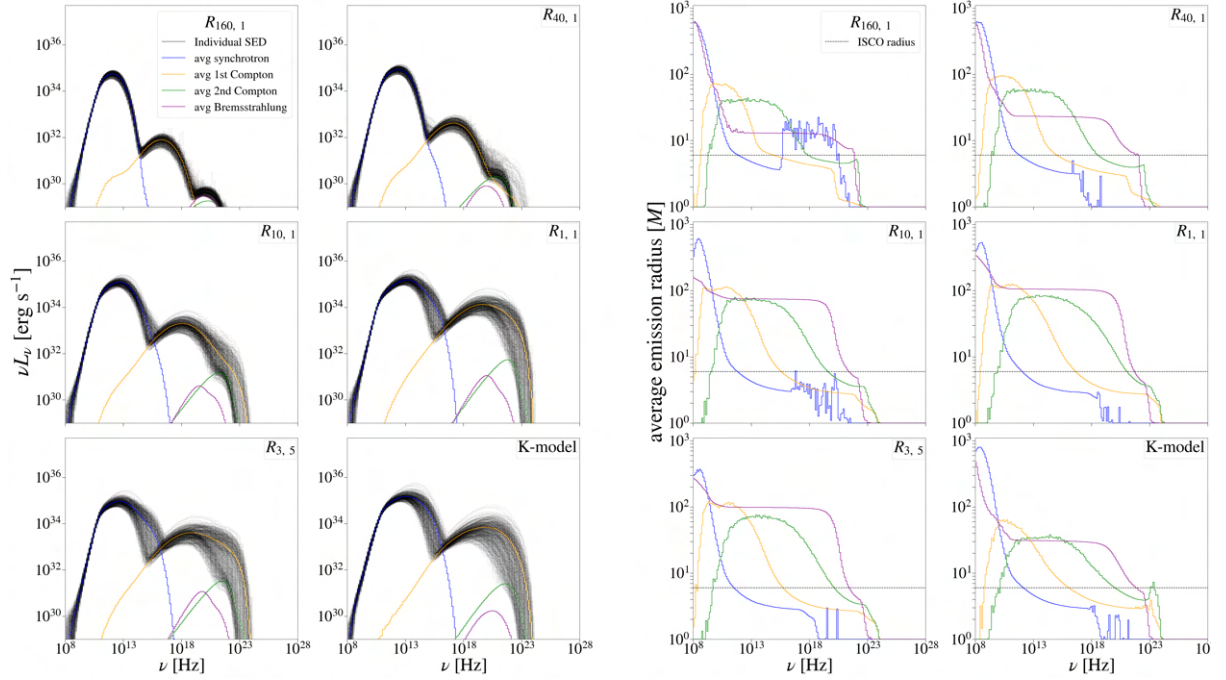


**Figure 7:** *Left two columns:* All individual SEDs (black lines) for our  $a_* = 0$  model. Each subplot represents an electron temperature model. On the top row are respective  $R_{160,1}$  and  $R_{40,1}$  models; on the middle row  $R_{10,1}$  and  $R_{1,1}$ ; and on the bottom row the  $R_{3,5}$  and K-model. The overplotted blue, yellow, green and purple lines represent the corresponding time-averaged contributions from respective synchrotron, 1st-order Compton, 2nd-order Compton and Bremsstrahlung continuum emission. *Right two columns:* The average radius of emission per type of continuum emission, with each subplot representing a temperature manner analogous to the left two columns. Dashed lines correspond to the ISCO radius.

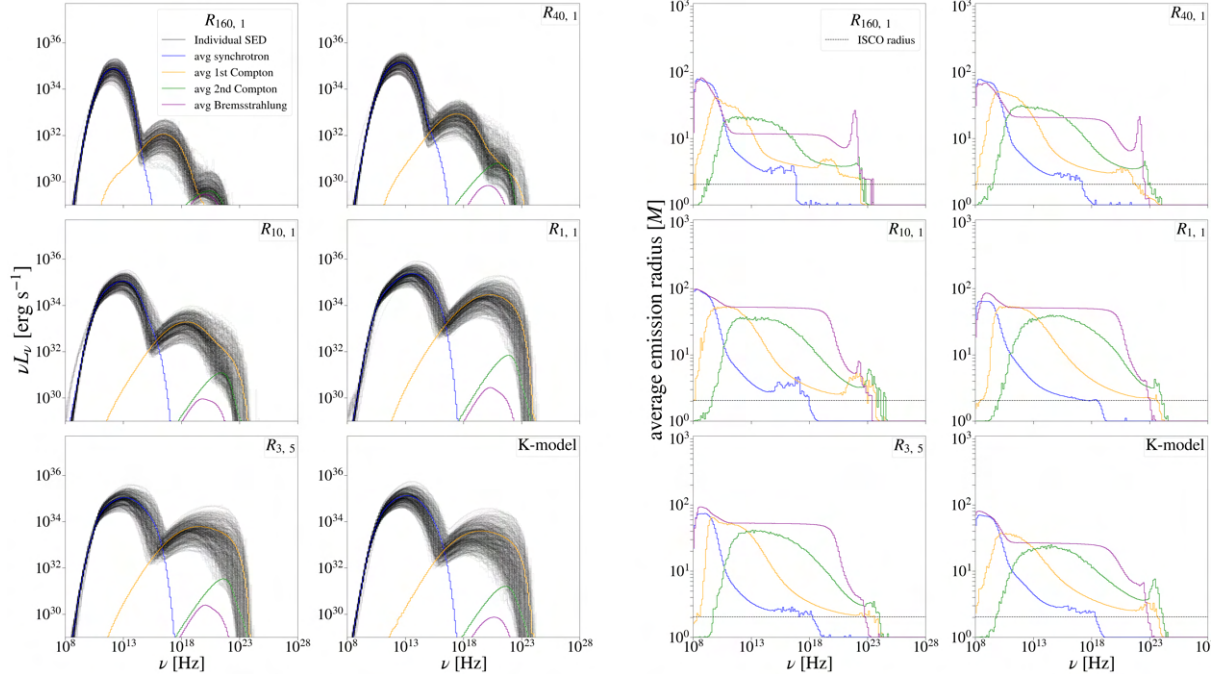


**Figure 8:** Same as in Fig. 7, but for  $a_* = 0.94$ . Note that although a radio jet is present in our models, we here cut out all emission past  $r > 100 M$ .

Figs. 9 and 10 show emission maps for a single time slice of both  $a_* = 0$  and  $a_* = 0.94$  MAD models respectively. These are constructed by individually tracing all recorded superphotons that normally compose a SED (albeit at a lower spectral resolution). We then show the superphoton emission origin with

their local plasma electron temperature ( $\Theta_e$ ) and magnetic field strength ( $B$ ) as a function of electron number density ( $N_e$ ). The bulk of the emission is typically confined to within  $5 M$ , regardless of BH spin. For both BH spin models, the electron temperatures of the K-model are best reproduced by the  $R_{\leq 3, \leq 5}$  prescriptions at comparable magnetic field strength, although these still overheat the electrons to some extent and a sizable fraction of electrons in the  $R_{1,1}$  prescription reach the imposed temperature ceiling of  $\Theta_e = 10^3$ . The  $R_{160,1}$  prescription exhibits a clear temperature cutoff past  $\Theta_e \approx 30$  for both BH spin models. As a general comparison to the K-model, the  $R_{\leq 3, \leq 5}$  prescriptions slightly overheat, while  $R_{10,1}$  somewhat underheats. The  $R_{\geq 40, 1}$  prescriptions strongly underheat, limiting temperatures and restricting Comptonization into X-rays.

Another immediate observation is the mostly synonymous origin of synchrotron and Compton emission. We further look into this in Fig. 11(a)-(d), where we plot four frequency ranges during the most luminous part of both the  $a_* = 0$  and  $a_* = 0.94$  NIR and X-ray lightcurves (discussed in §3.2). In general, emission becomes increasingly confined toward higher frequencies. As expected, sub-mm emission shifts toward more extended regions of the disc, where temperatures are lower.

For both BH spin models, we generally associate high frequency emission with hot plasma that has been shocked by outward propagating flux eruptions in the disc. For  $a_* = 0$ , these appear as co-rotating hot spots, while for  $a_* = 0.94$  models they stretch out into spiral arms (Tchekhovskoy et al., 2011; Dexter et al., 2020b). This connection is perhaps best demonstrated in the  $\theta$ -averaged GRMHD snapshot shown in Fig. 11(e) and (f), where outgoing flux eruptions lead to the formation of hot, shocked plasma close to the horizon. Although the plasma within flux eruption zones is highly magnetised ( $\sigma \gg 1$ ) and consequently excluded from our emission sampling (which requires  $\sigma < 1$ ), there remains a hot boundary layer between these zones and the denser surrounding accreting medium. Such boundary layers dominate the NIR and X-ray emission, as both the K-model and the  $R_{\leq 10, \leq 5}$  prescriptions preferentially sample the hot gas located there. As flux eruptions are both stronger for  $a_* = 0.94$  and more rapidly wind around the disc's spin axis compared to  $a_* = 0$ , they produce more sharply defined low- and high-density regions. This leads to well-defined spiral structures (Fig. 11(f)), which are apparent even in the sub-mm emission, where low-density regions contribute little to no emission. As the frequency increases, emission becomes increasingly confined to the inner edges of the spiral arm structures, bordering the highly magnetised plasma where  $\beta < 1$ . By increasing  $R_{high}$ , these confined spiral emission structures diffuse but remain noticeable. Past  $R_{\geq 40, 1}$ ,  $\Theta_e$  quickly plateaus, and most high-frequency emission vanishes.

Figs. 12 and 13 present a more detailed view of the corresponding fluid parameters by including the underlying proton temperatures and the local gas-to-magnetic pressure ratio,  $\beta$ , as a function of plasma density (expressed through the electron number density  $N_e$ , which scales one-to-one with the proton number density and thus plasma density). Moreover, we provide additional face-on emission maps where the colour scale corresponds to  $\beta$ . We then compare the  $R_{160,1}$  prescription (panel a) to the K-model (panel b) during the most luminous part of the K-models NIR and X-ray integrated light curves (§3.2). The time evolution of these figures helps identify two states in the disc: a ‘quiescent’ state where the proton population that underlines the emission zone remains subrelativistic ( $\Theta_p < 1$ ) and an ‘eruption’ state which contains an additional relativistic proton population in the plasma layers around the eruption zone. Fig. 12 and 13 help illustrate how high-frequency emission in the K-model tends to originate from the inner parts of the spiral structures where  $\beta \geq 1$  and  $\Theta_p \gtrsim 1$ . In contrast, for  $R_{160,1}$ , electron temperatures in these same regions are significantly lower as  $T_e \approx T_i/160$  for  $\beta \gg 1$ . As a result, emission from hot plasma is suppressed and instead predominantly originates from cooler zones where  $\beta < 1$  and  $\Theta_p < 1$ . Consequently,  $\Theta_e$  plateaus, except for a few highly relativistic regions ( $\Theta_p \gtrsim 10$ ) bordering inner eruption zones that can still contribute some emission. Among the additional  $R(\beta)$  prescriptions,  $R_{40,1}$  behaves similarly to  $R_{160,1}$ , though plateauing at a higher electron temperature of  $\Theta_e \approx 70$ . The  $R_{\leq 3, \leq 5}$  prescriptions more closely resemble the K-model,  $R_{10,1}$  shows intermediate behaviour between the two. All these trends are consistent throughout the simulation. The figures corresponding to the

remaining prescriptions are given in Fig. B1 in Appendix B<sup>8</sup>.

In Fig. 14 we compare the time-averaged total SED for each  $R(\beta)$  prescription (coloured thick lines) to that of the K-model (underlying thick grey lines). Shaded regions represent the minimum to maximum reached spectral luminosity. Unsurprisingly, the  $R_{\leq 3}, \leq 5$  prescriptions generally provide the best match for the K-model, although for  $a_* = 0.94$ ,  $R_{1,1}$  does significantly overpredict the K-model. This is consistent with our earlier findings on the electron temperature similarities as discussed in above. We note how this is only based on averaged spectra properties, such that individual NIR and X-ray fits can still differ between models. We conclude that  $R(\beta)$  prescriptions can serve as useful approximations to the more sophisticated turbulent K-model when studying high-energy, time-averaged observables. In the next section, we show that this is also the case when considering NIR and X-ray variability.

---

<sup>8</sup>In addition, movies for a range of  $R(\beta)$  prescriptions can be found at <https://www.youtube.com/playlist?list=PLujfkmFfo7WQksP3N7fBx06nuDQdyopkY>.

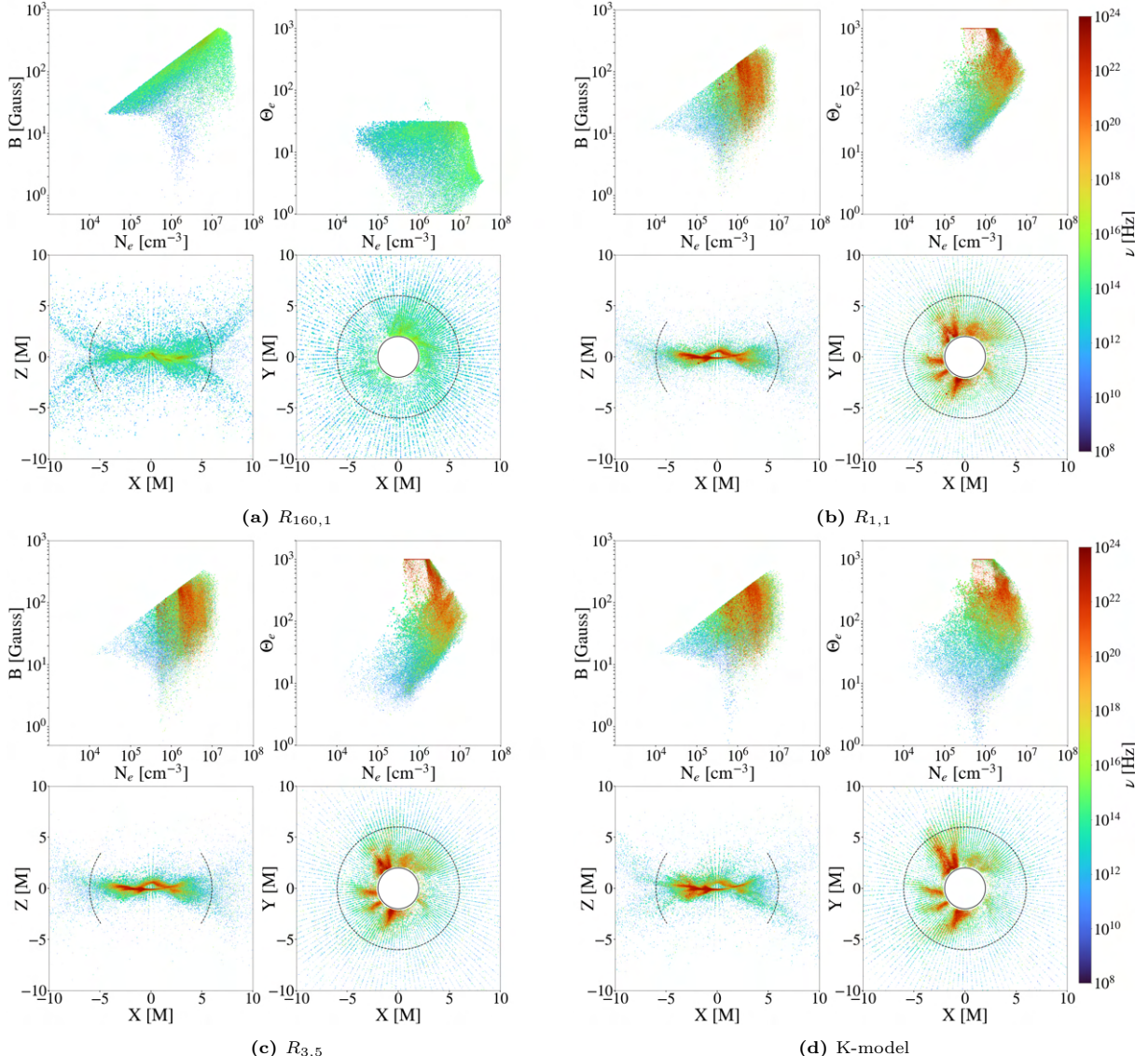


**Figure 9:** Superphoton origin within  $10 M$  and their associated local plasma properties constructed by ray-tracing an  $a_* = 0$  GRMHD snapshot at  $t = 23630 M$  for four electron temperature models. Each temperature model is divided into a  $2 \times 2$  subgrid with (a)  $R_{160,1}$ ; (b)  $R_{1,1}$ ; (c)  $R_{3,5}$  and (d) the K-model. Plotted in all  $2 \times 2$  subpanels are the magnetic field strength,  $B = \sqrt{b^\mu b_\mu}$ , and the dimensionless electron temperature,  $\Theta_e = kT_e/m_ec^2$ , as a function of electron number density ( $N_e$ ) and an edge-on and face-on view of the emission regions. Solid black lines represent the event horizon and dashed lines the ISCO. Dot sizes correspond to the product of the simulation weight with the photon frequency,  $w\nu$ , as this determines the photon's relative contribution to the SED. The corresponding  $\theta$ -averaged GRMHD fluid snapshots can be found in Fig. 11(e).

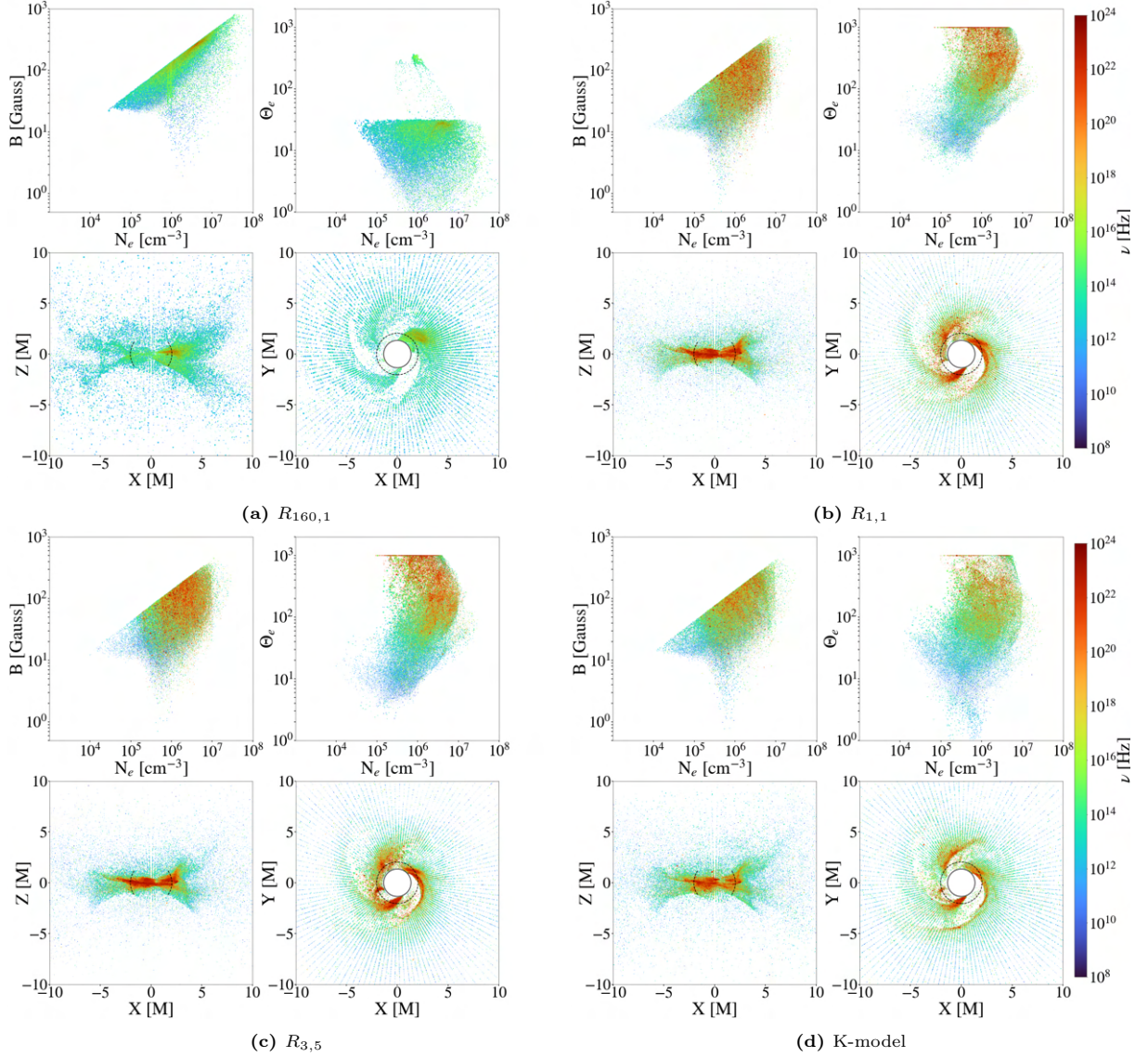


**Figure 10:** Same as in Fig. 9, but for  $a_* = 0.94$  at  $t = 20000 M$ . The corresponding  $\theta$ -averaged GRMHD fluid snapshots can be found in Fig. 11(f).

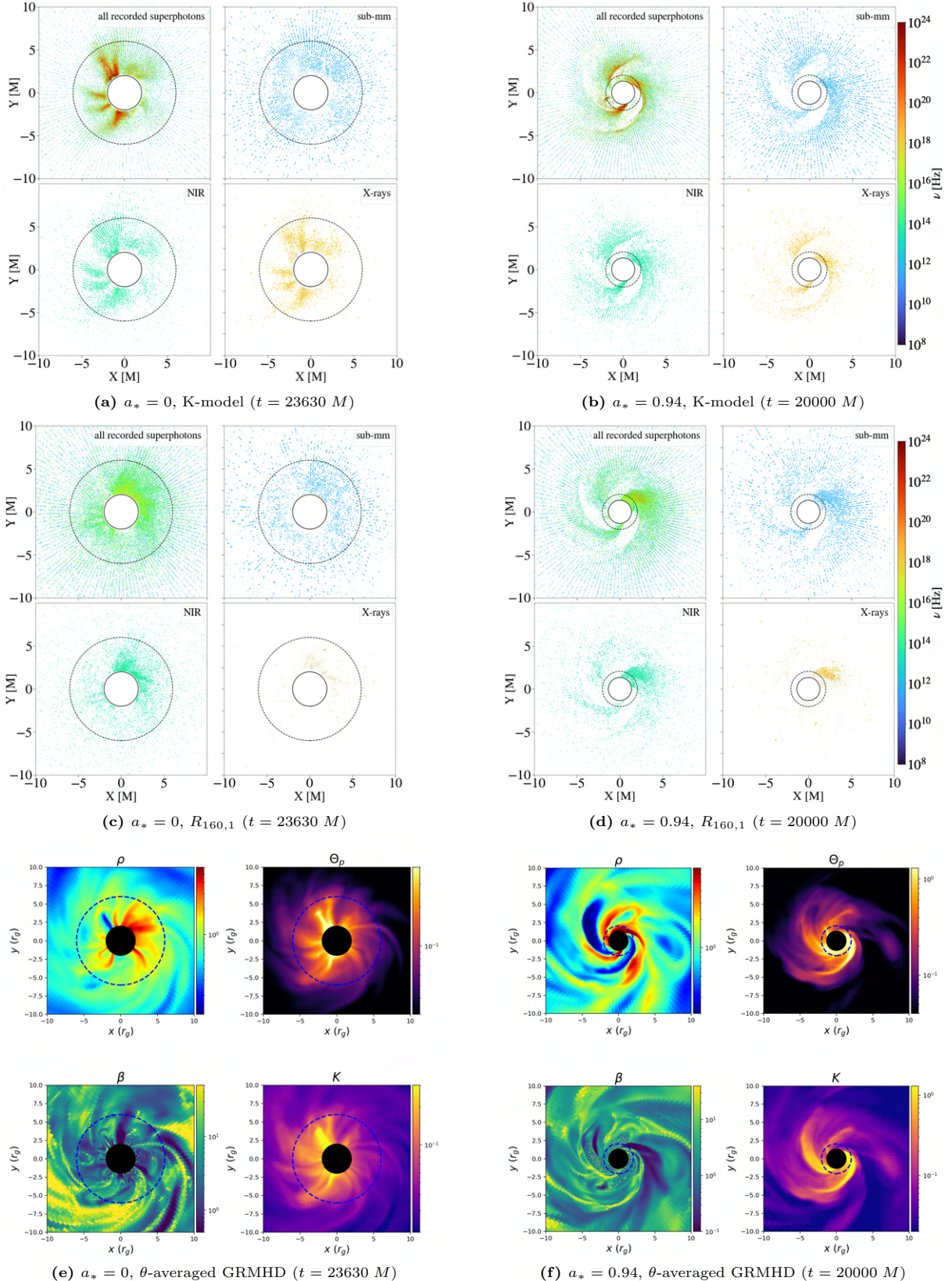


**Figure 11:** (a), (b), (c), (d): Face-on view of the K-model (a, b) and  $R_{160,1}$  (c, d) superphoton emission regions for  $a_* = 0$  (a, c) and  $a_* = 0.94$  (b, d). Both  $a_* = 0$  and  $a_* = 0.94$  time slices correspond to the most luminous part of the K-models light curve (see §3.2). Frequency ranges are limited to NIR (30-3  $\mu\text{m}$ , bottom left), sub-mm (300 GHz - 1 THz, top right) and X-rays (2-8 keV, bottom right). The solid and dashed lines correspond to the event horizon and ISCO, respectively. We do note that superphoton dot sizes have been adjusted per frequency range so that the individual superphoton size only corresponds to its respective SED contribution in the panels depicting ‘all recorded superphotons’, where we show the full frequency range of recorded superphotons. (e, f): underlying GRMHD density in code units  $\rho$  (top left), proton temperature  $\Theta_p$  (top right),  $\beta \equiv P_g/P_B$  (bottom left) and entropy  $K = (\gamma - 1) u \rho^{-\gamma}$  (bottom right). Note that the colour scaling differs between  $a_* = 0$  and  $a_* = 0.94$ .

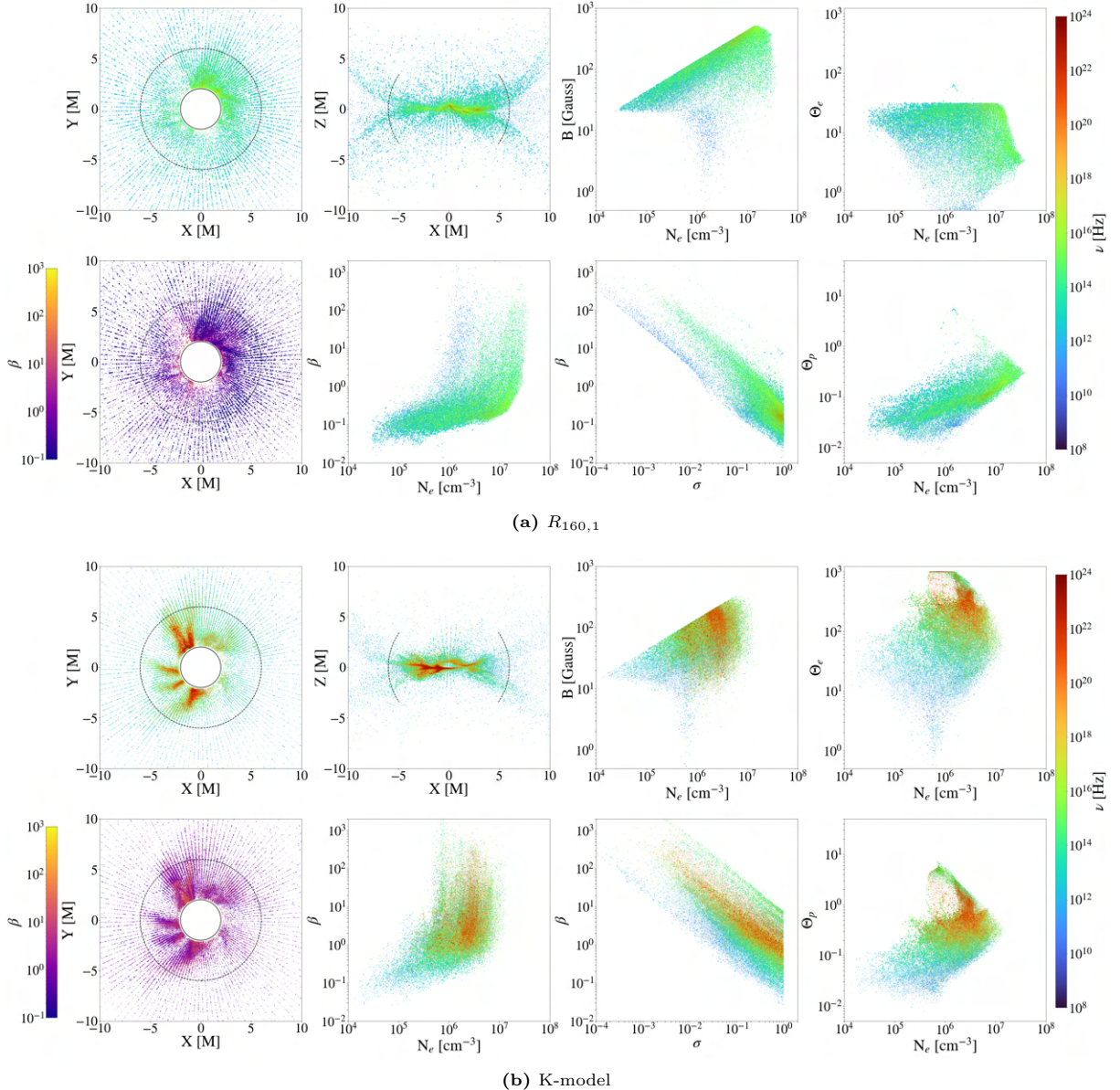


**Figure 12:** Same as in Fig. 9, but now including a more detailed plasma parameter overview for  $R_{160,1}$  (a) and the K-model (a), both for  $a_* = 0.0$  at  $t = 23630 M$ . The top row for both models contains the same panels as in Fig. 9. The bottom row depicts a face-on view of the plasma  $\beta$ ,  $\beta$  versus density ( $N_e$ ),  $\beta$  versus the magnetisation ( $\sigma$ ) and the dimensionless proton temperature  $\Theta_p$  versus  $N_e$ .

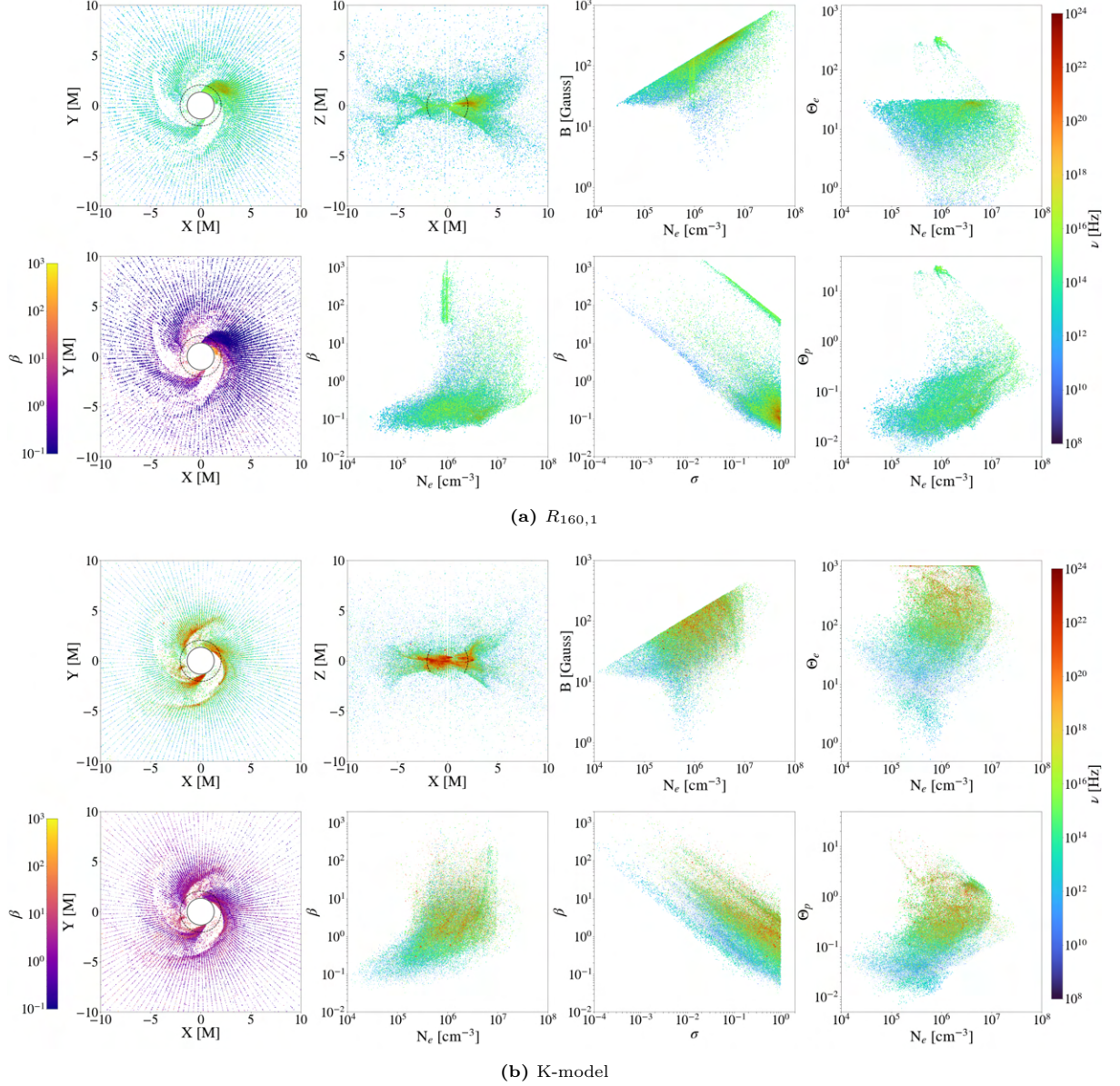


**Figure 13:** Same as in Fig. 12, but for  $a_* = 0.94$  ( $t = 20000 M$ ).

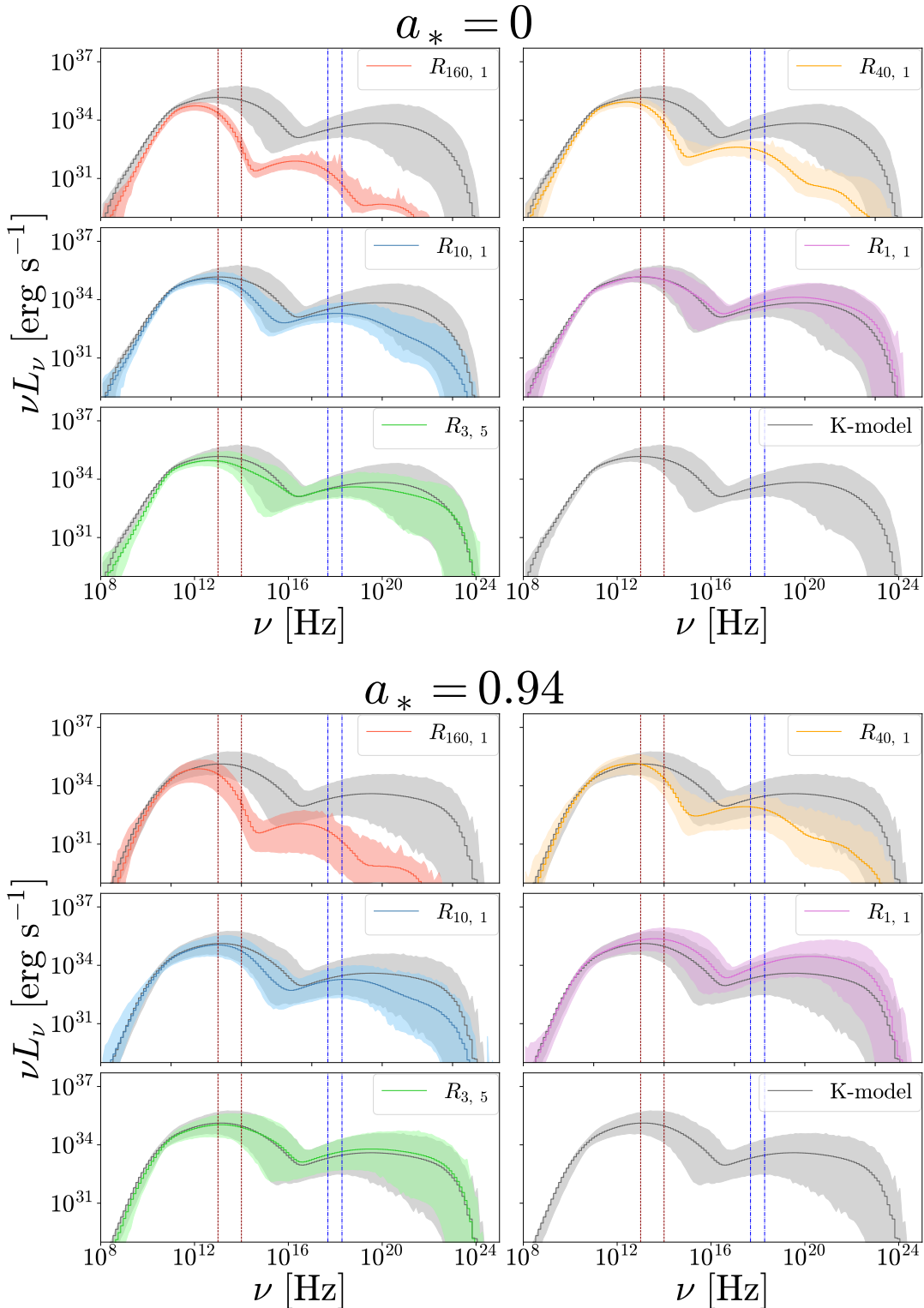


**Figure 14:** Comparison of  $R(\beta)$  prescriptions with the K-model. The red, orange, blue, purple and green lines represent the time-averaged SED of the  $(R_{high}, R_{low}) = (160, 1); (40, 1); (10, 1); (1, 1)$  and  $(3, 5)$  models, respectively, and grey lines the K-model in each subfigure. Coloured regions indicate the minimum to maximum reached at each frequency between all SEDs of a model. The vertical lines correspond to the frequency ranges analysed in §3.2, with red dashed lines the NIR (30-3  $\mu$ m) and blue dash-dotted lines X-rays (2-8 keV).

### 3.2 Multiwavelength light curve time variability

As discussed in §3.1 and illustrated in Figs. 7 and 8, our models exhibit clear time variability. Here we provide a detailed quantitative variability analysis and characterise its origins. We integrate all SEDs to retrieve temperature model-specific broadband light curves. We then calculate the fractional root mean square (RMS) variability, light curve luminosity ratios, autocorrelation, cross-correlation functions (CCFs) and power spectral densities (PSDs), which help link the variability back to the underlying plasma.

Broadband light curves are computed by integrating each snapshot's SED ( $L = \int \nu L_\nu d\ln \nu$ ) over specific frequency bands spanning 30 to 3  $\mu\text{m}$  for NIR and 2 to 8 keV for X-rays. The full simulation time interval of  $\Delta t = 5000 M$  corresponds to  $\sim 28$  hours when scaled to Sgr A\*. An overview of all computed light curves is given in Fig. 15. These light curves form the basis of our variability analysis, beginning with the total fractional RMS variability, defined as  $c_{RMS,x} = \sigma_x/\bar{x}$ , with  $\sigma_x$  the standard deviation and  $\bar{x}$  the mean. Table 2 presents an overview of the total NIR and X-ray fractional RMS for all our models.

**Table 2:**  
Total fractional RMS variability for the integrated light curves from Fig. 15.

K-model	NIR $a_* = 0$	X-rays $a_* = 0$	NIR $a_* = 0.94$	X-rays $a_* = 0.94$
K-model	0.48	0.41	0.85	0.61
$R_{3,5}$	0.48	0.44	0.71	0.56
$R_{1,1}$	0.39	0.34	0.63	0.49
$R_{10,1}$	0.44	0.34	0.74	0.59
$R_{40,1}$	0.40	0.30	0.82	0.62
$R_{160,1}$	0.44	0.30	1.02	0.73

**Notes:** Each row corresponds to a different electron temperature model. The left two columns correspond to  $a_* = 0$  and the right two columns to  $a_* = 0.94$ .

Our results show that, regardless of BH spin, the NIR RMS variability consistently exceeds that of the X-rays for each electron temperature model. Moreover, the RMS variability for both NIR and X-rays increases significantly from  $a_* = 0$  to  $a_* = 0.94$  across all temperature models. We find a clear trend of increasing RMS variability with increasing  $R_{high}$  for  $a_* = 0.94$ , whereas this is not generally seen for  $a_* = 0$ . We further note a general, spin-independent increase in both the  $R_{3,5}$  prescription and the K-model.

To further characterise the amplitude of this variability, we examine the luminosity ratios of all our models throughout the full light curve. Fig. 16 presents the maximum-to-minimum luminosity ratios ( $L_{max}/L_{min}$ ) throughout the full light curve (blue dots) and for any restricted time windows of  $\sim 8$  hours for NIR and  $\sim 2$  hours for X-rays (red dots). For  $a_* = 0$ , we observe no significant trend in  $L_{max}/L_{min}$  with increasing  $R_{high}$ , aside from a potential slight decrease in NIR and increase in X-rays. Maximum luminosity ratios typically hover around  $L_{max}/L_{min} \lesssim 4 - 11$  in NIR and  $L_{max}/L_{min} \lesssim 7 - 15$  in X-rays. In contrast, for  $a_* = 0.94$ , these ratios notably increase, particularly toward large  $R_{high}$ , with a  $R_{160,1}$  total light curve luminosity ratio of  $L_{max}/L_{min} \gtrsim 40$  in NIR and  $\gtrsim 200$  in X-rays. This is mimicked by the shorter timescale luminosity ratio of  $\sim 30$  in NIR and  $\sim 50$  in X-rays. In addition, we show the

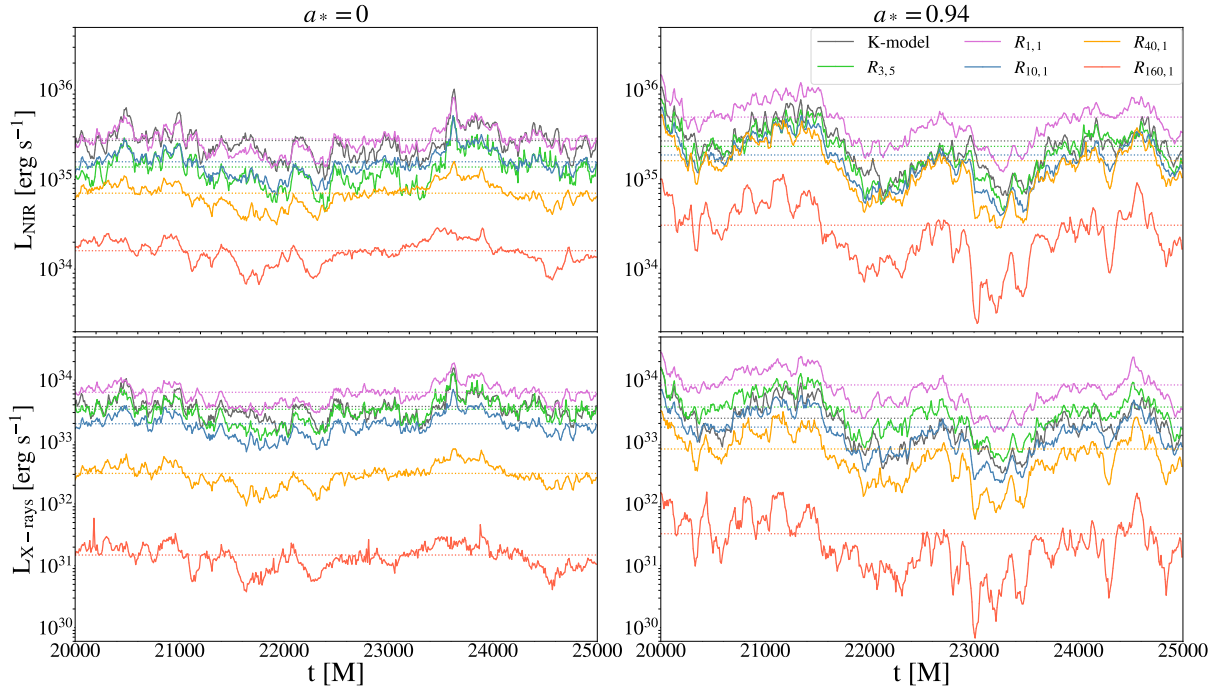


**Figure 15:** Left panels:  $a_* = 0$  integrated broadband light curves between  $t \in [20000, 25000]$   $M$  ( $\sim 28$  hours) for NIR (top, 30-3  $\mu\text{m}$ ) and X-rays (bottom, 2-8 keV). Dotted lines refer to each model's average luminosity. Right panels: Identical to the left panels, except now for  $a_* = 0.94$ . Grey; green; purple; blue; orange; and red correspond to the K-model;  $R_{3,5}$ ;  $R_{1,1}$ ;  $R_{10,1}$ ;  $R_{40,1}$ ;  $R_{160,1}$  prescription, respectively.

ratio of the average light curve luminosity with the minimum (green dots) and maximum (purple dots, inverted for scale) across the full light curve. Notably, in  $a_* = 0.94$  models,  $(L_{avg}/L_{max})^{-1}$  remains unchanged with increasing  $R_{high}$ , whereas  $L_{max}/L_{min}$  and  $L_{avg}/L_{min}$  increase rapidly. This indicated that the enhanced variability seen for  $R_{\geq 40, 1}$  is primarily the result of deep luminosity dips, rather than flaring activity.

Having quantified the variability amplitude we now investigate whether any periodic substructure is present in the signal. In Fig. 17, we compute PSDs of all modelled light curves together with that of the spin model-dependent mass accretion rate,  $\dot{M}$ , and the dimensionless magnetic flux on the horizon,  $\phi_{BH}$  (Tchekhovskoy et al., 2011), determined by

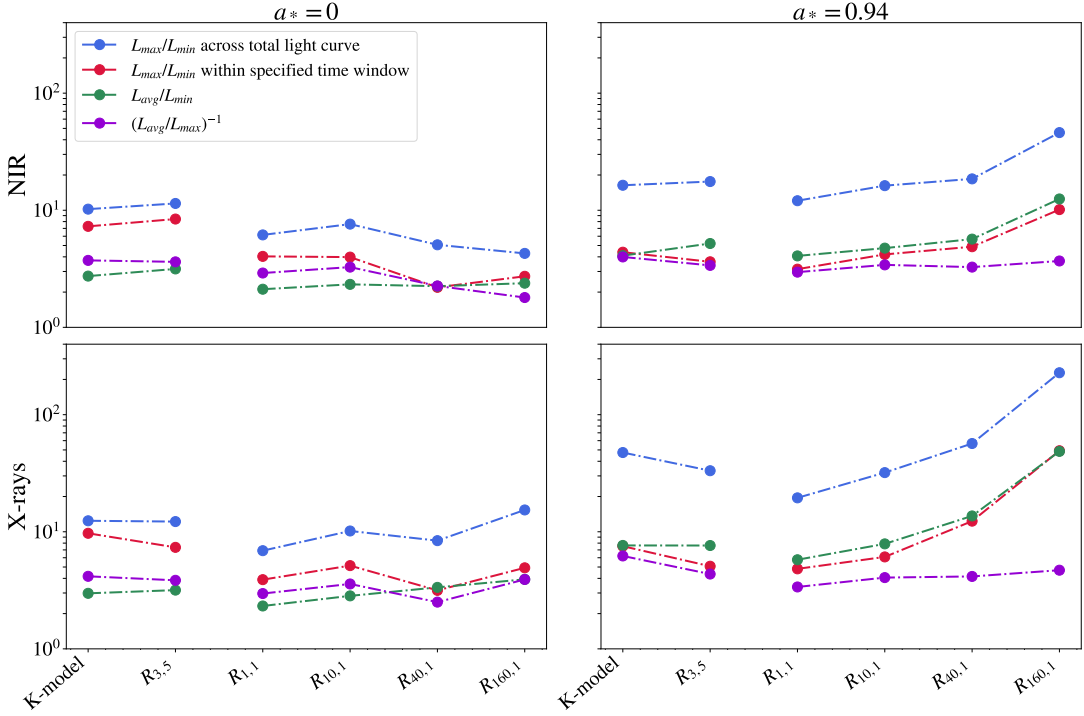
$$\dot{M} = - \int_{\phi} \int_{\theta} \rho u^r \sqrt{-g} d\theta d\phi, \quad (32)$$

and

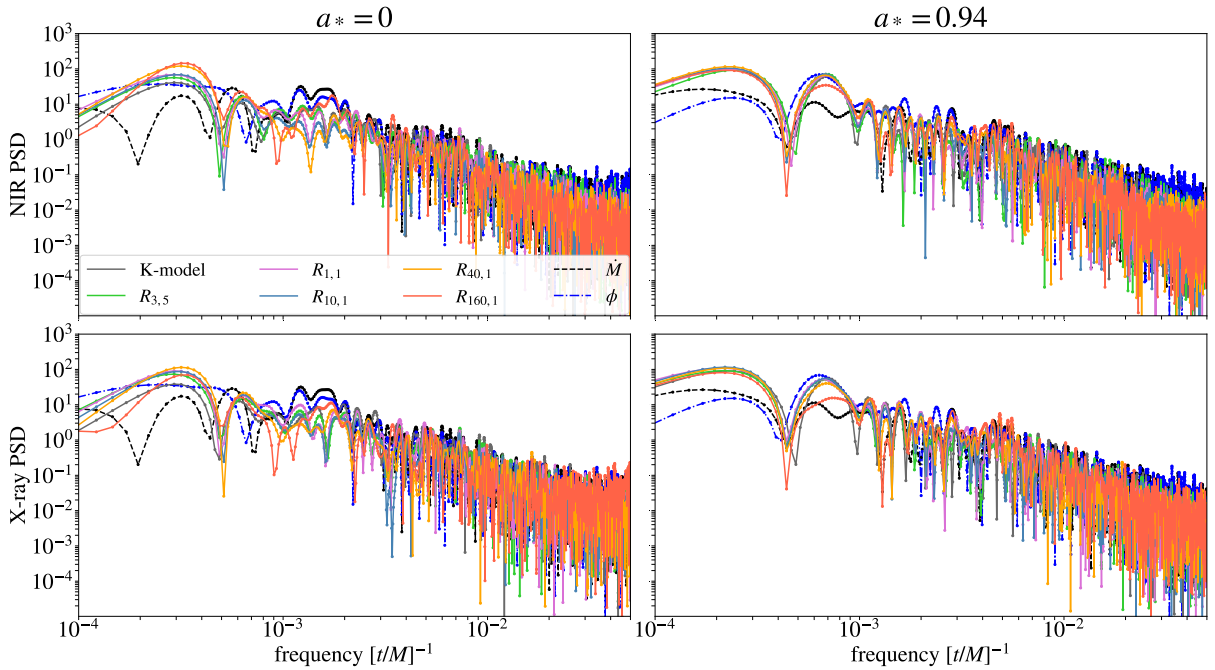
$$\phi_{BH} = \frac{\Phi_{BH}}{\sqrt{\langle \dot{M} \rangle}} = \frac{1}{\sqrt{\langle \dot{M} \rangle}} \int_{\phi} \int_{\theta} \|B^r\| \sqrt{-g} d\theta d\phi, \quad (33)$$

where  $u^r$  and  $B^r$  are the radial components of the fluid four-velocity and magnetic field, respectively, and  $\Phi_{BH}$  the magnetic flux. During the 5000  $M$  of the GRMHD simulations where we sample light curves, the MAD parameter,  $\phi_{BH}$ , ranges between  $30 \lesssim \phi_{BH} \lesssim 60$ . Regardless of BH spin and temperature model, both NIR and X-ray short-term ( $\lesssim 1000 M$  or 5 hours) variability<sup>9</sup> is best characterised by a stochastic red noise power spectrum, with no indication of periodic variability on near-horizon timescales. However, we do find spin model-dependent long-term periodicity, peaking at  $\sim 3000 M$  (17 hours) for  $a_* = 0$  and around  $\sim 1400$  and  $4300 M$  (8 and 22 hours) for  $a_* = 0.94$ . For  $a_* = 0.94$ , this long-term periodicity at  $\sim 1400 M$  is also clearly seen for  $\phi_{BH}$ .

<sup>9</sup>Given our sampling rate of  $10 M$ , the Nyquist limit sets the shortest resolvable period at  $20 M$ , or  $\sim 7$  minutes, which is within the observed short-term variability range.

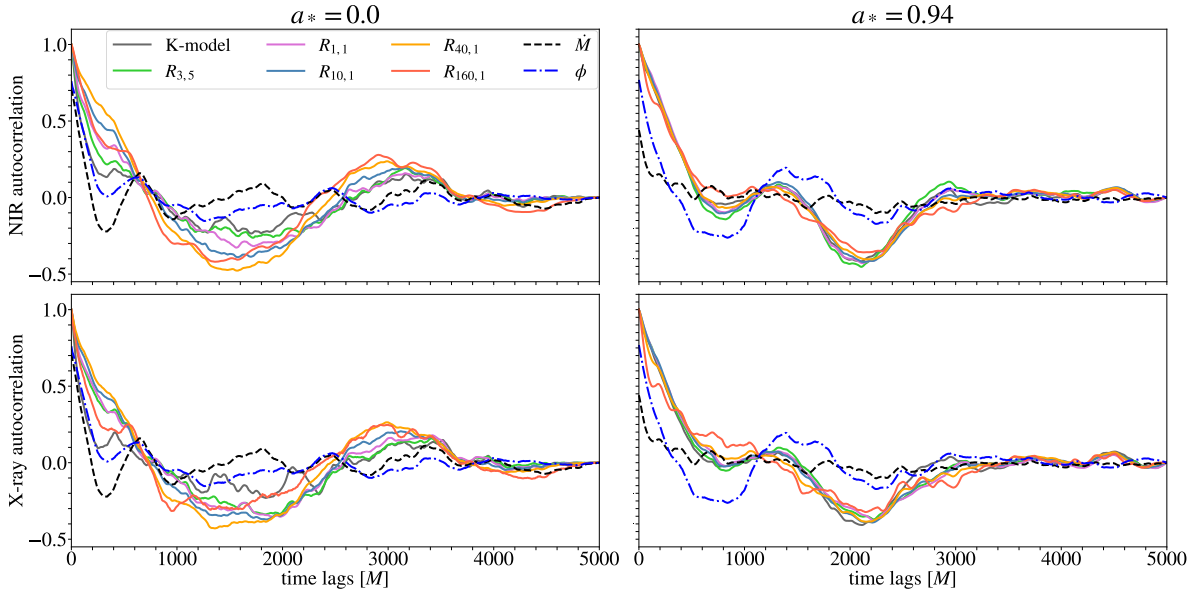


**Figure 16:** Left panels:  $a_* = 0$  light curve luminosity ratios for each electron temperature model. Blue points represent the ratio of maximum to minimum luminosity ( $L_{\max}/L_{\min}$ ) over the full light curve, while red points indicate the largest of this ratio within any restricted time window of  $1430 M$  ( $\sim 8$  hours) for NIR and  $360 M$  ( $\sim 2$  hours) for X-rays. Green points represent the ratio of average to minimum luminosity, while purple points indicate the inverse ratio of average to maximum luminosity. Right panels: Identical to the left panels, except now for  $a_* = 0.94$ .



**Figure 17:** Power spectral densities (PSDs) of all temperature model-specific light curves from Fig. 15 for both  $a_* = 0$  (left column) and  $a_* = 0.94$  (right column). Top row: NIR ( $30-3 \mu m$ ). Bottom row: X-rays ( $2-8$  keV). In addition, we plot the mass accretion rate,  $\dot{M}$ , as a black dashed line and the magnetic flux threading the event horizon,  $\phi_{BH}$ , as a blue dash-dotted line.

To look further into the underlying correlation of any periodic features, we compute autocorrelations in



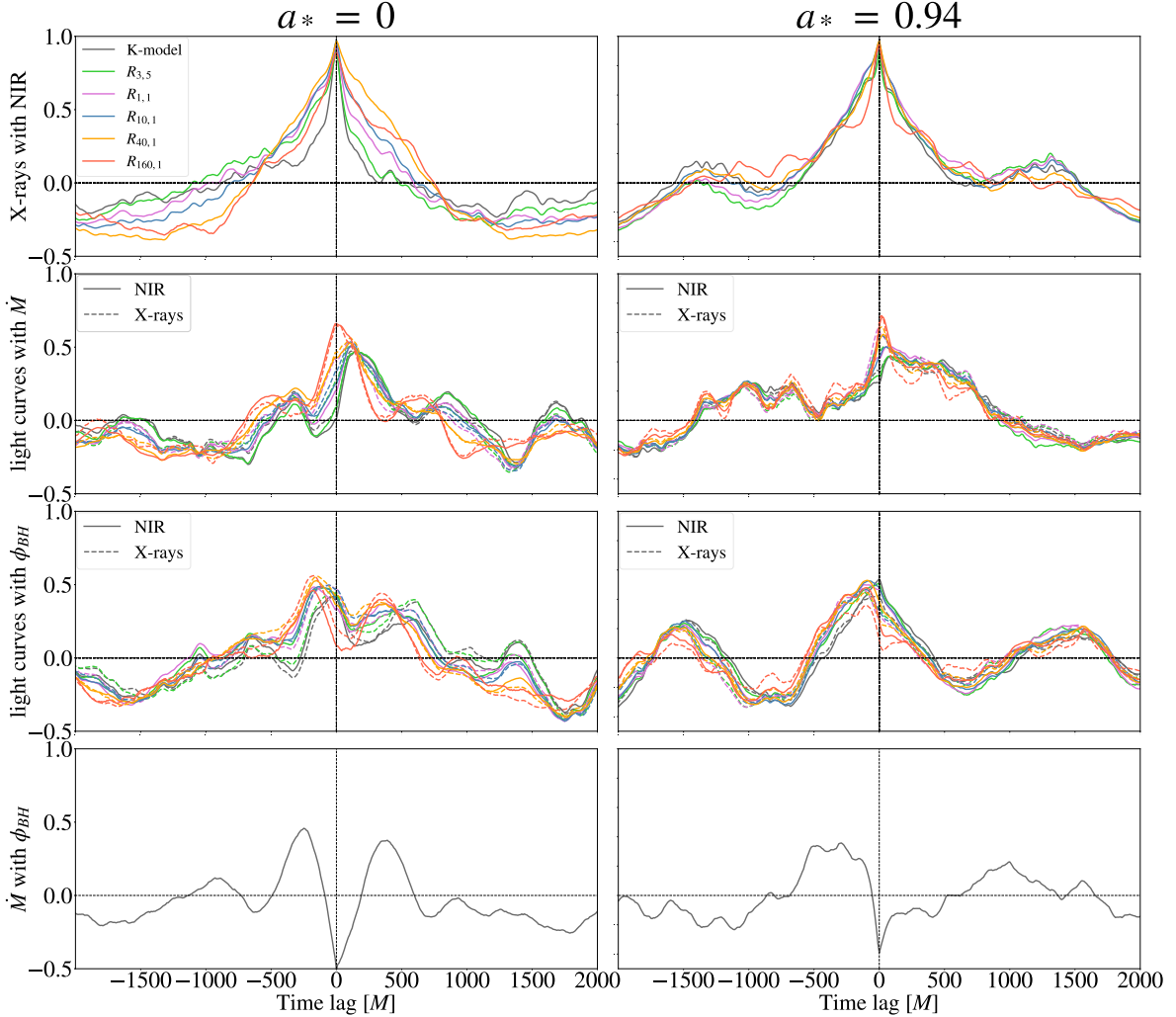
**Figure 18:** Normalised autocorrelations of all light curves from Fig. 15 for both  $a_* = 0$  (left column) and  $a_* = 0.94$  (right column). *Top row:* NIR (30–3  $\mu\text{m}$ ). *Bottom row:* X-rays (2–8 keV). Similar to Fig. 17, we plot the  $\dot{M}$  as a black dashed line and  $\phi_{BH}$  as a blue dash-dotted line.

Fig. 18 for all the same quantities present in the PSDs. For  $a_* = 0$ , all light curves exhibit a clear single periodic signal, consistent with the long-term periodicity seen in the PSDs. For  $a_* = 0.94$ , however, two separate periodic signals overlap, with the shorter period of  $\sim 1400 M$  appearing also in  $\phi_{BH}$ , whereas  $\dot{M}$  shows no significant coherent or periodic variability. For  $a_* = 0$ , both  $\phi_{BH}$  and  $\dot{M}$  show a notable periodic signal with a period of  $\sim 650 M$  (3.5 hours), without clear signs of longer periodicity. All these results are consistent with Fig. 17. We conclude that long-term oscillatory components are present in our light curves, such that part of the maximum-to-minimum luminosity ratios in Fig. 16 can be attributed to this long-term variability.

As initially demonstrated in Fig. 11(a)-(d), both our NIR and X-ray emission originates from similar regions. Moreover, their light curves closely align (Fig. 15). To quantitatively assess whether the Comptonization into X-rays is indeed temporally correlated with the NIR synchrotron emission, we compute CCFs between all temperature model-specific X-ray and NIR light curves in the top row of Fig. 19. These consistently show strong correlation centred around zero time lag ( $\tau = 0$ ), confirming that X-rays and NIR are simultaneous and that X-ray emission in our models is indeed co-located SSC emission. We link the relatively slow drop-off with increasing or decreasing time lag to the long-term periodic components, apparent in all light curves (Fig. 17). For  $a_* = 0$ , correlation toward positive lags is slightly skewed with respect to negative lags for the hottest  $R_{\leq 3, \leq 5}$  prescriptions, suggesting that NIR variability is somewhat of a stronger predictor of future X-ray variability than vice versa. For  $a_* = 0.94$ , we see no such trend.

We extend our CCF analysis by cross-correlating each NIR and X-ray light curve with the mass accretion rate,  $\dot{M}$  (second row in Fig. 19), the magnetic flux on the event horizon,  $\phi_{BH}$  (third row), and  $\dot{M}$  with  $\phi_{BH}$  (bottom row). We explicitly focus on longer timescales to link back to the long-term periodicity from the PSD and autocorrelation analysis. We note that  $\phi_{BH}$  (also often referred to as the ‘MAD parameter’) gradually builds up on the BH, until  $\phi_{BH}$  eventually saturates at  $\phi \approx 50 – 60$  in our simulations. As the magnetic pressure increases, the accretion flow is choked off. During flux eruptions,  $\phi_{BH}$  drops rapidly, and accretion onto the BH is resumed. A clear (anti-)correlation with  $\phi_{BH}$  can thus indicate a connection to the eruption zones. This is indeed demonstrated in the  $a_* = 0$  CCF between  $\dot{M}$  and  $\phi_{BH}$  (bottom panel), which shows a pattern of moderate negative and positive correlation, consis-

tent with anti-correlated periodic variability peaked around  $\tau = 0$ , and with a period of  $\sim 600 - 700 M$ . This agrees with our previous findings in the left panels of Figs. 17 and 18. For  $a_* = 0.94$  we lack clear indication that changes in  $\phi_{BH}$  lead those in  $\dot{M}$ , but do find notable anti-correlation at  $\tau = 0$  and signs that  $\dot{M}$  leads  $\phi_{BH}$  by about  $\sim 100 - 500 M$ . Cross-correlating the light curves with  $\dot{M}$  reveals



**Figure 19:** Cross correlation functions (CCFs) between all the same quantities presented in Figs. 17 and 18. The left column corresponds to  $a_* = 0$  and the right to  $a_* = 0.94$ . *Top row:* Between each temperature model-specific X-ray and NIR light curve. *Second row:* Between each NIR/X-ray light curve and  $\dot{M}$ . *Third row:* Between each NIR/X-ray light curve and  $\phi_{BH}$ . In both the second and third rows, solid lines correspond to NIR and dashed lines to X-rays. *Bottom row:* Between the spin model-dependent  $\dot{M}$  and  $\phi_{BH}$ .

moderate peak correlations ranging from  $\sim 0.5 - 0.65$  for  $a_* = 0$  and up to  $\sim 0.7$  for  $a_* = 0.94$ . Peak light curve- $\phi_{BH}$  correlations are  $\sim 0.5$ , regardless of BH spin. Both the  $a_* = 0$  and  $a_* = 0.94$  light curve- $\dot{M}$  CCF functions peak near short positive time lags, with the  $R_{160,1}$  prescription almost precisely at  $\tau = 0$ . In general, the  $R_{160,1}$  prescription correlates strongest to  $\dot{M}$  at  $\tau = 0$  and hotter temperature prescriptions are shifted toward larger time lags of at most  $200 M$  for  $a_* = 0$  and  $100 M$  for  $a_* = 0.94$ . Between spin models, the structure of the light curve- $\phi_{BH}$  CCF functions changes drastically. For  $a_* = 0$  we find a general trend where longer light curve- $\phi_{BH}$  time lags corresponds to a shorter light curve- $\dot{M}$  lags and vice versa. This only holds within a time lag window of about  $\pm 500$  around  $\tau = 0$  where  $\dot{M}$  and  $\phi_{BH}$  are most (anti-)correlated. For  $a_* = 0.94$  the light curve- $\phi_{BH}$  correlation shows correlated periodic variability with a period of  $\sim 1400 M$ , consistent with the periodic signal in both  $\phi_{BH}$  and the light curves found in Fig. 17. The longest periodicity of  $\sim 3000 M$  for  $a_* = 0$  light curves is not immediately evident from Fig. 19, but does emerge moderately from the light curve- $\dot{M}$  CCFs by extending the axis to longer time lags. The signal at  $4300 M$  for  $a_* = 0.94$ , however, remains weak in the CCF.

In summary, variability in both the mass accretion rate and magnetic flux on the BH horizon correlates moderately with light curve variability for both BH spins. For  $a_* = 0$ ,  $\dot{M}$  and  $\phi_{BH}$  exhibit variability on timescales of  $\sim 650 M$ , their moderate correlation with the light curves suggests this periodicity does not strongly or consistently imprint on the light curve periodicity. Only for  $a_* = 0.94$  does the periodic variability in  $\phi_{BH}$  clearly imprint on the light curves at a period of  $\sim 1400 M$ , suggesting it plays a dominant role in driving the observed periodic behaviour. On timescales below  $500 M$  ( $\sim 3$  hours), only stochastic variability drives all variables considered here.

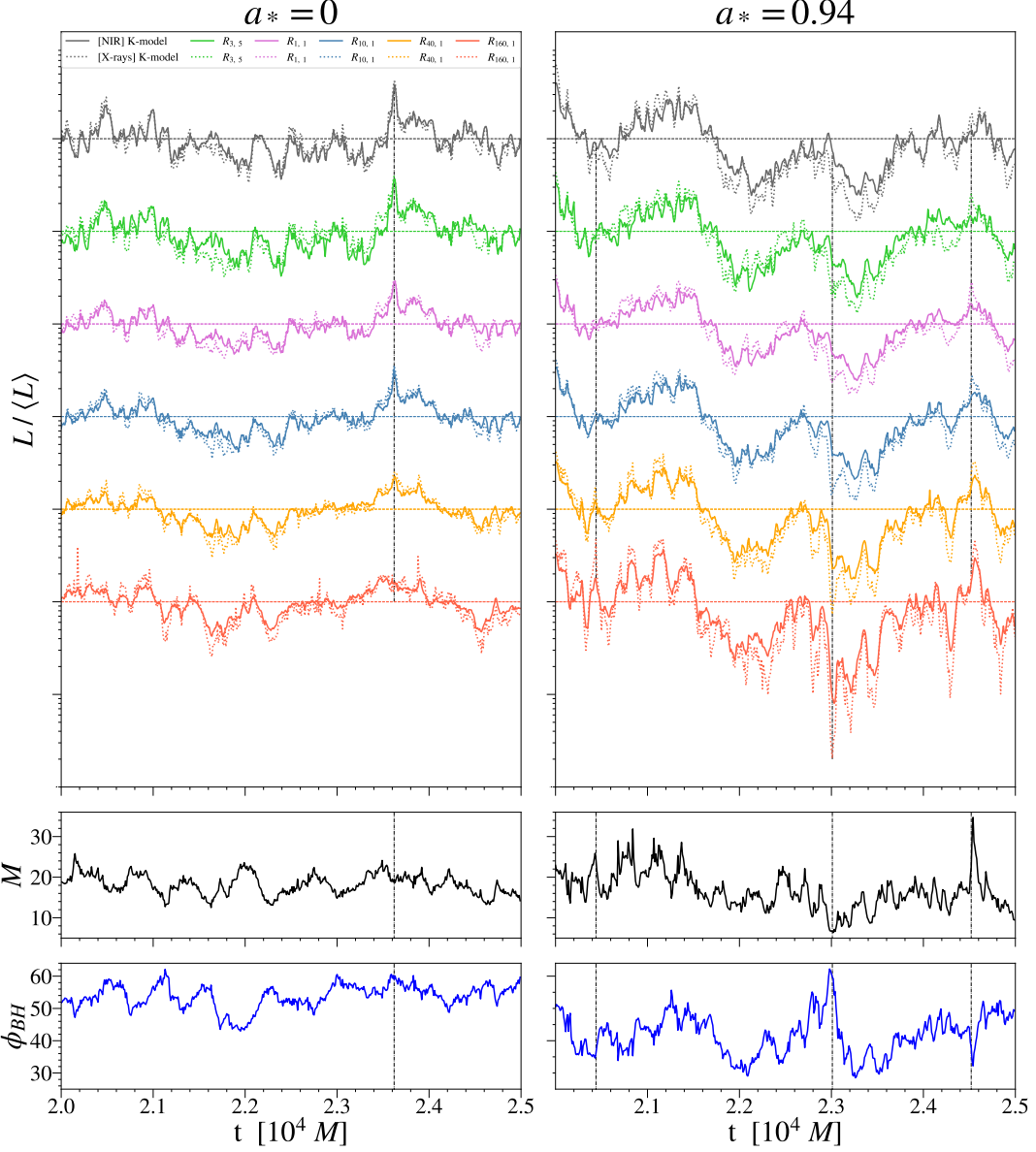


**Figure 20:** Top row: The light curves from Fig. 15 normalised by their average luminosity over the entire interval. Models are separated by a decade along the y-axis. Temperature model-dependent NIR (solid lines) and X-ray (dotted lines) luminosity evolution curves are overlaid on the same axis. Middle row: The evolution of the mass accretion rate,  $\dot{M}$ , in code units (Eq. 32). Bottom row: The evolution of the dimensionless magnetic flux on the BH horizon,  $\phi_{BH}$  (Eq. 33). In all panels, vertical dash-dotted lines highlight strong differences between the model-dependent luminosities and the corresponding  $\dot{M}$  and  $\phi_{BH}$ . Left panels represent  $a_* = 0$  and right panels  $a_* = 0.94$ .

In Fig. 20, we compare light curve variability across temperature models by normalising each curve by its average luminosity and overlaying the NIR and X-rays signals. In the bottom panels, we provide the evolution of the mass accretion rate and magnetic flux on the horizon, which indeed appear most notably

anti-correlated at  $\tau = 0$  for  $a_* = 0$ . Across spin models, both NIR and X-ray luminosities follow highly similar variability patterns, indeed without time delay.

For both the  $a_* = 0$  K-model and  $R_{\leq 10, \leq 5}$  prescriptions, a prominent ‘spike’ occurs at  $t = 23630 M$ , as indicated by the vertical dash-dotted black line in the left panel. At this moment in the evolution, luminosities increase by a factor of four, marking it as a good candidate for flares observed in Sgr A\* as discussed in §1.3. The underlying photon maps (Fig. 12) and GRMHD panels (Fig. 11e) show that the associated emission stems from compact regions within  $r \lesssim 5 M$  where outward-propagating flux eruptions shock the inflowing gas. These shocked boundary layers host an abundance of (trans-)relativistic protons, which translate to a hot electron population as discussed in §3.1. Such variable ‘eruption layers’ typically last for  $\sim 30 - 150 M$  (10 – 50 minutes) and are present throughout most of the disc’s evolution. However, stronger flux eruptions (i.e. steep drops in  $\phi_{BH}$ ) do not necessarily correlate to the largest increases in luminosity, as large parts of the disc are rapidly expelled and the eruption zone becomes masked as  $\sigma > \sigma_{max} = 1$ . Rather, the spike at  $t = 23630 M$  reflects the effect of multiple smaller stochastically accumulating flux eruptions. Toward larger  $R_{high}$ , spikes in the light curve are increasingly suppressed as electron temperatures become too low to effectively couple to the eruption layers in the disc.

Compared to  $a_* = 0$ , flux eruptions for  $a_* = 0.94$  are not only stronger but also rapidly get ‘wrapped’ around the disc’s spin axis. Similarly to the  $a_* = 0$  case, the peak luminosity of the K-model and  $R_{\leq 10, \leq 5}$  prescriptions at  $t = 20000 M$  can be linked back to a combination of multiple separated smaller flux eruptions (Figs. 13 and 11f). All  $a_* = 0.94$  light curves exhibit a long-term oscillatory component, matching the  $\sim 1400 - 1500 M$  periodicity in  $\phi_{BH}$  and contributing to the general increase in RMS variability found in Table 2. Toward cooler  $R(\beta)$  prescriptions, emission naturally stems from less energetic material that is more sensitive to changes in the magnetic pressure on the horizon. As  $\phi_{BH}$  increases and accretion is suppressed,  $\dot{M}$  drops sharply, leading to a steep decline in luminosity, most notably for  $R_{160,1}$ . When accretion is resumed following a flux eruption event, the luminosity spikes up again. The result is a highly variable pattern of sharp luminosity drops during low  $\dot{M}$  and spikes during high  $\dot{M}$ , as highlighted by vertical black dashed lines in the right panels of Fig. 20. Toward hotter temperature models, isolated dips in luminosity are more strongly linked to the onset of the flux eruptions themselves, where large portions of energetic plasma are expelled from the disk. In Fig. B2 in Appendix B we demonstrate the disruptive nature of the largest flux eruption in our  $a_* = 0.94$  model on the emission at  $t = 23010 M$ .

### 3.3 Comparison to observations

We here compare the spectral predictions of our electron temperature models against observational constraints. In Fig. 21, we show the models’ averaged SEDs and variability ranges alongside observational quiescent constraints (EHT Collaboration, 2022d, black dots). Moreover, we compare against a range of X-ray flaring events that were simultaneous with a NIR peak or reported to be ‘within 10 minutes of each other’ (Eckart et al., 2012, their Table 3). Such simultaneous observations are typically explained as SSC emission (Markoff et al., 2001; Eckart et al., 2004, 2006, 2008), which is the regime that we model in this work. We further note that observational studies find approximately four times the amount of NIR flares compared to X-rays (Neilsen et al., 2013), a discrepancy that may be attributed to a detection threshold potentially obscuring weak X-ray flares within the quiescent emission. Given the strong similarity and close correlation between the NIR and X-ray light curve peaks, we find no evidence in our models for such a discrepancy between frequency bands. In general, observed X-ray flares of Sagittarius A\* extend to a larger luminosity range compared to NIR. We overlay a range of 2-10 keV flares observed during a 3 Ms *Chandra* campaign, containing 39 isolated X-ray flares (Neilsen et al., 2013). These more or less correspond to the general range of highly luminous X-ray flares.

For both BH spin models, the K-model and  $R_{\leq 10, \leq 5}$  prescriptions generally overheat the electrons, overproducing the quiescent NIR and X-rays constraints, while still unable to explain the most energetic X-ray flares. This excess quiescent emission severely limits the achievable variability. While observations show that typical X-ray flares increase the luminosity by a factor of 10-30 compared quiescence (and can exceed ratios of  $\sim 500$  for the brightest flares, Witzel et al. 2018), our hot temperature models produce a smaller contrasts of at most 6 times the averaged luminosity for the  $a_* = 0.94$  K-model. In the NIR, observed flares are more moderate, typically reaching 3-10 times quiescence level, with exceptionally strong flares up to  $\sim 30$  times quiescence (Witzel et al., 2018). Our models reach NIR maximum-to-average luminosity ratios of at most 4. Only the  $a_* = 0.94 R_{40,1}$  prescription lies right on the edge of satisfying quiescent constraints while still being capable of reproducing some simultaneous flare luminosities. In general, all  $R_{\geq 40, 1}$  prescriptions are consistent with quiescent constraints, but remain unable to reproduce observed flare luminosities.

To best capture observed luminosities and variability, our comparisons suggest that a temperature prescription that behaves most like the cool  $R_{40,1}$  during quiescence and couples strongly to the eruption layers in the inner parts of the flow like  $R_{\leq 10, \leq 5}$  would help better match highly energetic flare-like observations for MAD models. MADs with a single  $R(\beta)$  prescription cannot naturally produce NIR and X-ray flares, despite being too variable at millimetre wavelengths (EHT Collaboration, 2022d).

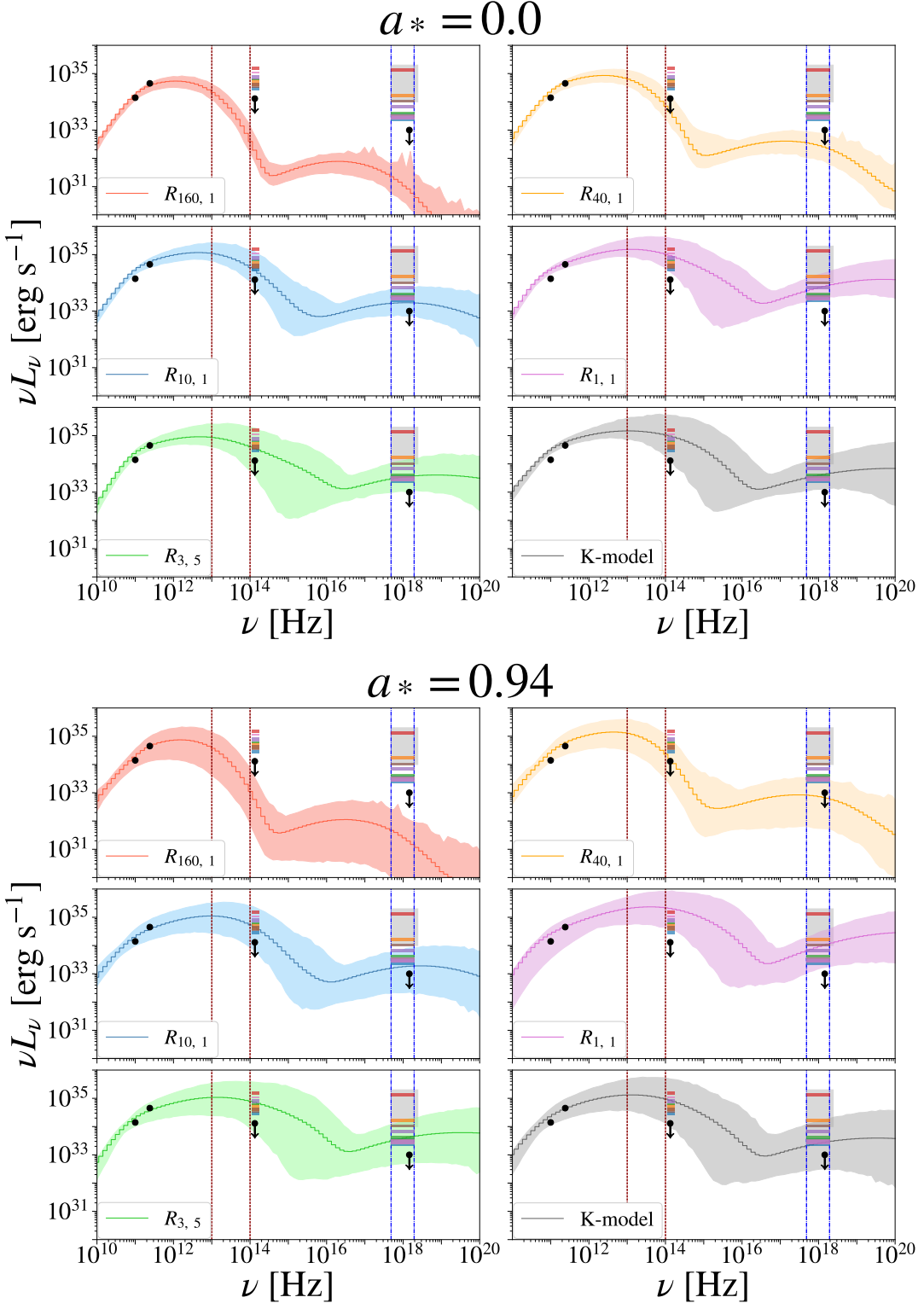


**Figure 21:** Similar to in Fig. 14, but instead we compare each model to observational quiescent data (black dots) during the EHT 2017 observing campaign, which provides upper limits to the models in NIR and X-rays (EHT Collaboration, 2022d). The coloured rectangles centred around  $2.2 \mu\text{m}$  and 4 keV represent observed X-ray flares that were associated with a simultaneous NIR peak to within 10 minutes (Eckart et al., 2012, see their Table 3). They note that the purple and red  $2.2 \mu\text{m}$  NIR peaks were extrapolated from the actual flux at  $3.5 \mu\text{m}$ ). Each colour denotes a distinct simultaneous event and its error margin within one  $\sigma$ . The shaded rectangular grey regions between 2 and 10 keV represent a range of 39 isolated X-ray flares from Neilsen et al. (2013) and more or less correspond to the general range of highly luminous X-ray flares.

In this work, we have employed radiative transfer to investigate the spectral properties and time variability of both NIR and X-ray emission produced by two-temperature MADs, applied to Sgr A\*. Through direct mapping of the emission regions, we have compared turbulent heating to a wide range of  $R(\beta)$  prescriptions and linked their respective emission back to the relevant underlying fluid properties.

### **4.1 Turbulent heating and $R(\beta)$ prescriptions in MADs**

We find that  $R_{\leq 10, \leq 5}$  prescriptions are well capable of reproducing the spectral luminosity range and averaged observables produced by the K-model. Moreover, they exhibit similar temporal variability and light curve profiles. Among these, the  $R_{3,5}$  model emerges as the closest match to the turbulent K-model, both in terms of emission morphology and variability. Although no single  $R(\beta)$  prescription universally reproduces the K-model across all metrics and spin values, our results highlight the utility of phenomenological  $R(\beta)$  prescriptions in approximating the more complex nature of thermal turbulent heating models for MADs. However, the K-model and similar  $R(\beta)$  prescriptions consistently overproduce both NIR and X-ray quiescent constraints obtained from observation ([Baganoff et al., 2003](#); [EHT Collaboration, 2022d](#)). This may indicate that turbulent Alfvénic heating is not an efficient heating mechanism in the environment of Sgr A\* or that the system is not as much in a MAD state as currently thought.

### **4.2 Emission zones characteristics and light curve variability**

The temperature model-specific NIR and X-ray emission in our models is tightly temporally correlated, independent of BH spin. We thus do not observe any time lags between the two bands as X-ray Comptonization in our models occurs by the same electron population that is sourcing NIR synchrotron photons, all within a dominant emission radius of  $\sim 5 M$ . We do note that many observational studies on weaker X-ray flaring events report low photon counts (e.g. [Boyce et al. 2019](#)), leaving large uncertainties to the interpretation of the spectral properties, such as their spectral index or total luminosity. We therefore do not consider a detailed spectral slope analysis of our models, but note it as a potential future direction of study.

Across all models, variability is stochastic to within  $\sim 5$  hours. Both the K-model and  $R_{\leq 10, \leq 5}$  prescriptions show emission peaks that originate from hot, shocked plasma in the boundaries layers between magnetically dominated ( $\beta \lesssim 1$ ) plasma created by outward propagating magnetic flux eruptions and gas-pressure dominated regions ( $\beta \gtrsim 1$ ). These regions are capable of driving light curve fluctuations on timescales of  $\sim 10\text{-}50$  minutes. For  $a_* = 0$  models, such zones more or less appear as co-rotating localised hot spots, whereas for  $a_* = 0.94$  they are stretched out into spiral structures.

The RMS light curve variability increases with BH spin, even more significantly toward cooler temperature prescriptions. We link this to a long-term ( $\sim 8$  hours) oscillatory component in the light curves and an increased correlation with the mass accretion rate toward cooler temperature models. Across all models, the NIR and X-ray maximum-to-average luminosity ratios remain below  $\lesssim 4$  for NIR and below 6 for X-rays, which stays well below some of the strongest observed X-ray flaring-to-quiescent flux ratios ([Eckart et al., 2012](#)). Thus, despite being too variable at 230 GHz ([EHT Collaboration, 2022d](#)), both turbulent heating and  $R(\beta)$  prescriptions remain unable to explain the observed variability toward higher frequencies naturally. Such flares may be best recovered by including a non-thermal component in future models.

### 4.3 The role of magnetic reconnection heating

In this work, we only model electron heating alongside the flow in the GRMHD simulation through the turbulent K-model. However, the flux eruption layers that we associate with highly energetic emission are potential sites for both thermal and nonthermal magnetic reconnection heating. The energetics of such (non)thermal electron populations remains one of the least constrained aspects of current models. As we are unable to capture the strongest observed flare amplitudes, (non)thermal reconnection heating may represent a crucial missing ingredient in current emission models. It is plausible that some superposition of electron heating mechanisms could naturally reproduce the more extended and steady emission that results from  $R_{\geq 40, 1}$  prescriptions, while simultaneously being able to produce intense localised heating associated with flux eruptions, which should occur on timescales in line with flare observations.

Reconnection heating has been partly explored in the context of radiative models of Sgr A\*. Chael et al. (2018) apply a sub-grid heating prescription based on the trans-relativistic thermal reconnection heating model from Rowan et al. (2017) to SANE discs. They find that both turbulent and reconnection heating underpredict NIR and X-ray variability. Dexter et al. (2020b) apply the nonthermal reconnection heating model from Werner et al. (2018) to MADs, but they inject the dissipated heat into a thermal electron population. They include polarisation in their analysis, but omit X-ray emission and a detailed variability analysis. Their  $a_* = 0.9375$  MAD model shows similar spiral emission structures and similar heating in the boundary regions between the strongly magnetised ( $\beta \lesssim 1$ ) and weakly magnetised ( $\beta \gtrsim 1$ ) plasma. Although their NIR spectral luminosities agree reasonably well with our models, their model produces stronger NIR ‘flare-like’ variability, with the flux increasing by an order of  $\sim 10 - 20$  on timescales of  $\sim 30 - 60$  min. This may indeed suggest that reconnection heating is the more dominant mechanism driving flaring behaviour in Sgr A\*. We do note that X-rays in our models originate from these same emission regions and do not exhibit a notable increase in variability compared to the NIR. Thus, by extension, thermal reconnection heating models may also fail at explaining the large difference in observed NIR and X-ray flare variability, such that a nonthermal, dominantly X-ray emitting electron population remains a likely candidate.

The thermal reconnection model from Rowan et al. (2017) distributes dissipated heat according to

$$\delta_e = \frac{1}{2} \exp \left( \frac{-(1 - \beta/\beta_{max})^{3.3}}{1 + 1.2 \sigma_w^{0.7}} \right), \quad (34)$$

where  $\beta \leq \beta_{max} = \sigma_w/4$  and  $\sigma_w$  the local ratio of magnetic energy to enthalpy density (which is the magnetisation accounted for relativistic inertia)

$$\sigma_w = \frac{b^2}{w} = \frac{b^2}{(\rho_e + \rho_p)c^2 + \gamma_e u_e + \gamma_p u_p}, \quad (35)$$

with  $\rho_e, \rho_p$  the electron and proton densities,  $\gamma_e$  and  $\gamma_p$  the adiabatic indices and  $u_e, u_p$  the internal energy densities, respectively. As reconnection heating models remain derived from particle-in-cell simulations, their application to global GRMHD simulations is somewhat difficult to justify and leaves plenty of uncertainties. Given the lack of consensus on the importance of different heating mechanisms, we explore an alternative ad-hoc motivated electron temperature prescription that, like reconnection-based models, includes a magnetisation parameter. Its main purpose is to attempt to decouple the quiescent electron population from the highly energetic eruption layers, such that the system remains below quiescent constraints while still able to couple to highly energetic flux eruption layers. In Appendix C, we describe this prospective  $R(\beta, \sigma)$  prescription, which introduces a ridge-like barrier in  $\beta-\sigma$  space. An exploratory run keeps both NIR and X-ray luminosity well below quiescent constraints throughout most of the disc’s evolution, while still producing strong *relative* light curve peaks comparable to the K-model and main  $R(\beta)$  prescriptions considered in this work.

#### 4.4 Effect of magnetisation cut-off

Ressler et al. (2017) elaborates on the need for a  $\sigma$  cut (their Appendix C), which is implemented to prevent numerical errors as the total energy becomes magnetically dominated. However, they state that the maximum allowed value of  $\sigma_{max} = 1$  remains somewhat arbitrarily chosen and is set as a conservative upper limit. As we find the boundary of magnetically dominated regions to be the dominant source of high-frequency emission, the specific value of  $\sigma_{max}$  may have important consequences on the characteristics of the light curve.

Ressler et al. (2017) find only negligible difference between  $\sigma_{max} = 1$  and  $\sigma_{max} = 3$  on their NIR and X-ray emission (see their Fig. C1). Mizuno et al. (2021) also find no significant impact of choosing  $\sigma_{max} = 5$  when modeling 230 GHz images of M87. Chael et al. (2019) analyse a wide range of  $\sigma_{max} = 1, 10, 25, 50$  and no restriction at all (their Fig. 17) for MAD models of M87, which does strongly affect both their turbulent and reconnection heating NIR and X-ray emission profiles.

To assess the effect of this condition on our models, we analyse one time slice during a flux eruption at  $t = 21890 M$  for  $a_* = 0$  in the  $R_{40,1}$  prescription, where normally the SED stays well below quiescent constraints. We then consider both stricter and more lenient  $\sigma_{max}$  restrictions of  $\sigma_{max} = 0.1, 0.5, 1, 3, 5, 10, 20$  and 50. As  $\sigma_{max}$  increases, we include more of the magnetically dominated (and thermally unreliable) eruption zone into the total emission. In Fig. 22 we trace the fluid parameters assuming  $\sigma_{max} = 50$ . The vertical black dashed line in the  $\beta$  versus  $\sigma$  panel shows the typical imposed cutoff of  $\sigma_{max} = 1$ . We also show the SEDs corresponding to each value of  $\sigma_{max}$  in the bottom panel of Fig. 22. Past  $\sigma_{max} \gtrsim 5$ , the model starts to incorporate increasingly unreliable regions of relativistic plasma ( $\Theta_p > 1$ ), linked to the inner magnetised regions of low-density eruption zones. These produce secondary synchrotron and Compton bumps in the SED. For  $\sigma_{max} = 50$ , even inner parts of the jet are included in the emission.

Increasing  $\sigma_{max}$  to  $\sigma_{max} = 3$  seems to significantly increase the NIR and X-ray spectral luminosity, without affecting the sub-mm and radio. In short, including sampling from regions with  $\sigma \lesssim 5$  does significantly increase NIR and X-ray luminosity by approximately an order of magnitude and shifts the synchrotron and Compton peak frequencies. Although regions where  $1 \leq \sigma \leq 5$  may still prove numerically unreliable, this does not yet incorporate emission from highly relativistic parts of the plasma. Future work thus may benefit from a deeper understanding of highly magnetised plasma and potentially from incorporating a range of  $\sigma_{max} \lesssim 5$  values into the analysis.

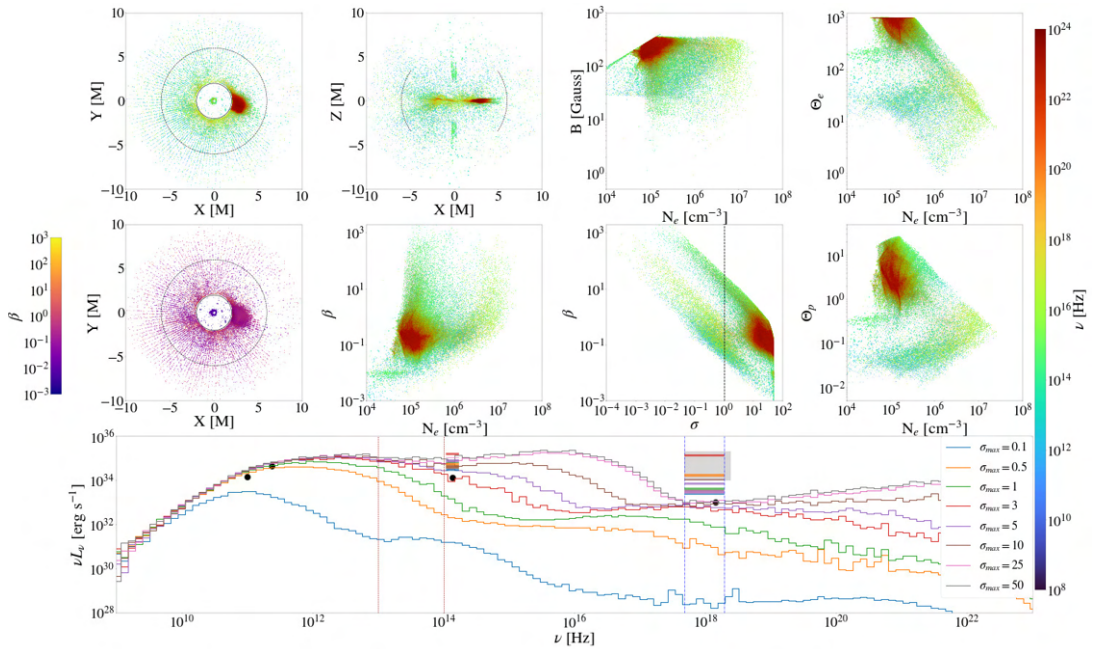


**Figure 22:** Same as in Fig. 12, but only for the  $R_{40,1}$  prescription at  $t = 21890 M$  (corresponding to a strong flux eruption in the disc). Rather than impose the typical  $\sigma < \sigma_{max} = 1$  condition, we set  $\sigma_{max} = 50$  in all panels corresponding to the fluid (top two rows). In the  $\beta$  versus  $\sigma$  panel, we mark  $\sigma_{max} = 1$  with a vertical dashed line. In the bottom row, we show total SEDs, each corresponding to a different value of  $\sigma_{max}$ . The black dots correspond to quiescent constraints, akin to in Fig. 21. The shaded bars centred at  $2.2 \mu\text{m}$  and 4 keV and black dots correspond to simultaneous flaring observations and quiescent constraints, similar to in Fig. 21.

- M. A. Abramowicz, B. Czerny, J. P. Lasota, and E. Szuszkiewicz. Slim Accretion Disks. *ApJ*, 332:646, Sept. 1988. doi: 10.1086/166683.
- D. K. Aitken, J. Greaves, A. Chrysostomou, T. Jenness, W. Holland, J. H. Hough, D. Pierce-Price, and J. Richer. Detection of polarized millimeter and submillimeter emission from sagittarius a\*. *ApJ*, 534(2):L173, may 2000. doi: 10.1086/312685. URL <https://dx.doi.org/10.1086/312685>.
- P. Anninos, P. C. Fragile, and J. D. Salmonson. Cosmos++: Relativistic Magnetohydrodynamics on Unstructured Grids with Local Adaptive Refinement. *ApJ*, 635(1):723–740, Dec. 2005. doi: 10.1086/497294.
- W. Baade and R. Minkowski. On the Identification of Radio Sources. *ApJ*, 119:215, Jan. 1954. doi: 10.1086/145813.
- F. K. Baganoff, M. W. Bautz, W. N. Brandt, G. Chartas, E. D. Feigelson, G. P. Garmire, Y. Maeda, M. Morris, G. R. Ricker, L. K. Townsley, and F. Walter. Rapid X-ray flaring from the direction of the supermassive black hole at the Galactic Centre. *Nature*, 413(6851):45–48, Sept. 2001. doi: 10.1038/35092510.
- F. K. Baganoff, Y. Maeda, M. Morris, M. W. Bautz, W. N. Brandt, W. Cui, J. P. Doty, E. D. Feigelson, G. P. Garmire, S. H. Pravdo, G. R. Ricker, and L. K. Townsley. Chandra X-Ray Spectroscopic Imaging of Sagittarius A\* and the Central Parsec of the Galaxy. *ApJ*, 591(2):891–915, July 2003. doi: 10.1086/375145.
- S. A. Balbus and J. F. Hawley. A Powerful Local Shear Instability in Weakly Magnetized Disks. I. Linear Analysis. *ApJ*, 376:214, July 1991. doi: 10.1086/170270.
- S. A. Balbus and J. F. Hawley. Instability, turbulence, and enhanced transport in accretion disks. *Rev. Mod. Phys.*, 70:1–53, Jan 1998. doi: 10.1103/RevModPhys.70.1. URL <https://link.aps.org/doi/10.1103/RevModPhys.70.1>.
- B. Balick and R. L. Brown. Intense sub-arcsecond structure in the galactic center. *ApJ*, 194:265–270, Dec. 1974. doi: 10.1086/153242.
- J. M. Bardeen, W. H. Press, and S. A. Teukolsky. Rotating Black Holes: Locally Nonrotating Frames, Energy Extraction, and Scalar Synchrotron Radiation. *ApJ*, 178:347–370, Dec. 1972. doi: 10.1086/151796.
- M. C. Begelman. Can a spherically accreting black hole radiate very near the Eddington limit? *MNRAS*, 187:237–251, Apr. 1979. doi: 10.1093/mnras/187.2.237.
- G. S. Bisnovatyi-Kogan and A. A. Ruzmaikin. The Accretion of Matter by a Collapsing Star in the Presence of a Magnetic Field. II: Self-consistent Stationary Picture. *Astrophysics and Space Science*, 42(2):401–424, July 1976. doi: 10.1007/BF01225967.
- R. D. Blandford and D. G. Payne. Hydromagnetic flows from accretion disks and the production of radio jets. *MNRAS*, 199:883–903, June 1982. doi: 10.1093/mnras/199.4.883.
- R. D. Blandford and R. L. Znajek. Electromagnetic extraction of energy from Kerr black holes. *MNRAS*, 179:433–456, May 1977. doi: 10.1093/mnras/179.3.433.

- 
- H. Boyce, D. Haggard, G. Witzel, S. P. Willner, J. Neilsen, J. L. Hora, S. Markoff, G. Ponti, F. Baganoff, E. E. Becklin, G. G. Fazio, P. Lowrance, M. R. Morris, and H. A. Smith. Simultaneous x-ray and infrared observations of sagittarius a\*'s variability. *ApJ*, 871(2):161, jan 2019. doi: 10.3847/1538-4357/aaf71f. URL <https://dx.doi.org/10.3847/1538-4357/aaf71f>.
- A. H. Bridle and R. A. Perley. Extragalactic radio jets. *Annual Review of Astronomy and Astrophysics*, 22(Volume 22, 1984):319–358, 1984. ISSN 1545-4282. doi: <https://doi.org/10.1146/annurev.aa.22.090184.001535>. URL <https://www.annualreviews.org/content/journals/10.1146/annurev.aa.22.090184.001535>.
- S. M. Carroll. *Spacetime and geometry. An introduction to general relativity*. 2004.
- A. Chael. Survey of radiative, two-temperature magnetically arrested simulations of the black hole M87\* I: turbulent electron heating. *MNRAS*, 537(3):2496–2515, Mar. 2025. doi: 10.1093/mnras/staf200.
- A. Chael, M. Rowan, R. Narayan, M. Johnson, and L. Sironi. The role of electron heating physics in images and variability of the galactic centre black hole sagittarius a\*. *MNRAS*, 478(4):5209–5229, 06 2018. ISSN 0035-8711. doi: 10.1093/mnras/sty1261. URL <https://doi.org/10.1093/mnras/sty1261>.
- A. Chael, R. Narayan, and M. D. Johnson. Two-temperature, Magnetically Arrested Disc simulations of the jet from the supermassive black hole in M87. *MNRAS*, 486(2):2873–2895, June 2019. doi: 10.1093/mnras/stz988.
- G. Compère and A. Fiorucci. Advanced Lectures on General Relativity. *arXiv e-prints*, art. arXiv:1801.07064, Jan. 2018. doi: 10.48550/arXiv.1801.07064.
- H. D. Curtis. Descriptions of 762 Nebulae and Clusters Photographed with the Crossley Reflector. *Publications of Lick Observatory*, 13:9–42, Jan. 1918.
- J. Dexter, A. Jiménez-Rosales, S. M. Ressler, A. Tchekhovskoy, M. Bauböck, P. T. de Zeeuw, F. Eisenhauer, S. von Fellenberg, F. Gao, R. Genzel, S. Gillessen, M. Habibi, T. Ott, J. Stadler, O. Straub, and F. Widmann. A parameter survey of Sgr A\* radiative models from GRMHD simulations with self-consistent electron heating. *MNRAS*, 494(3):4168–4186, May 2020a. doi: 10.1093/mnras/staa922.
- J. Dexter, A. Tchekhovskoy, A. Jiménez-Rosales, S. M. Ressler, M. Bauböck, Y. Dallilar, P. T. de Zeeuw, F. Eisenhauer, S. von Fellenberg, F. Gao, R. Genzel, S. Gillessen, M. Habibi, T. Ott, J. Stadler, O. Straub, and F. Widmann. Sgr a\* near-infrared flares from reconnection events in a magnetically arrested disc. *MNRAS*, 497(4):4999–5007, 08 2020b. ISSN 0035-8711. doi: 10.1093/mnras/staa2288. URL <https://doi.org/10.1093/mnras/staa2288>.
- T. Do, A. M. Ghez, M. R. Morris, J. R. Lu, K. Matthews, S. Yelda, and J. Larkin. High Angular Resolution Integral-Field Spectroscopy of the Galaxy's Nuclear Cluster: A Missing Stellar Cusp? *ApJ*, 703(2):1323–1337, Oct. 2009. doi: 10.1088/0004-637X/703/2/1323.
- T. Do, A. M. Ghez, M. R. Morris, S. Yelda, L. Meyer, J. R. Lu, S. D. Hornstein, and K. Matthews. A near-infrared variability study of the galactic black hole: A red noise source with no detected periodicity. *ApJ*, 691(2):1021, jan 2009. doi: 10.1088/0004-637X/691/2/1021. URL <https://dx.doi.org/10.1088/0004-637X/691/2/1021>.
- K. Dodds-Eden, S. Gillessen, T. K. Fritz, F. Eisenhauer, S. Trippe, R. Genzel, T. Ott, H. Bartko, O. Pfuhl, G. Bower, A. Goldwurm, D. Porquet, G. Trap, and F. Yusef-Zadeh. The two states of Sgr A\* in the near-infrared: bright episodic flares on top of low level continuous variability. *ApJ*, 728(1):37, jan 2011. doi: 10.1088/0004-637X/728/1/37. URL <https://dx.doi.org/10.1088/0004-637X/728/1/37>.

- 
- J. C. Dolence, C. F. Gammie, M. Mościbrodzka, and P. K. Leung. grmonty: A Monte Carlo Code for Relativistic Radiative Transport. *ApJ - Supplement Series*, 184(2):387–397, Oct. 2009. doi: 10.1088/0067-0049/184/2/387.
- A. Eckart, F. K. Baganoff, M. Morris, M. W. Bautz, W. N. Brandt, G. P. Garmire, R. Genzel, T. Ott, G. R. Ricker, C. Straubmeier, T. Viehmann, R. Schödel, G. C. Bower, and J. E. Goldston. First simultaneous NIR/X-ray detection of a flare from Sgr A\*. *A&A*, 427:1–11, Nov. 2004. doi: 10.1051/0004-6361:20040495.
- A. Eckart, F. K. Baganoff, R. Schödel, M. Morris, R. Genzel, G. C. Bower, D. Marrone, J. M. Moran, T. Viehmann, M. W. Bautz, W. N. Brandt, G. P. Garmire, T. Ott, S. Trippe, G. R. Ricker, C. Straubmeier, D. A. Roberts, F. Yusef-Zadeh, J. H. Zhao, and R. Rao. The flare activity of Sagittarius A\*. New coordinated mm to X-ray observations. *A&A*, 450(2):535–555, May 2006. doi: 10.1051/0004-6361:20054418.
- A. Eckart, F. K. Baganoff, M. Zamaninasab, M. R. Morris, R. Schödel, L. Meyer, K. Muzic, M. W. Bautz, W. N. Brandt, G. P. Garmire, G. R. Ricker, D. Kunneriath, C. Straubmeier, W. Duschl, M. Dovciak, V. Karas, S. Markoff, F. Najarro, J. Mauerhan, J. Moultaka, and A. Zensus. Polarized NIR and X-ray flares from Sagittarius A\*. *A&A*, 479(3):625–639, Mar. 2008. doi: 10.1051/0004-6361:20078793.
- A. Eckart, M. García-Marín, S. N. Vogel, P. Teuben, M. R. Morris, F. Baganoff, J. Dexter, R. Schödel, G. Witzel, M. Valencia-S., V. Karas, D. Kunneriath, C. Straubmeier, L. Moser, N. Sabha, R. Buchholz, M. Zamaninasab, K. Mužić, J. Moultaka, and J. A. Zensus. Millimeter to X-ray flares from Sagittarius A\*. *A&A*, 537:A52, Jan. 2012. doi: 10.1051/0004-6361/201117779.
- A. S. Eddington. *The mathematical theory of relativity*. 1923.
- EHT Collaboration. First Sagittarius A\* Event Horizon Telescope Results. I. The Shadow of the Supermassive Black Hole in the Center of the Milky Way. *ApJ - Letters*, 930(2):L12, May 2022a. doi: 10.3847/2041-8213/ac6674.
- EHT Collaboration. First Sagittarius A\* Event Horizon Telescope Results. II. EHT and Multiwavelength Observations, Data Processing, and Calibration. *ApJ - Letters*, 930(2):L13, May 2022b. doi: 10.3847/2041-8213/ac6675.
- EHT Collaboration. First Sagittarius A\* Event Horizon Telescope Results. III. Imaging of the Galactic Center Supermassive Black Hole. *ApJ - Letters*, 930(2):L14, May 2022c. doi: 10.3847/2041-8213/ac6429.
- EHT Collaboration. First Sagittarius A\* Event Horizon Telescope Results. V. Testing Astrophysical Models of the Galactic Center Black Hole. *ApJ - Letters*, 930(2):L16, May 2022d. doi: 10.3847/2041-8213/ac6672.
- EHT Collaboration. First Sagittarius A\* Event Horizon Telescope Results. VII. Polarization of the Ring. *ApJ Letters*, 964:L25, mar 2024a. doi: 10.3847/2041-8213/ad2df0. URL <https://dx.doi.org/10.3847/2041-8213/ad2df0>.
- EHT Collaboration. First Sagittarius A\* Event Horizon Telescope Results. VIII. Physical Interpretation of the Polarized Ring. *ApJ Letters*, 964(2):L26, mar 2024b. doi: 10.3847/2041-8213/ad2df1. URL <https://dx.doi.org/10.3847/2041-8213/ad2df1>.
- H. Falcke, F. Melia, and E. Agol. Viewing the Shadow of the Black Hole at the Galactic Center. *ApJ - Letters*, 528(1):L13–L16, Jan. 2000. doi: 10.1086/312423.
- L. G. Fishbone and V. Moncrief. Relativistic fluid disks in orbit around Kerr black holes. *ApJ*, 207:962–976, Aug. 1976. doi: 10.1086/154565.

- 
- C. F. Gammie, J. C. McKinney, and G. Tóth. Harm: A numerical scheme for general relativistic magnetohydrodynamics. *ApJ*, 589(1):444, may 2003. doi: 10.1086/374594. URL <https://dx.doi.org/10.1086/374594>.
- C. F. Gammie, S. L. Shapiro, and J. C. McKinney. Black hole spin evolution. *ApJ*, 602(1):312, feb 2004. doi: 10.1086/380996. URL <https://dx.doi.org/10.1086/380996>.
- R. Genzel, R. Schödel, T. Ott, A. Eckart, T. Alexander, F. Lacombe, D. Rouan, and B. Aschenbach. Near-infrared flares from accreting gas around the supermassive black hole at the Galactic Centre. *Nature*, 425(6961):934–937, Oct. 2003. doi: 10.1038/nature02065.
- R. Genzel, F. Eisenhauer, and S. Gillessen. The Galactic Center massive black hole and nuclear star cluster. *Reviews of Modern Physics*, 82(4):3121–3195, Oct. 2010. doi: 10.1103/RevModPhys.82.3121.
- R. Giacconi, S. Murray, H. Gursky, E. Kellogg, E. Schreier, and H. Tananbaum. The Uhuru catalog of X-ray sources. *ApJ*, 178:281–308, Dec. 1972. doi: 10.1086/151790.
- R. Gold, J. C. McKinney, M. D. Johnson, and S. S. Doeleman. Probing the Magnetic Field Structure in Sgr A\* on Black Hole Horizon Scales with Polarized Radiative Transfer Simulations. *ApJ*, 837(2):180, Mar. 2017. doi: 10.3847/1538-4357/aa6193.
- GRAVITY Collaboration. First light for GRAVITY: Phase referencing optical interferometry for the Very Large Telescope Interferometer. *A&A*, 602:A94, June 2017. doi: 10.1051/0004-6361/201730838.
- GRAVITY Collaboration. A geometric distance measurement to the Galactic center black hole with 0.3% uncertainty. *A&A*, 625:L10, May 2019. doi: 10.1051/0004-6361/201935656.
- GRAVITY Collaboration. The flux distribution of Sgr A\*. *A&A*, 638:A2, June 2020. doi: 10.1051/0004-6361/202037717.
- G. G. Howes. A prescription for the turbulent heating of astrophysical plasmas. *MNRAS*, 409(1):L104–L108, Nov. 2010. doi: 10.1111/j.1745-3933.2010.00958.x.
- G. G. Howes, S. C. Cowley, W. Dorland, G. W. Hammett, E. Quataert, and A. A. Schekochihin. A model of turbulence in magnetized plasmas: Implications for the dissipation range in the solar wind. *Journal of Geophysical Research (Space Physics)*, 113(A5):A05103, May 2008. doi: 10.1029/2007JA012665.
- S. Ichimaru. Bimodal behavior of accretion disks: theory and application to Cygnus X-1 transitions. *ApJ*, 214:840–855, June 1977. doi: 10.1086/155314.
- J. I. Katz. X-rays from spherical accretion onto degenerate dwarfs. *ApJ*, 215:265–275, July 1977. doi: 10.1086/155355.
- Y. Kawazura, M. Barnes, and A. A. Schekochihin. Thermal disequilibration of ions and electrons by collisionless plasma turbulence. *Proceedings of the National Academy of Science*, 116(3):771–776, Jan. 2019. doi: 10.1073/pnas.1812491116.
- R. P. Kerr. Gravitational Field of a Spinning Mass as an Example of Algebraically Special Metrics. *Physical Review Letters*, 11(5):237–238, Sept. 1963. doi: 10.1103/PhysRevLett.11.237.
- P. K. Leung, C. F. Gammie, and S. C. Noble. Numerical Calculation of Magnetobremssstrahlung Emission and Absorption Coefficients. *ApJ*, 737(1):21, Aug. 2011. doi: 10.1088/0004-637X/737/1/21.
- S. Markoff, H. Falcke, F. Yuan, and P. L. Biermann. The Nature of the 10 kilosecond X-ray flare in Sgr A\*. *A&A*, 379:L13–L16, Nov. 2001. doi: 10.1051/0004-6361:20011346.
- D. P. Marrone, J. M. Moran, J.-H. Zhao, and R. Rao. Interferometric measurements of variable 340 ghz linear polarization in sagittarius a\*. *ApJ*, 640(1):308, mar 2006. doi: 10.1086/500106. URL <https://dx.doi.org/10.1086/500106>.

- 
- D. P. Marrone, J. M. Moran, J.-H. Zhao, and R. Rao. An Unambiguous Detection of Faraday Rotation in Sagittarius A\*. *ApJ - Letters*, 654(1):L57–L60, Jan. 2007. doi: 10.1086/510850.
- J. C. McKinney. General relativistic magnetohydrodynamic simulations of the jet formation and large-scale propagation from black hole accretion systems. *MNRAS*, 368(4):1561–1582, 04 2006. ISSN 0035-8711. doi: 10.1111/j.1365-2966.2006.10256.x. URL <https://doi.org/10.1111/j.1365-2966.2006.10256.x>.
- J. C. McKinney and C. F. Gammie. A measurement of the electromagnetic luminosity of a kerr black hole. *ApJ*, 611(2):977, aug 2004. doi: 10.1086/422244. URL <https://dx.doi.org/10.1086/422244>.
- L. Meyer, T. Do, A. Ghez, M. R. Morris, G. Witzel, A. Eckart, G. Bélanger, and R. Schödel. A 600 Minute Near-Infrared Light Curve of Sagittarius A\*. *ApJ*, 688(1):L17, oct 2008. doi: 10.1086/593147. URL <https://dx.doi.org/10.1086/593147>.
- C. W. Misner, K. S. Thorne, and J. A. Wheeler. *Gravitation*. 1973.
- Y. Mizuno, C. M. Fromm, Z. Younsi, O. Porth, H. Olivares, and L. Rezzolla. Comparison of the ion-to-electron temperature ratio prescription: GRMHD simulations with electron thermodynamics. *MNRAS*, 506(1):741–758, Sept. 2021. doi: 10.1093/mnras/stab1753.
- M. Mościbrodzka. Revision of Two-temperature Magnetically Arrested Flows onto a Black Hole. *ApJ*, 981(2):145, Mar. 2025. doi: 10.3847/1538-4357/adb1a7.
- M. Mościbrodzka, H. Falcke, and H. Shiokawa. General relativistic magnetohydrodynamical simulations of the jet in M 87. *A&A*, 586:A38, Feb. 2016. doi: 10.1051/0004-6361/201526630.
- A. Müller. *Black hole astrophysics: magnetohydrodynamics on the Kerr geometry*. PhD thesis, -, Dec. 2004.
- R. Narayan and I. Yi. Advection-dominated Accretion: A Self-similar Solution. *ApJ*, 428:L13, June 1994. doi: 10.1086/187381.
- R. Narayan, I. V. Igumenshchev, and M. A. Abramowicz. Magnetically Arrested Disk: an Energetically Efficient Accretion Flow. *Publications of the Astronomical Society of Japan*, 55(6):L69–L72, 12 2003. ISSN 0004-6264. doi: 10.1093/pasj/55.6.L69. URL <https://doi.org/10.1093/pasj/55.6.L69>.
- R. Narayan, A. Skadowski, R. F. Penna, and A. K. Kulkarni. GRMHD simulations of magnetized advection-dominated accretion on a non-spinning black hole: role of outflows. *MNRAS*, 426(4):3241–3259, Nov. 2012. doi: 10.1111/j.1365-2966.2012.22002.x.
- J. Neilsen, M. A. Nowak, C. Gammie, J. Dexter, S. Markoff, D. Haggard, S. Nayakshin, Q. D. Wang, N. Grosso, D. Porquet, J. A. Tomsick, N. Degenaar, P. C. Fragile, J. C. Houck, R. Wijnands, J. M. Miller, and F. K. Baganoff. A Chandra/HETGS Census of X-Ray Variability from Sgr A\* during 2012. *ApJ*, 774(1):42, Sept. 2013. doi: 10.1088/0004-637X/774/1/42.
- I. D. Novikov and K. S. Thorne. Astrophysics of black holes. In C. Dewitt and B. S. Dewitt, editors, *Black Holes (Les Astres Occlus)*, pages 343–450, Jan. 1973.
- D. N. Page and K. S. Thorne. Disk-Accretion onto a Black Hole. Time-Averaged Structure of Accretion Disk. *ApJ*, 191:499–506, July 1974. doi: 10.1086/152990.
- R. F. Penna, J. C. McKinney, R. Narayan, A. Tchekhovskoy, R. Shafee, and J. E. McClintock. Simulations of magnetized discs around black holes: effects of black hole spin, disc thickness and magnetic field geometry. *MNRAS*, 408(2):752–782, 10 2010. ISSN 0035-8711. doi: 10.1111/j.1365-2966.2010.17170.x. URL <https://doi.org/10.1111/j.1365-2966.2010.17170.x>.

- 
- D. Porquet, P. Predehl, B. Aschenbach, N. Grosso, A. Goldwurm, P. Goldoni, R. S. Warwick, and A. Decourchelle. XMM-Newton observation of the brightest X-ray flare detected so far from Sgr A\*. *A&A*, 407:L17–L20, Aug. 2003. doi: 10.1051/0004-6361:20030983.
- O. Porth, H. Olivares, Y. Mizuno, Z. Younsi, L. Rezzolla, M. Moscibrodzka, H. Falcke, and M. Kramer. The black hole accretion code. *Computational Astrophysics and Cosmology*, 4(1):1, May 2017. doi: 10.1186/s40668-017-0020-2.
- J. E. Pringle. Thermal instabilities in accretion discs. *MNRAS*, 177:65–71, Oct. 1976. doi: 10.1093/mnras/177.1.65.
- S. M. Ressler, A. Tchekhovskoy, E. Quataert, M. Chandra, and C. F. Gammie. Electron thermodynamics in GRMHD simulations of low-luminosity black hole accretion. *MNRAS*, 454(2):1848–1870, Dec. 2015. doi: 10.1093/mnras/stv2084.
- S. M. Ressler, A. Tchekhovskoy, E. Quataert, and C. F. Gammie. The disc-jet symbiosis emerges: modelling the emission of Sagittarius A\* with electron thermodynamics. *MNRAS*, 467(3):3604–3619, May 2017. doi: 10.1093/mnras/stx364.
- B. Ripperda, F. Bacchini, and A. A. Philippov. Magnetic Reconnection and Hot Spot Formation in Black Hole Accretion Disks. *ApJ*, 900(2):100, Sept. 2020. doi: 10.3847/1538-4357/ababab.
- B. Ripperda, M. Liska, K. Chatterjee, G. Musoke, A. A. Philippov, S. B. Markoff, A. Tchekhovskoy, and Z. Younsi. Black Hole Flares: Ejection of Accreted Magnetic Flux through 3D Plasmoid-mediated Reconnection. *ApJ - Letters*, 924(2):L32, Jan. 2022. doi: 10.3847/2041-8213/ac46a1.
- M. E. Rowan, L. Sironi, and R. Narayan. Electron and Proton Heating in Transrelativistic Magnetic Reconnection. *ApJ*, 850(1):29, Nov. 2017. doi: 10.3847/1538-4357/aa9380.
- B. R. Ryan, J. C. Dolence, and C. F. Gammie. bhlight: General Relativistic Radiation Magnetohydrodynamics with Monte Carlo Transport. *ApJ*, 807(1):31, July 2015. doi: 10.1088/0004-637X/807/1/31.
- L. D. S. Salas, M. T. P. Liska, S. B. Markoff, K. Chatterjee, G. Musoke, O. Porth, B. Ripperda, D. Yoon, and W. Mulaudzi. Two-temperature treatments in magnetically arrested disc GRMHD simulations more accurately predict light curves of Sagittarius A\*. *MNRAS*, 538(2):698–710, Apr. 2025. doi: 10.1093/mnras/staf240.
- A. Santangelo and R. Madonia. Fifty years of x-ray astronomy: A look back and into the (near) future. *Astroparticle Physics*, 53:130–151, 2014. ISSN 0927-6505. doi: <https://doi.org/10.1016/j.astropartphys.2013.11.005>. URL <https://www.sciencedirect.com/science/article/pii/S0927650513001631>. Centenary of cosmic ray discovery.
- K. Schwarzschild. Über das Gravitationsfeld eines Massenpunktes nach der Einsteinschen Theorie. *Sitzungsberichte der Königlich Preussischen Akademie der Wissenschaften*, pages 189–196, Jan. 1916.
- N. I. Shakura and R. A. Sunyaev. Black holes in binary systems. Observational appearance. *A&A*, 24: 337–355, Jan. 1973.
- S. L. Shapiro, A. P. Lightman, and D. M. Eardley. A two-temperature accretion disk model for Cygnus X-1: structure and spectrum. *ApJ*, 204:187–199, Feb. 1976. doi: 10.1086/154162.
- A. Tchekhovskoy, R. Narayan, and J. C. McKinney. Efficient generation of jets from magnetically arrested accretion on a rapidly spinning black hole. *MNRAS: Letters*, 418(1):L79–L83, 11 2011. ISSN 1745-3925. doi: 10.1111/j.1745-3933.2011.01147.x. URL <https://doi.org/10.1111/j.1745-3933.2011.01147.x>.

- 
- E. P. Velikhov. Stability of an Ideally Conducting Liquid Flowing between Cylinders Rotating in a Magnetic Field. *Soviet Journal of Experimental and Theoretical Physics*, 9(5):995–998, Nov. 1959.
- P. Virtanen et al. SciPy 1.0: Fundamental Algorithms for Scientific Computing in Python. *Nature Methods*, 17:261–272, 2020. doi: 10.1038/s41592-019-0686-2.
- G. R. Werner, D. A. Uzdensky, B. Cerutti, K. Nalewajko, and M. C. Begelman. The Extent of Power-law Energy Spectra in Collisionless Relativistic Magnetic Reconnection in Pair Plasmas. *ApJ - Letters*, 816(1):L8, Jan. 2016. doi: 10.3847/2041-8205/816/1/L8.
- G. R. Werner, D. A. Uzdensky, M. C. Begelman, B. Cerutti, and K. Nalewajko. Non-thermal particle acceleration in collisionless relativistic electron–proton reconnection. *MNRAS*, 473(4):4840–4861, 09 2018. ISSN 0035-8711. doi: 10.1093/mnras/stx2530. URL <https://doi.org/10.1093/mnras/stx2530>.
- G. R. Werner, A. A. Philippov, and D. A. Uzdensky. Particle acceleration in relativistic magnetic reconnection with strong inverse-compton cooling in pair plasmas. *MNRAS: Letters*, 482(1):L60–L64, 08 2019. ISSN 1745-3925. doi: 10.1093/mnrasl/sly157. URL <https://doi.org/10.1093/mnrasl/sly157>.
- M. Wielgus et al. Millimeter Light Curves of Sagittarius A\* Observed during the 2017 Event Horizon Telescope Campaign. *ApJ - Letters*, 930(2):L19, May 2022. doi: 10.3847/2041-8213/ac6428.
- G. Witzel, G. Martinez, J. Hora, S. P. Willner, M. R. Morris, C. Gammie, E. E. Becklin, M. L. N. Ashby, F. Baganoff, S. Carey, T. Do, G. G. Fazio, A. Ghez, W. J. Glaccum, D. Haggard, R. Herrero-Illana, J. Ingalls, R. Narayan, and H. A. Smith. Variability timescale and spectral index of sgr a\* in the near infrared: Approximate bayesian computation analysis of the variability of the closest supermassive black hole. *ApJ*, 863(1):15, aug 2018. doi: 10.3847/1538-4357/aace62. URL <https://dx.doi.org/10.3847/1538-4357/aace62>.
- G. N. Wong, Y. Du, B. S. Prather, and C. F. Gammie. The jet–disk boundary layer in black hole accretion. *ApJ*, 914(1):55, jun 2021. doi: 10.3847/1538-4357/abf8b8. URL <https://dx.doi.org/10.3847/1538-4357/abf8b8>.
- A. I. Yfantis, M. A. Mościbrodzka, M. Wielgus, J. T. Vos, and A. Jimenez-Rosales. Fitting the light curves of Sagittarius A\* with a hot-spot model. Bayesian modeling of QU loops in the millimeter band. *A&A*, 685:A142, May 2024. doi: 10.1051/0004-6361/202348230.
- F. Yuan and R. Narayan. Hot accretion flows around black holes. *Annual Review of Astronomy and Astrophysics*, 52(1):529–588, Aug. 2014. ISSN 1545-4282. doi: 10.1146/annurev-astro-082812-141003. URL <http://dx.doi.org/10.1146/annurev-astro-082812-141003>.
- F. Yuan, E. Quataert, and R. Narayan. Nonthermal electrons in radiatively inefficient accretion flow models of sagittarius a\*. *ApJ*, 598(1):301–312, Nov. 2003. ISSN 1538-4357. doi: 10.1086/378716. URL <http://dx.doi.org/10.1086/378716>.
- F. Yusef-Zadeh, H. Bushouse, R. G. Arendt, M. Wardle, J. M. Michail, and C. J. Chandler. Nonstop Variability of Sgr A\* Using JWST at 2.1 and 4.8  $\mu\text{m}$  Wavelengths: Evidence for Distinct Populations of Faint and Bright Variable Emission. *ApJ - Letters*, 980(2):L35, Feb. 2025. doi: 10.3847/2041-8213/ada88b.

## A

## Appendix - Bias modification

To efficiently sample the upscattered part of the spectrum in an optically thin source, `grmonty` uses a biased scattering probability distribution (Eq. 29, see also §5.1 [Dolence et al. \(2009\)](#)). The larger the bias, the larger the likelihood of scattering. To avoid undersampling parts of the spectrum associated with synchrotron source photons, the incident photon is not terminated upon scattering but continues. The code then launches a new upscattered photon, which is identically evolved throughout the system. To conserve the total photon number, the code adjusts the weights appropriately, scaled by the additional biased likelihood of scattering. For the incident photon  $w_i \rightarrow w(1 - 1/b)$  (with subscript  $i$  labelling the initial value). The upscattered photon then gets a weight  $w/b$ . The code contains a tuning routine to avoid ‘overbiasing’, where scattering becomes too probable, possibly resulting in a chain reaction. This would significantly increase computational cost (as more upscattered photons need to be tracked) and possibly even terminate the simulation if the ratio of scattered to sourced superphotons  $N_{scatt}/N_{made}$  becomes too large.

A problem encountered in our runs was the inability of this bias tuning routine to consistently keep this ratio between a reasonable  $0.5 \leq N_{scatt}/N_{made} \leq 3$ . Rather than manually adjusting the bias per run, we incorporate an additional routine that decreases the bias if  $N_{scatt}/N_{made}$  exceeds a chosen ratio. We arbitrarily choose a function to decrease the bias activated by the following condition

$$\text{if } \frac{N_{scatt}}{N_{made}} > \lambda \Rightarrow b = \frac{b_i}{c^{\frac{1}{\lambda} \frac{N_{scatt}}{N_{made}}}},$$

where  $\lambda$  is the desired scattering ratio and  $c$  is an arbitrarily chosen constant dictating the intrusive strength of the routine on the bias ( $c > 1$ ), which we set to  $c = 3$ . As `grmonty` does not permit scattering ratios of  $N_{scatt}/N_{made} > 10$ , we set  $\lambda = 3$  in our main runs. This will first attempt to linearly correct the bias if  $N_{scatt}/N_{made} > 3$  while transitioning to an inverse cubic decrease if  $N_{scatt}/N_{made} > 9$ . The base of the exponential can be arbitrarily altered to any number as long as  $c > 1$ . Although other functions are certainly equally capable of keeping the bias in check, we find this method adequately redirects the bias without being overtly intrusive on the simulation. When tested during strong peaks in the NIR and X-ray light curves, this method shows no noticeable deviation from the code’s inherent biasing strategy.

## B Appendix - Emission maps and plasma parameters

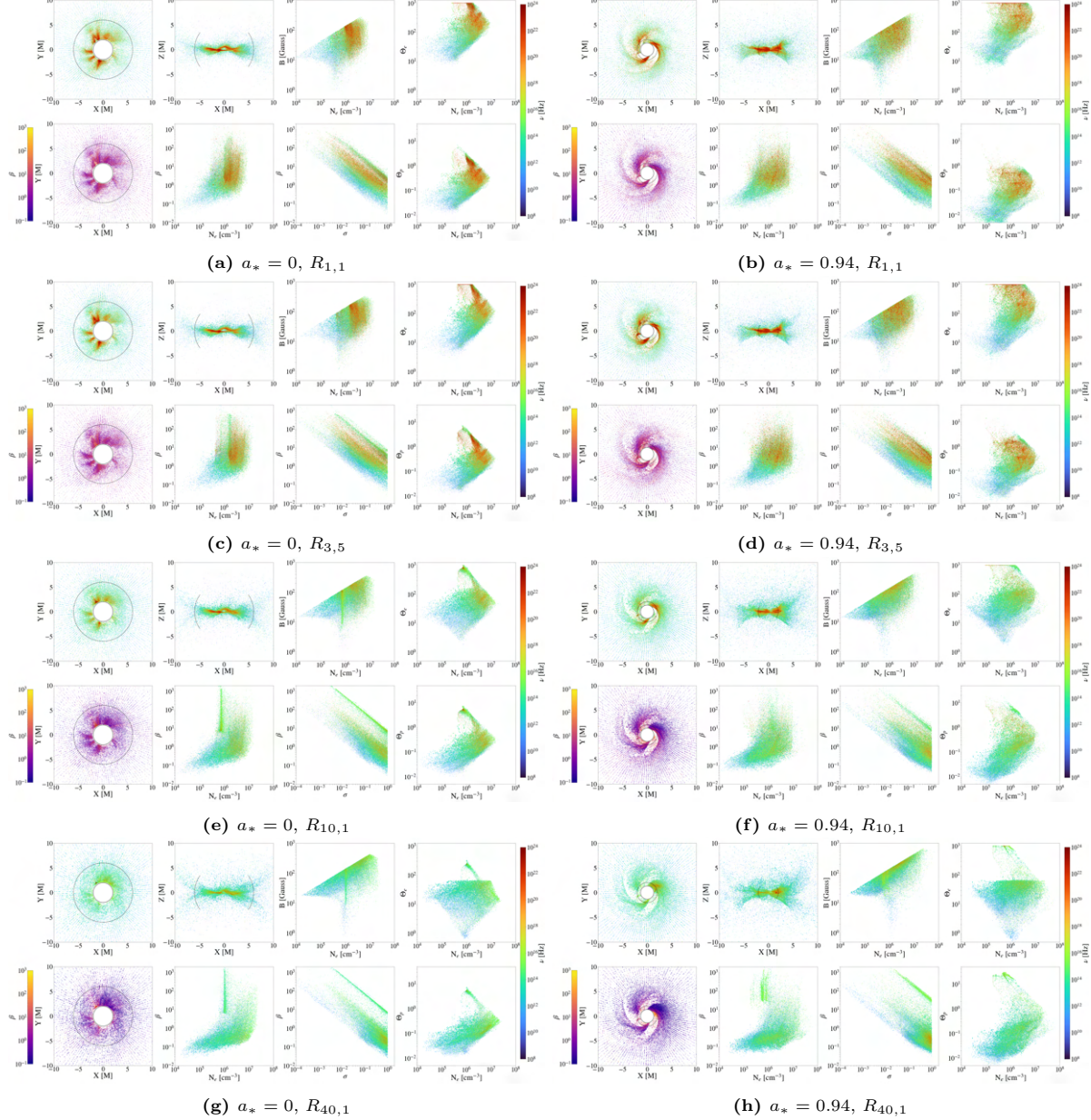


**Figure B1:** Same as in Fig. 12 and 13, but for all additional temperature models at  $t = 23630 M$  for  $a_* = 0$  (left column) and  $t = 20000 M$  for  $a_* = 0.94$  (right column). Each row shows a different  $R(\beta)$  prescription. Full evolution movies for a variety of  $R(\beta)$  models are available [here](#).

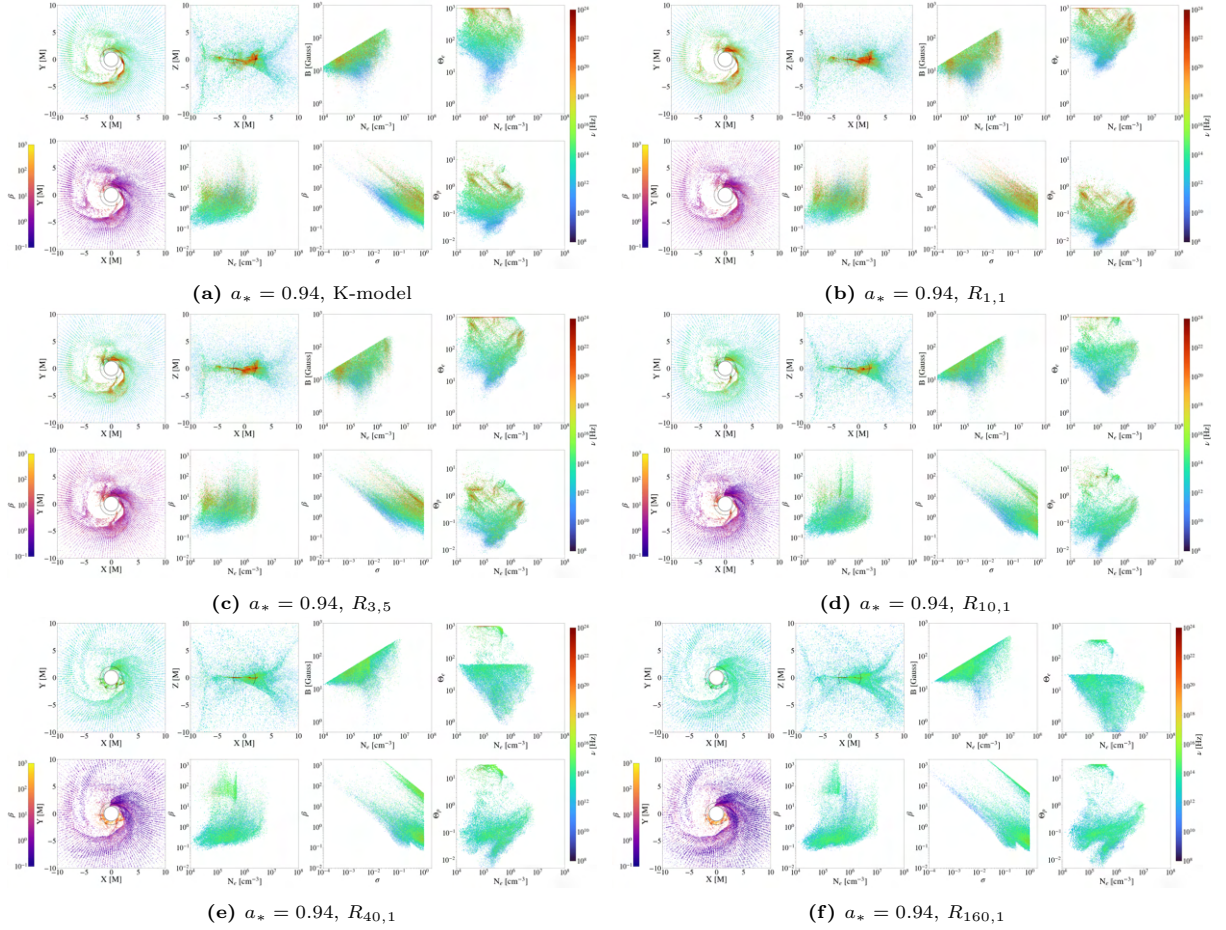


**Figure B2:** Same as in Fig. 13, but for a different time snapshot at  $t = 23010 M$ , where a strong flux eruption expels large portions of the disk.

## C Appendix - Prospects for a $R(\beta, \sigma)$ prescription

The evolution of Figs. 12 and 13 (and by extension Figs. B1) highlights how the hot eruption layers occupy large portions of the  $\beta$ - $N_e$  diagrams where  $\beta \gtrsim 1$ . However, both the K-model and hottest  $R_{\leq 3, \leq 5}$  prescriptions couple strongly to the most energetic and dense part of the plasma at similar  $\beta$  closest to the event horizon, resulting in persistently high luminosities even during ‘quiescent’ states of the disk where flux eruptions are either non-occurring or remain minor.

Ideally, we would like a temperature model that behaves like the  $R_{40,1}$  prescription in quiescence, but can still tap into the eruption layers to produce bright NIR and X-ray flares. While the standard  $R(\beta)$  model effectively reduces the coupling close to the horizon, it cannot simultaneously couple to the low-density eruption layers needed for flare-like luminosity spikes. Because these eruption layers exist at similar beta ( $\beta \gtrsim 1$ ), but lower densities compared to the hot quiescent gas near the horizon, adding an explicit density-dependent temperature increase to the  $R(\beta)$  prescription could, in principle, distinguish the two populations.

Alternatively, the  $\beta$ - $\sigma$  diagrams reveal a clear separation between the quiescent parts of the plasma and the eruption layers. These eruption layers occupy a distinct region above a main quiescent population, most apparent for the somewhat cooler prescriptions such as  $R_{10,1}$  in Fig. B1(e). This suggests that a prescription that smoothly transitions in  $\sigma$ - $\beta$  space can decouple the hot quiescent component from the flare-generating eruption layers without relying on coordinate or density-imposed criteria.

To achieve this, we define rotated coordinates in  $\log_{10} \beta$ - $\log_{10} \sigma$  space and impose a temperature ‘ridge-like’ barrier centred on the hottest parts of the quiescent electron population. We model the barrier as a stretched out Gaussian bump centred around coordinates  $(\sigma_0, \beta_0)$  and tilted in  $\log_{10} \sigma$ - $\log_{10} \beta$  space by a slope parameter

$$s = \frac{\Delta(\log_{10} \beta)}{\Delta(\log_{10} \sigma)}. \quad (36)$$

The corresponding rotation angle is then  $\theta = \tan^{-1}(s)$ . To ensure that the baseline regions  $R_{below}$  and  $R_{above}$  (defined below) correspond intuitively to the ‘below’ and ‘above’ sides of the barrier, we add a factor of  $\pi$  to the rotation angle. The rotated coordinates then become

$$\sigma_0 = \log_{10} \sigma_{center}, \quad (37)$$

$$\beta_0 = \log_{10} \beta_{center}, \quad (38)$$

$$X_{rot} = \cos(\theta + \pi) (\log_{10} \sigma - \sigma_0) + \sin(\theta + \pi) (-[\log_{10} \beta - \beta_0]), \quad (39)$$

$$Y_{rot} = -\sin(\theta + \pi) (\log_{10} \sigma - \sigma_0) + \cos(\theta + \pi) (-[\log_{10} \beta - \beta_0]), \quad (40)$$

where  $\sigma_{center}$  and  $\beta_{center}$  determine the center of a imposed Gaussian barrier, which determines the local transition strength according to

$$B = \exp\left(-\frac{X_{rot}^2}{L^2} - \frac{Y_{rot}^2}{W^2}\right). \quad (41)$$

$L$  and  $W$  are arbitrary constants that allow one to modify the shape of the Gaussian. We set  $\log_{10} L = 8$  to stretch the Gaussian bump into a ridge-like barrier and  $\log_{10} W = 1/5$ , which sets the effective width of the barrier reasonably small. We artificially alter the baseline ion-to-electron ratio above and below the barrier according to

$$R_{eff} = \begin{cases} R_{below} & Y_{rot} < 0, \\ R_{above} & Y_{rot} > 0. \end{cases}$$

In our exploratory model, we cool the plasma below the barrier by setting  $R_{below} = 15$  and  $R_{above} = 1$ .

Finally, the local ion-to-electron temperature ratio is determined by

$$\frac{T_i}{T_e} = R_{eff} + (R_{barrier} - R_{eff})B, \quad (42)$$

where  $R_{barrier}$  determines the barrier height along the centre of the ridge. We here set  $R_{barrier} = 300$ , which enforces strong cooling. In Fig. C1, we show the resulting parameterisation prescription. Regions below the barrier in  $\beta$ - $\sigma$  space are predominantly populated by the quiescent parts of the plasma, whereas only the eruption layers attain the high  $\beta$  and  $\sigma$  necessary to couple to the strongly heated region above the barrier. The barrier itself then acts to suppress a substantial portion of the most luminous quiescent emission near the horizon.

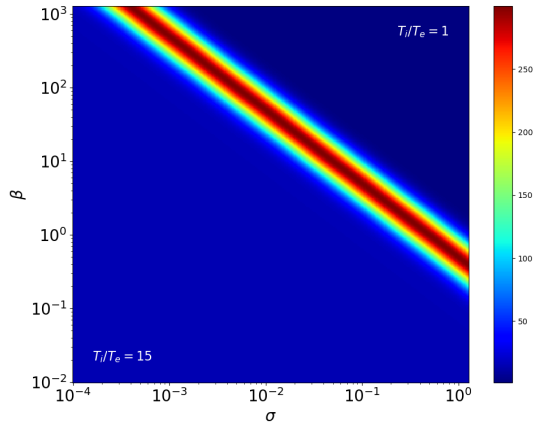


**Figure C1:** Temperature ratio ( $T_i/T_e$ ) diagram as a function of  $\beta$  and  $\sigma$  according to the alternative  $R(\beta, \sigma)$  prescription with parameters as described in the text. This artificially imposes a ridge-like barrier to better separate the quiescent parts of the disc from the eruption layers.

Like in our main  $R(\beta)$  models, we increase  $\mathcal{M}$  accordingly to fit the observed 230 GHz flux. We run an exploratory model for  $a_* = 0$  to demonstrate the behaviour of this alternative temperature prescription, albeit only for the one set of parameters described above. We sample  $\sim 6 \times 10^6$  synchrotron superphotons, which upscatter to at most  $\sim 1 \times 10^6$  superphotons during strong peaks in the light curve. Although the NIR parts of the spectrum remain reasonably smooth, the X-ray light curves are less reliable, but remain sufficient to probe general trends, especially during peaks in the light curve. In Fig. C2, we compare the resulting light curves with those of the K-model,  $R_{1,1}$  and  $R_{160,1}$  prescriptions.

As intended, the alternative  $R(\beta, \sigma)$  prescription remains significantly cooler compared to the K-model and  $R_{1,1}$  prescription throughout most of its evolution. This lowers the average luminosity by just under a decade compared to the K-model. Moreover, the  $R(\beta, \sigma)$  prescription is still capable of strong coupling to the eruption layers, as demonstrated by the spike at  $t = 23630 M$ . Between  $23200 \leq t \leq 23700 M$ , its luminosity varies by approximately a factor of  $\sim 30$ , both in NIR and X-rays. The light curve becomes more variable on short timescales, such that its total RMS fractional variability is 0.74 in NIR and 0.68 in X-rays. However, this may in part be the effect of the lower spectral resolution in our exploratory model. For reference, the highest RMS variability for the remaining temperature models plotted in Fig. C2 is 0.48 in NIR and 0.41 in X-rays (both K-model). Measured against its own averaged luminosity, the alternative  $R(\beta, \sigma)$  prescription does not reach notably higher maximum-to-averaged luminosity ratios.

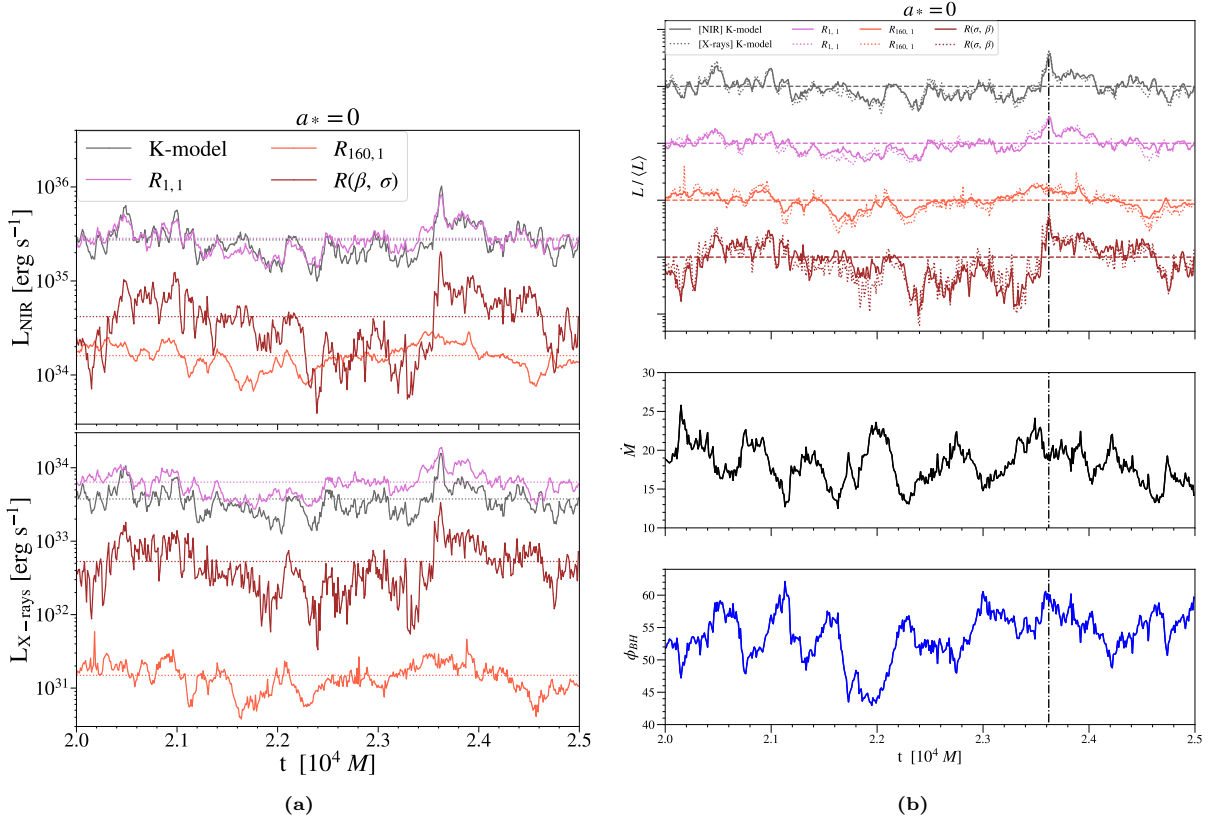


**Figure C2:** A comparison of the ‘ridge-like barrier’  $R(\beta, \sigma)$  prescription (with parameters described in the text) with the K-model,  $R_{1,1}$  and  $R_{160,1}$  prescription, only for  $a_* = 0$ . The grey, red, purple and brown lines respectively correspond to the K-model,  $R_{160,1}$ ,  $R_{1,1}$  and  $R(\beta, \sigma)$  prescriptions. **(a):** NIR and X-ray light curves, same as in Fig. 15. **(b):** NIR and X-ray light curves normalised by their average and the mass accretion rate and magnetic flux on the horizon, same as in Fig. 20.

In Fig. C3, we provide an overview of the plasma parameters for the  $R(\beta, \sigma)$  prescriptions, associated with the peak in the light curve at  $t = 23630 M$ . In Fig. C4 we do the same, but during a supposed ‘quiescent’ moment in the disc’s evolution at  $t = 22690 M$ . The figures highlight how the prescription is capable of decoupling from the plasma on the horizon, while still coupling to the highly energetic flux eruption layers. Such an alternative temperature prescription may allow our radiative models to behave more like observed flare-like emission. However, a more qualitative assessment would require an extensive investigation of the (rather large) parameter space, which we leave to future work.

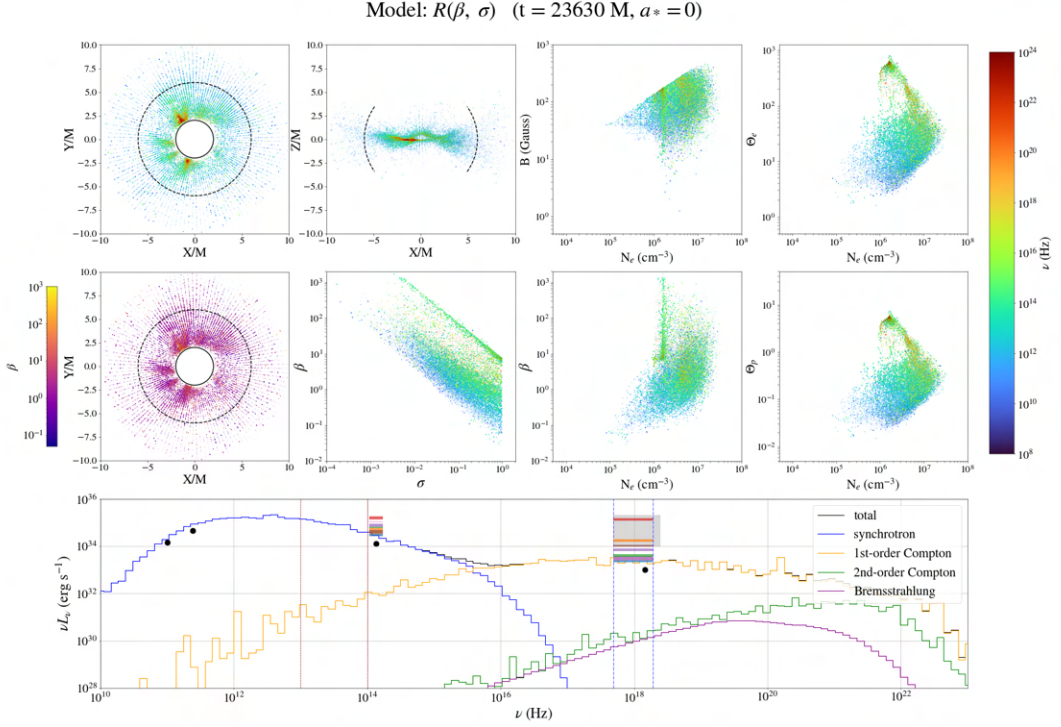


**Figure C3:** Same as in Fig. 12, but for the  $R(\beta, \sigma)$  prescription described in the text. The bottom panel with the SED contains the same observational comparison as in Fig. 21. All panels correspond to the peak in the light curve at  $t = 23630 M$ . The model does a reasonable job of reducing high-frequency emissions from near the horizon, while still coupling well to flux eruptions. However, its luminosity during the light curve peak still sits below observed flare-like observations.

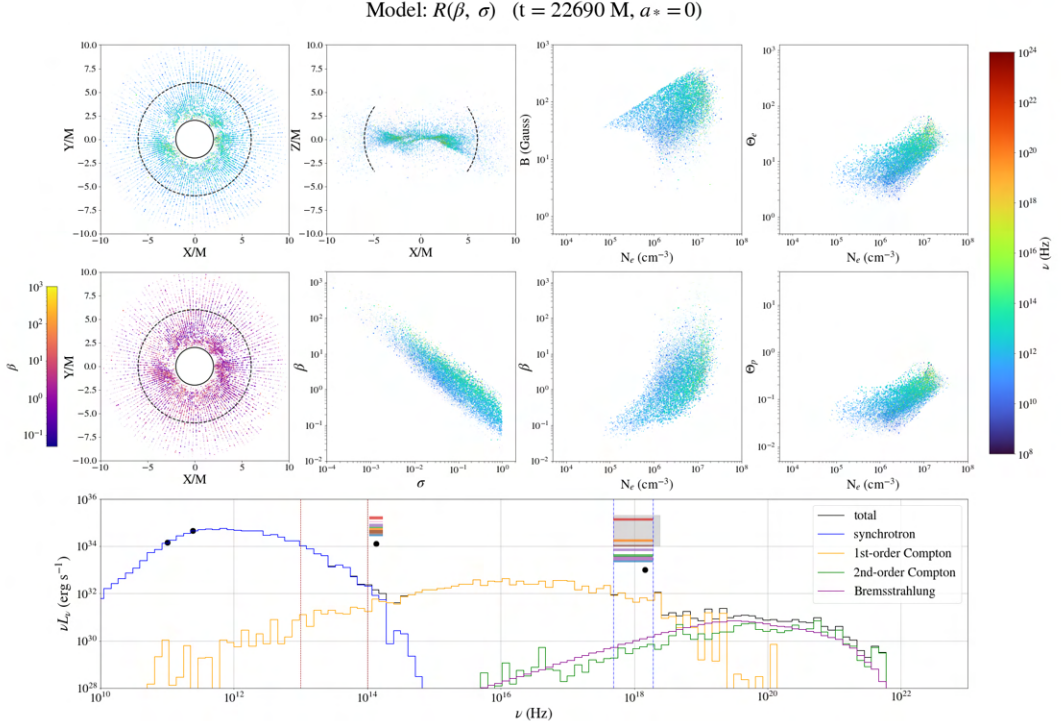


**Figure C4:** Same as in Fig. C3, but for  $t = 22690 M$ , during a ‘quiescent’ moment in the disc’s evolution. A movie depicting the full evolution of these panels can be found [here](#).